



HAL
open science

From cells to tissues: physical modelling of the collective behaviour of embryonic cells

Jos Käfer

► **To cite this version:**

Jos Käfer. From cells to tissues: physical modelling of the collective behaviour of embryonic cells. Biological Physics [physics.bio-ph]. Université Joseph-Fourier - Grenoble I, 2008. English. NNT : . tel-00346418

HAL Id: tel-00346418

<https://theses.hal.science/tel-00346418>

Submitted on 11 Dec 2008

HAL is a multi-disciplinary open access archive for the deposit and dissemination of scientific research documents, whether they are published or not. The documents may come from teaching and research institutions in France or abroad, or from public or private research centers.

L'archive ouverte pluridisciplinaire **HAL**, est destinée au dépôt et à la diffusion de documents scientifiques de niveau recherche, publiés ou non, émanant des établissements d'enseignement et de recherche français ou étrangers, des laboratoires publics ou privés.



Université Grenoble I - Joseph Fourier
Ecole Doctorale de Physique
Spécialité : Physique pour les sciences du vivant

**Des cellules aux tissus :
modélisation physique
du comportement collectif
des cellules embryonnaires**

Jos Käfer



Directeur de thèse : François Graner
Laboratoire de Spectrométrie Physique (UMR 5588)
Soutenance de thèse : 5 décembre 2008

JURY:

Yohanns Bellaïche	Rapporteur
Pierre-François Lenne	Rapporteur
Andreas Deutsch	Président
Hervé Guillou	Examineur
François Graner	Directeur de thèse

**From cells to tissues:
physical modelling
of the collective behaviour
of embryonic cells**

Jos Käfer

Thesis supervisor : François Graner
Laboratoire de Spectrométrie Physique (UMR 5588)
PhD-defense : 5 December 2008

Keywords: Morphogenesis, Biological development, Cell adhesion, Cellular patterns, Cell aggregates, Monte-Carlo simulations

Mots clés : Morphogenèse, Développement biologique, Adhésion cellulaire, Motifs cellulaires, Agrégats cellulaires, Simulations Monte-Carlo

- Écoute-moi bien, Onésiphore, j'ai moult soucis que je vais te déverser dans les oreilles.

- Vous eûtes des ennuis dans la ville capitale ?

- Il ne s'agit pas de cela, dit le duc agacé. Au fait, tu le sais ou tu le supposes ?

- Hm, hm, fit Onésiphore. Durant votre absence, vos filles furent sages comme des images collées à la porte d'un savetier.

- Ouais. Nous verrons ça plus tard. Pour le moment, j'ai trois questions à te poser, qui sont : primo ce que tu penses des rêves, secundo ce que tu penses du langage des animaux, tertio ce que tu penses de l'histoire universelle en général, et de l'histoire générale en particulier. J'écoute.

- Hm, hm, fit Onésiphore. Distinguo...

- Pas de distinguo ! hurla le duc en tapant du pied. Tu entends ? Pas de distinguos, pas de dialectique, rien de tout cela. Je veux du solide. J'écoute.

- Hm, hm, fit Onésiphore. Je ne puis répondre aux trois questions simultanément : mon discours est linéaire, comme tout discours humain.

(Raymond Queneau - Les fleurs bleues, 1965)

Acknowledgements en remerciements

Etant un biologiste des Pays-Bas, je suis venu, naïvement, faire une thèse dans un labo de physique en France. J'ai appris des tas de choses, tout en m'amusant bien : merci à tous et à toutes qui m'ont aidé dans cette aventure. Impossible de remercier tout le monde ; cette page de ma thèse n'est pas le seul moyen de remercier, j'espère l'avoir fait ou pouvoir le faire autrement.

Premièrement, merci à François, mon directeur de thèse. Tu m'as proposé de venir faire une thèse entouré par les montagnes et les physiciens, et ça ne m'a pas déplu ! Merci de m'avoir 'obligé' de discuter en français dès le deuxième mois de ma thèse, et merci pour ta patience avec un biologiste. Ta manière de voir la science et faire de la recherche est, comment dirais-je, assez particulière, et j'ai eu l'occasion d'apprendre bien des choses par rapport à la physique, la pédagogie, les collaborations, rédiger, tout en ayant la possibilité de ne pas être d'accord avec toi ... Merci aussi pour tout qui n'était pas science : ballades fatigantes, discussions politiques, partage d'un panier de légumes ...

Merci aux rapporteurs, Yohanns Bellaïche et Pierre-François Lenne, qui ont accepté de lire en détail ce manuscrit aux interfaces de deux domaines de la science, and thanks to the jury members Hervé Guillou and Andreas Deutsch for their commitment to this last part of a PhD-thesis.

This thesis would not have been possible without the investment of all collaborators. Richard Carthew and Takashi Hayashi did an excellent job in understanding and discussing biology and simulations with a 'theoretical biologist'; their help was essential to make the first year of my thesis to a success. Carl-Phillip Heisenberg and Michael Krieg had the insight to combine experiments and modelling to explain physical phenomena in cell sorting; on top of that, thanks to Michael for the good reception in Dresden. Abbas Mgharbel, Hélène Delanoë et Jean-Paul Rieu ont entrepris l'aventure de comparer quantitativement leurs expériences et nos simulés : le futur dira

ce que ça devient. Thanks to Rita de Almeida, Gilberto Thomas and Marco Idiart for the good reception in Brazil.

Een speciale plaats hebben Stan Marée, Verônica Grieneisen, en Paulien Hogeweg. Stan en Paulien, door jullie bevlogen begeleiding tijdens mijn afstudeervak heb ik de smaak van theoretische biologie te pakken gekregen, en kon ik mijn werk in Grenoble goed beginnen. Stan en Verônica, bedankt voor jullie niet aflatende enthousiasme voor alles wat met ontwikkelingsbiologie, simulaties, Brazilië en nog veel meer te maken heeft, en *last but not least*: zonder jullie zou ik nooit in Grenoble terecht gekomen zijn!

L'accueil au labo pour ce qui n'était pas science était chaleureusement fait par Christophe : j'ai pu découvrir les montagnes, Grenoble et ses marchés, la cuisine française, le vin des côtes du Rhône, Georges Brassens, la pétanque, les contrepèteries, les champignons. Ta voiture qui nous a souvent accompagné en montagne roule toujours sous le derrière d'un conducteur inexpérimenté. Et figure-toi que je me suis finalement même bien servi du contenu scientifique de ta thèse !

Merci aux autres membres du labo : Patrice (pour l'aide informatique et linguistique), Catherine (pour Sinterklaas et l'ambiance au labo), Philippe (qui m'a même appris à quoi sert un modèle mathématique), Jan-Paul (voor de lessen integratie voor een Nederlander in Frankrijk, en de geheimtaal 'nederlands'), mon co-bureau Clément (pour le soutien biophysique), Giovanni (entre autres pour les sorties, parfois bourrines, en montagne), les autres doctorants Julien, Pascale, Malika, Maud, Cécile, Andreea, Shirin, Christoph, David, Edith et Valentina (sans vous il n'y aurait pas autant de vie au labo), Jessie, et bien d'autres encore.

A la colocation à l'Île d'Amour, j'ai apprécié, et j'apprécie encore, la bonne atmosphère, la bonne cuisine, le potager, la musique, les sorties dans les montagnes, les soirées sympas, le soutien des thésards Caro et Sam, et les accents du sud qu'apporte Estelle ; tout cela constitue un véritable chez moi, un point de repos après les journées et semaines de simulations ou rédaction (ou après les randos en montagne).

En dan nog een dankwoord aan mijn ouders : bedankt voor alle hulp, en met name bedankt voor alle vragen over mijn onderzoek, die me zeker geholpen hebben bij het begrijpelijk maken van mijn werk voor anderen.

Contents

Acknowledgements en remerciements	vii
Preface	xiii
Context of this thesis	xv
1 Introduction	17
1.1 Developmental biology	17
1.1.1 Morphogenesis	17
1.1.2 The cell	19
1.1.2.1 Overview	19
1.1.2.2 Cytoskeleton	20
1.1.2.3 Cytoskeleton and the membrane	22
1.1.2.4 Cell adhesion	23
1.1.3 Tissues	24
1.2 The physics for this thesis in a nutshell	28
1.2.1 Forces, energy	28
1.2.2 Liquids	30
1.2.3 Foams	32
1.2.3.1 Structure at equilibrium	32
1.2.3.2 Foam dynamics	35
1.3 Analogies between biological and physical systems	37
1.3.1 Liquids and cellular aggregates	37
1.3.2 Bubbles and tissues	39
1.4 This thesis	40
1.5 Résumé français	41
2 The Cellular Potts Model (CPM)	43
2.1 Context	43
2.2 Algorithm	44
2.2.1 Energy	44

CONTENTS

2.2.2	Lattice	45
2.2.3	Energy minimisation	47
2.3	Quantitative use	49
2.3.1	Measurements	49
2.3.2	Length and time scales	50
2.4	Implementation, use and resources	51
2.5	Résumé français	52
3	Cell topology and geometry in <i>Drosophila</i> eye facets	53
3.1	Introduction	53
3.2	Methods	56
3.2.1	Experiments	56
3.2.2	Simulations	57
3.2.3	Image analysis	58
3.3	Modelling cells as soap bubbles	59
3.4	Adhesion and the contractile cytoskeleton	61
3.4.1	Variable tension model	61
3.4.2	Wildtype	62
3.4.3	<i>Roi</i> mutants	65
3.4.4	N-cadherin mutants	66
3.4.5	E-cadherin mutants	68
3.4.6	E- and N-cadherin mutants	70
3.5	Discussion	70
3.5.1	Constant and variable tension models	70
3.5.2	Adhesion	71
3.5.3	Cortical tension	72
3.6	Conclusions	73
3.7	Résumé français	73
4	Adhesion and contraction in cell sorting of zebrafish germ layers	75
4.1	Introduction: the zebrafish and gastrulation	75
4.2	Overview of experiments	76
4.2.1	General	76
4.2.2	Cell sorting	77
4.2.3	Adhesion strength	77
4.2.4	Cortical tension	81
4.3	Role of contraction in tissue surface tension	81
4.3.1	Cortical tension as a cell property	81
4.3.2	Interface-specific cortical tension	85
4.3.3	Gastrulation	88

4.4	Discussion	89
4.4.1	Cortical tension and the DAH	89
4.4.2	Towards a quantitative description	91
4.4.3	Gastrulation	93
4.5	Conclusion	93
4.6	Résumé français	94
5	Aggregate compression	97
5.1	Introduction	97
5.1.1	Cell aggregates	97
5.1.2	Liquid and solid behaviour	100
5.1.3	Time scales	101
5.1.4	This chapter	103
5.2	Methods	104
5.2.1	Compression and forces	104
5.2.2	Aggregate shape	105
5.2.3	Surface tension	106
5.2.4	Estimations	107
5.2.5	Cell shape and spatial behaviour	108
5.2.6	Validations and optimisation	108
5.3	Aggregate compression	114
5.3.1	Liquid behaviour	114
5.3.2	Cell-cell interfacial tension and fluctuations	114
5.3.3	Cell-medium interfacial tension	117
5.3.4	Variable tension model	118
5.3.5	Relaxation towards equilibrium	122
5.4	Discussion	128
5.4.1	Liquid and non-liquid behaviour	128
5.4.2	Biological origin of the parameters	129
5.4.3	Simulations	130
5.4.4	Perspectives	131
5.5	Résumé français	132
6	Concluding discussion	135
6.1	Synthesis	135
6.1.1	Summary of the results	135
6.1.2	Merits and limits of physical analogies	137
6.2	Modelling approach	137
6.3	Contemporary literature	139
6.4	Outlook	141
6.5	Résumé français	143

CONTENTS

Bibliography

145

Preface

How does a fertilised egg cell give rise to an organism with legs, hairs, eyes (or feathers, Figure 1)? Of course, by having lots of cell divisions. But that only accounts for the creation of more cells, not for the establishment of shapes. Multicellular organisms are a coherent cell mass, not a collection of scattered cells. Cells adhere; but when mutually adhering objects are mixed together, they form a mass with the shape of a sphere, or something not too different from a sphere (Steinberg, 1963). To form an organism, one thus needs more than adhesion alone.



Figure 1: René Magritte, Clairvoyance, 1936

Thanks to N. Desprat for bringing this work to my attention.

We here try to understand how an organism acquires its shape. Most multi-cellular organisms change their shape during development. When we try to change the shape of an object, we have to apply force. An organism provides itself the forces to shape itself (cf Figure 2), of course also influenced by external forces (e.g. gravity). The study of biological morphogenesis thus requires to understand how an organism can exert forces, and how it reacts to them.

Physics is the science of matter and its motion, in space and time *. Organisms, tissues and cells are ‘matter’ as well, so they can be studied physically. The science related to physics that deals with forces and how matter responds to them is mechanics.

Biology is an experimental science. Several experimental approaches to find out how a biological system (e.g. cell, organism, ecosystem) functions

*<http://en.wikipedia.org/wiki/Physics>, Aug. 28, 2008

exists. The first approach is to identify the components that interact; in an organism this typically involves dissection, in a cell microscopy. Then one tries to find out how these components interact, and what the effect of one component on the system is. A widely used technique is to destroy a component in a system, and to compare the behaviour of this mutant (in the widest sense of the word) with the normal system. But one component often has multiple interactions, making it difficult to infer the role of one component from such experiments.

Theoretical “toy” models can be useful tools in such complex systems. The goal is to make a model as simple as possible, describing the interactions between the components in equations, and trying to find out how the model behaves. Because of the complexity of many biological systems (many different interacting components; or the components themselves are complex), it is often impossible to solve the equations describing the system analytically. One can then still study a model theoretically, by running computer simulations (‘numerical simulations’), and trying to interpret the outcome. To quote A. Einstein, a model “should make things as simple as possible, but not simpler”, in order to link the role of the constituents to the observed behaviour.

When building such a model, one typically has to make some assumptions: what details should be included and what not; some relations are not known, but we still have to assume something to get the model to work. One thus tries to limit the number of assumptions (minimal model), or tries to test them. This necessity to make assumptions has an advantage: it points out which elements of the system are ill-understood.

Theoretical models allow to test hypotheses that are not directly testable in experiments. Since it is easier to change a model variable than to create a mutant organism, models are useful to predict; since it is easier to know the value of a model variable than to measure experimentally, models are useful in the quantification of effects and relations. And one knows exactly what one has put in the model: complex behaviour can sometimes be explained by surprisingly simple interactions.

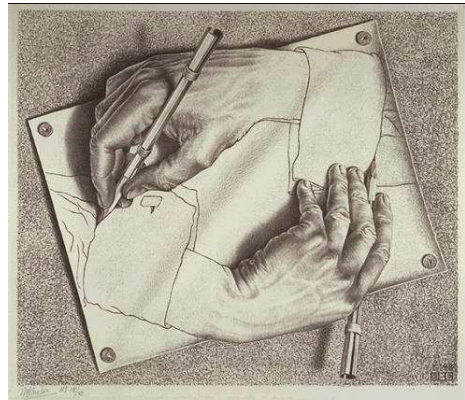


Figure 2: Drawing Hands, M.C. Escher, 1948.

All M.C. Escher works (c) 2008 The M.C. Escher Company - the Netherlands. All rights reserved. Used by permission. www.mcescher.com

Context of this thesis

In this thesis, I try to model some mechanical aspects of biological morphogenesis. The research was conducted in a physical lab, in the group DyFCoM (*Dynamique des Fluides Complexes et Morphogenèse*, dynamics of complex fluids and morphogenesis). Research in this group includes the study of deformable objects, individually or collectively. These objects range from vesicles and bubbles to cells, and in their study, experiments, simulations and theory are combined.

One of the subjects are foams, which are collections of bubbles. As I will lay out in the introduction, the mechanical behaviour of tissues and cells is often compared to that of foams and bubbles. Previous PhD-students (B. Dollet, C. Raufaste) focused on the flow of foam. Foams are convenient to study, because their constituents, the bubbles, can be easily visualised: they have a size of several millimetres to centimetres, and thus do not require microscopes. Tools have been developed to obtain statistical measurements on the bubbles (M. Aubouy, F. Graner, P. Marmottant, C. Quilliet ...). From these measurements, a mathematical model can be made, leading to the foams ‘constitutive equations’ (P. Marmottant, F. Graner, C. Raufaste), which can be solved to predict the foam’s behaviour (I. Cheddadi).

Collaborations between the foam researchers in the group and scientists outside Grenoble have proven important for this thesis as well. R. de Almeida, G. Thomas and M. Idiart from the *Instituto de Fisica* of the *Universidade Federal do Rio Grande do Sul* (Porto Alegre, Brazil) also study both foams and biological tissues, experimentally, numerically and theoretically; more particularly, they use the same numerical model, the Cellular Potts Model (CPM), as the one in this thesis.

During my master thesis at the Theoretical Biology and Bioinformatics group of Utrecht University (the Netherlands), I already used the CPM to study biological development. Many of the concepts of theoretical biology in general, and morphogenesis and the CPM in particular, I learned from my supervisors A. Marée and P. Hogeweg, and V. Grieneisen, who started a PhD in Utrecht. This allowed a flying start of my thesis: I have continued to use the simulation code developed by A. Marée, and have had regular discussions with V. Grieneisen and A. Marée concerning various CPM related issues.

The research was conducted in close collaboration with experimental labs. In order to understand the biology relevant for the morphogenesis of the *Drosophila* retina, I spent one month at Northwestern University (Evanston, Illinois, USA), with R. Carthew and T. Hayashi. A stay at the Max Planck Institute for Cell Biology and Genetics (MPI-CBG) in Dresden

(Germany) provided the opportunity to start a collaboration on cell sorting of the zebrafish germ layers with C.-P. Heisenberg and Y. Arboleda in this institute, and M. Krieg at the Biotec center of the *Technische Universität Dresden*, where I returned for two weeks. Frequent discussions with A. Mgharbel, H. Delanoë and J.-P. Rieu at the *Laboratoire de Physique de la Matière Condensée et des Nanostructures* (LPMCN) in Lyon on their experiments on cell aggregates were and still are important for the work on aggregate compression. In the meanwhile, B. Vianay and H. Guillou of the *Institut Néel* in Grenoble started to model individual cells on micro-patterned substrates with the CPM.

The winter school on the physics of liquid foams, in Les Houches (France) in January 2006 proved to be a useful starting point for a biologist to learn about the physics of foams. Several meetings and conferences focusing on modelling in biology (“Which mathematics for biology?”, Crete, July 2006; Satellite workshop on “Developmental Systems Biology” during the European Conference on Complex Systems in Dresden, October 2007; Symposium on the “Mathematical Modelling of Biological Pattern Formation” at the MPI-CBG in Dresden, December 2007; Workshop on “Multiscale Approaches in Cell Mechanics” in Autrans (France), January 2008; European Conference on Mathematical and Theoretical Biology in Edinburgh, June 2008) allowed to stay informed about other, related modelling work, and a course and a meeting focused at the interface of cell biology and biophysics (course “Cell Shape Changes”, *Institut Curie*, Paris, October 2007; GDR “CellTiss”, Arles, November 2007).

Introduction

1.1 Developmental biology

1.1.1 Morphogenesis

Developmental biology studies the processes that occur during the transition from a relatively simply shaped single cell to a usually much more complex adult organism (cf Figure 1.1). This usually involves growth, pattern formation, and morphogenesis.

Growth is the accumulation of mass. It is achieved through repetition of cell divisions and cell growth. Pattern formation (cf Figure 1.2) is the establishment of spatial motifs. Famous biological examples of patterns are

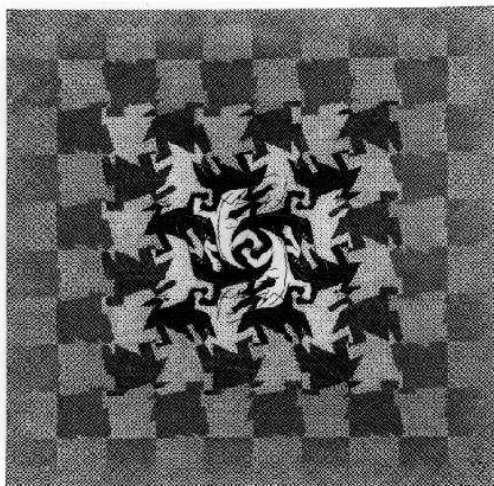


Figure 1.1: Development, M.C. Escher, 1937. An example of development without growth.

All M.C. Escher works (c) 2008 The M.C. Escher Company - the Netherlands. All rights reserved. Used by permission. www.mcescher.com

1. INTRODUCTION

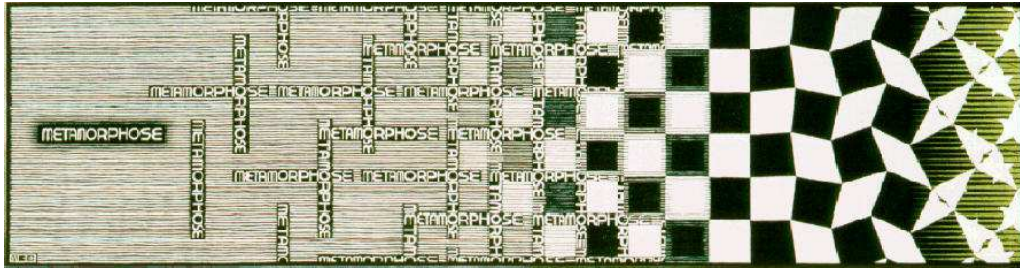


Figure 1.2: *Metamorphosis III*, M.C. Escher, 1967-1968: an example of pattern formation.

All M.C. Escher works (c) 2008 The M.C. Escher Company - the Netherlands. All rights reserved. Used by permission. www.mcescher.com

the stripes of the zebra, aggregation of cellular slime moulds, or the segmentation in the *Drosophila* embryo. Morphogenesis is the establishment of shape.

Growth, pattern formation and morphogenesis are governed by the genetic information, and a lot of effort in developmental biology consists in determining which gene does what, where and when. For a large part, this research has a chemical nature. Cells have to communicate with one another to exchange information, and a lot of communication is done through diffusible chemicals or direct receptor-ligand interactions. Cell type and fate can be determined chemically. But developing and maintaining a specific shape necessarily involves physics: work is done to go from one shape to another, objects deform or break when a large enough force is exerted, etc.

How objects react to forces, or what shape they attain as a result of their physical properties is the field of study of mechanics. People have studied for a long time the mechanical characteristics of single cells (Evans and Waugh, 1977; Thoumine and Ott, 1997; Thoumine et al., 1999; Guilak et al., 2002; Baaijens et al., 2005; Peeters et al., 2005; Trickey et al., 2006; Rosenbluth et al., 2006; Cuvelier et al., 2007). These studies pinpoint the importance of adhesion and the cytoskeleton for the mechanical properties. Both adhesion (Sato-Maeda et al., 1994; Merkel et al., 1999; Zhu et al., 2003; Perez et al., 2005; Leckband and Prakash, 2006) and the cytoskeleton (Janmey, 1991; Janmey et al., 1991; Lenormand et al., 2001; Brangwynne et al., 2006) have been subject to detailed biomechanical studies. Both also are involved in intercellular mechanotransduction (as reviewed by e.g. Janmey and McCulloch, 2007), and thus act on an intercellular level as well. On a larger scale, the shape of tissues is influenced by the adhesion and the

cytoskeleton (Pilot and Lecuit, 2005; Classen et al., 2005; Carthew, 2005; Lecuit and Lenne, 2007).

To understand how the cellular mechanical properties act collectively to determine the shape and morphogenesis of tissues is the motivation for this thesis. In the rest of this Section, we will have a closer look on cells and tissues, emphasising their physical properties. In Section 1.2, we introduce some physical concepts that are important in this thesis, and focus on liquids and foams. Liquids and foams are often used to understand the physical properties of tissues and aggregates, as introduced in Section 1.3.

1.1.2 The cell

1.1.2.1 Overview

The morphogenesis of animal tissues is the subject of this thesis. Tissues are composed of cells, which are the smallest subunits of an organism that are considered as alive. A cell contains all information necessary to reproduce itself, it produces its own energy, and its interior composition is highly regulated and distinctly different from the outside world.

Animal cells have a nucleus, mitochondria, endoplasmic reticulum, Golgi apparatus, membrane, and many more organelles, like other eukaryotic cells, but lack a cell wall. The cytoplasm contains many other molecules, notably numerous proteins, and multimolecular structures. The diameter of an animal cell is in the order of 10 to 100 μm .

The cell is active: it consumes energy. This energy is readily available to many processes as ATP (adenosine-tri-phosphate), which releases energy upon decomposition into ADP (adenosine-di-phosphate) and a phosphate. Other ways of energy transfer exist, but ATP is one of the most widely used energy carriers, and inhibition of the formation of ATP, or the inhibition of a protein to use ATP is a standard way to investigate the role of active processes in the cell.

The cell membrane is a phospholipid bilayer that contains a lot of proteins. The phospholipid bilayer is permeable for small, uncharged or weakly charged molecules; all other molecules have to pass through channels (formed by proteins) or are transported actively.

The cell's mechanical properties are mainly determined by the cytoskeleton (besides its role in intracellular transport), and the contacts between cells are mediated by adhesion molecules, as discussed hereafter.

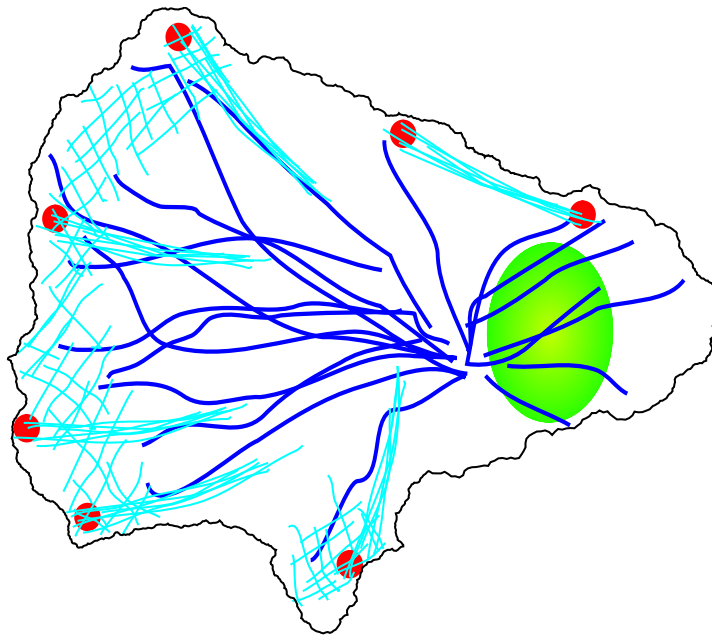


Figure 1.3: A schematic view of the cytoskeleton of a migrating cell. The nucleus is shown green, focal adhesions in red, and microtubules in dark blue. Of the actin filaments, in light blue, two types of organisation are shown: left, in the direction in which the cell moves, a gel-like network is present in lamellipodia; throughout the cell, associated with the focal adhesions, the filaments are oriented parallel and form stress fibres.

1.1.2.2 Cytoskeleton

The cytoskeleton accounts for a large part of the cell's ability to withstand forces and deformations. The main constituents are chains of proteins, which exist in three different types: microtubules, intermediate filaments and actin filaments (two of them are shown in Figure 1.3). Other molecules interact with these polymer chains, and thereby co-determine the cells' physical properties.

The composition and dynamics of these polymers are well described in cell biology textbooks, e.g. Alberts et al. (2002). Microtubules are the largest polymers, forming hollow cylinders of about 25 nm in diameter, made of globular tubulin monomers. One end of the microtubules is usually associated with the centrosome close to the nucleus, giving the microtubule organisation a star-like appearance (Figure 1.3).

Actin filaments (F-actin or microfilaments) are much thinner, with a diameter of 5 to 9 nm. The monomers are again globular (G-actin). Usually

two strands of monomers form a helix. Actin filaments occur throughout the cell, and can be organised in different ways. In lamellipodia and just underneath the cell membrane the filaments form a gel-like network; stress fibres are bundles of actin filaments, associated with focal adhesions (Figure 1.3).

Intermediate filaments are intermediate in diameter, around 10 nm. The proteins that form these filaments are filamentous themselves; in contrast to the microtubules and actin, different types exist (e.g. lamin, vimentin, keratin). They occur at several different places in the cells, and in different cell types.

Most filaments polymerise and depolymerise constantly. Actin filaments and microtubules are polar, having one end where polymerisation is more likely to happen, and the other where depolymerisation dominates. This is important in the establishment of polarity and coordinated movement of the cell, when all filaments are oriented in the same direction. There are numerous regulatory proteins acting on the stability of the filaments, affecting the (de-)polymerisation rates, and the nucleation of new filaments.

A wide range of cross-linking proteins is able to bind to two or more filaments, thus determining the filament organisation. A special case of cross-linking proteins are certain motor proteins, of which myosin II is perhaps the most well-known, that are able to move two filaments relative to one another.

Determining the contribution of the cytoskeletal components to the physical properties of the cell is not easy, due to the large number of interacting components. Janmey et al. (1991) studied the properties of gels of microtubules, actin filaments and vimentin intermediate filaments *in vitro*. Actin filaments are by far the most rigid, i.e. a gel of actin filaments deforms much less for the same applied strain than a gel of microtubules or intermediate filaments. Microtubules rupture easily, and are probably only important for the cell's mechanical properties when linked to other cytoskeletal filaments, while intermediate filaments are easy to deform at low stress rates, but become stiffer at high deformations.

Since then, a wide variety of biophysical techniques has been applied to the study of the properties of the cytoskeleton, *in vitro* and *in vivo*: magnetic and optical tweezers, atomic force microscopy, rheological methods (creep measurements, oscillating stress), passive microrheology (based on the diffusion of molecules). Particularly through *in vivo* studies, the effect of the the spatial organisation and the regulated interaction can be elucidated.

Brangwynne et al. (2006) showed that, *in vivo*, microtubules are highly resistant to compression because the surrounding cytoskeleton prevents them to buckle. As another example, Balland et al. (2005) used optical tweezers to oscillate beads attached to integrins at the outside of the cell. Integrins are connected to the actin cytoskeleton, so the stress exerted on the beads is transmitted to the cytoskeleton. Upon treatment with blebbistatin, that blocks the activity of myosin II, cells became softer, but also more fluid. When myosin II is active, it uses ATP to provoke a conformational change, which has as effect a movement of the binding site relative to the rest of the molecule. In this way it contracts an actin network, and is able to detach. In the presence of blebbistatin, myosin II can no longer use ATP, and can neither move nor detach. As a result, the actin network is less contracted, therefore softer; the position of the actin filaments is fixed, and the filaments do not slide past one another, therefore it is less fluid.

1.1.2.3 Cytoskeleton and the membrane

The cytoskeleton interacts with the membrane (reviewed by Doherty and McMahon, 2008): fibres more or less perpendicular to the membrane are responsible for membrane fluctuations and protrusions (Figure 1.3), and fibres parallel to the membrane support it. In many cells, a cortex of cytoskeletal fibres, mainly actin associated with myosin, exists. Biophysical experiments on the cell membrane demonstrate the importance of the cytoskeleton for the membrane behaviour.

The membrane tension can be determined by attaching a bead to the membrane, and pulling this bead with a (usually optical) tweezers (Dai et al., 1998; Dai and Sheetz, 1999; Raucher and Sheetz, 1999; Brevier, 2006). The tether, a small tube, can be several micrometres long, and the force required to keep the tether at a certain length does not depend on this length (Dai et al., 1998): the total area of the membrane can thus be increased to a certain extent without an increase in membrane tension. Furthermore, Thoumine et al. (1999) find that during cell spreading on an adhesive surface, the membrane area increases, but the membrane tension stays constant.

Both the tether pulling and the spreading experiments are in strong contrast with the behaviour of phospholipid vesicles: when increasing the vesicle size, the tension increases as well, and at 3% area increase the membrane ruptures (Israelachvili, 1991).

The cell membrane is believed to have numerous invaginations, from which material can be recruited to accommodate fast area changes, and on a longer term endo- and exocytosis regulate the amount of membrane

(Dai and Sheetz, 1999; Morris and Homann, 2001). These invaginations are accommodated by the underlying cytoskeleton, to which it adheres (Sheetz et al., 2006). The loss of cytoskeleton-membrane adhesion, or the destruction of the actomyosin cytoskeleton results in the formation of blebs (Paluch et al., 2005).

1.1.2.4 Cell adhesion

Cells can adhere to substrates, and cohere mutually. Adhesion to the substrates is mostly mediated by integrins, and by complexes called focal adhesions. Cell-cell adhesion is achieved by trans-membrane proteins or protein complexes, which are often linked to the cytoskeleton. In this thesis, we focus on cell-cell adhesion, which is mainly mediated by proteins from the cadherin family.

Several classes of cadherins exist; for reviews, see Gumbiner (2005); Halbleib and Nelson (2006). Most well known are the ‘classical cadherins’, to which E- and N-cadherin belong. Those are Ca^{2+} dependent, homophilic adhesion molecules. They are often organised in adherens junctions, which can occur as cadherin-dense patches on the membrane, or as belts in the case of epithelia (zonula adherens, see Figure 1.4).

At those junctions, α - and β -catenin are thought to link the intracellular domain of the cadherins to the cytoskeleton, but this link does not seem to be a direct physical one (Yamada et al., 2005). Nevertheless, catenins are often necessary for effective adhesion (Gates and Peifer, 2005). Besides, they have a multiplicity of other functions, varying from regulating actin dynamics (Drees et al., 2005) to interaction with several signalling pathways (Gumbiner, 2005).

Recently, Cavey et al. (2008) showed that two distinct populations of cadherin exist, one more stable than the other. The mobility of dense cadherin-patches is regulated by the α -catenin mediated actin-cadherin interactions. Besides the catenin-mediated ones, there are numerous other interactions between cadherins and the cytoskeleton (Mège et al., 2006; Kovacs and Yap, 2008). The cytoskeleton influences the strength and spatial organisation of the adherens junctions, and vice versa, adherens junctions influence the cytoskeleton composition and organisation, in ways that are starting to get elucidated (Kovacs and Yap, 2008).

Cadherins are mostly considered as homophilic, i.e. the different types only establish bonds with molecules of the same type. Why cadherins actually adhere homophilically is not clear. Duguay et al. (2003); Foty and Steinberg (2005) showed that cells expressing different cadherins mixed in the long term (four days), and Shi et al. (2008) were unable to find sufficient

1. INTRODUCTION

differences between homophilic and heterophilic interactions at the scale of one bond.

Other cadherin groups are not as well characterised. Protocadherins are supposed to have weak adhesive properties, but are nevertheless important in morphogenesis. Atypical cadherins like flamingo are important in signal transduction in the planar polarity pathways. The same molecules can act both as adhesion molecules and signal transducers: e.g., cells aggregate upon expression of flamingo (Usui et al., 1999).

Mechanically, adhesion is the establishment of bonds between molecules. An easy way to describe this is as an attractive force, or a potential energy that is diminished upon contact. Bell (1978) and Bell et al. (1984) showed that the physical action of the adhesion molecules depends on their chemical dynamics. As a result, the force required to separate adhesive cells depends on the speed of pulling, and mobile bonds may get concentrated in adhesive regions. Evans (1985a; 1985b) showed that there is a difference between viewing adhesion as a property that is continuous over the membrane, and viewing the adhesion molecules as sparsely distributed over the membrane; assuming a continuous distribution is only correct when the density of bonds is large enough. Later, single molecule force spectroscopy showed that the establishment and breaking of single bonds between large molecules and the forces associated to these events depends the speed of approach and separation (Merkel et al., 1999; Zhu et al., 2003; Evans and Calderwood, 2007).

How these physical and chemical properties of adhesion act in tissues is an open question. In tissues, cells are surrounded by other adhesive cells, and cadherins are organised into junctions where they interact with the cytoskeleton. This is difficult to study experimentally and theoretically, and to our knowledge, such studies do not exist. However, in studies of single cells on adhesive substrates, modelling adhesion as continuous attraction has shown to be successful (Frisch and Thoumine, 2002; Cuvelier et al., 2007).

1.1.3 Tissues

A tissue is a more or less homogeneous group of cells that performs the same function. Usually, organs consist of several tissues: e.g. the skin consists of epithelium, several types of connective tissue, blood vessels, etc., that all have their specific task and together accomplish the function of the skin as an organ (protecting the organism from the outside world).

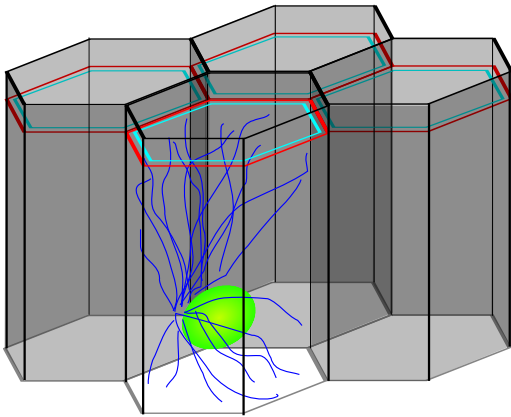


Figure 1.4: A schematic representation of four epithelial cells. The zonula adherens (red) is close to the apical surface (top), and is associated to the cortical cytoskeleton (light blue) consisting of actin and myosin. The nucleus (green) is usually found basally, and microtubules (dark blue) span the whole cell.

Some of the most well studied cases of tissue morphogenesis occur in epithelia, because they occur at the outside of the organism or of other tissues, and are thus much easier to visualise. An epithelium usually is a monolayer of cells, allowing it to be studied in 2D, which simplifies the visualisation even more. In an epithelium, the cells are often polarised as in Figure 1.4: adherens junctions and the associated cytoskeleton are concentrated in a zone near the apical surface.

Early in development, organs are not yet developed, and the organism just consists of several tissues (during the gastrula stage, those are typically ectoderm, endoderm, and mesoderm, but they again can be subdivided). A tissue thus consists of cells with similar behaviour, and are derived from the same mother cells.

Tissue morphogenesis is most striking when cells behave in a coordinated manner to achieve a shape change. Some of the most well known movements are invagination and convergent extension. Invagination (Figure 1.5) is the infolding of a sheet of cells. It is driven by a shape change of a group of cells that constrict apically, thereby folding the cell layer. The apical constriction has been shown to involve myosin II (Pilot and Lecuit, 2005; Quintin et al., 2008), and occurs likely in the zone of adherens junctions (Figure 1.5, insets).

Convergent extension occurs in tissue sheets or in 3D tissues (Keller, 2002): it is the elongation of a tissue in one dimension, that goes together

1. INTRODUCTION

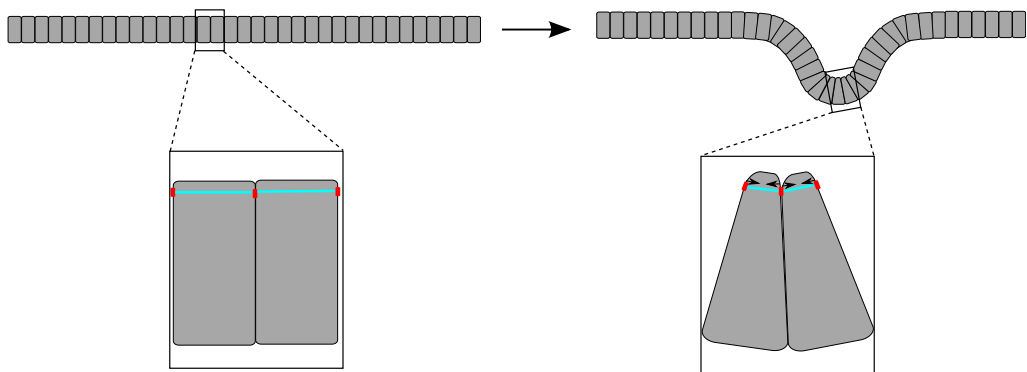


Figure 1.5: Invagination of a cell sheet. Insets show the shape change of the cells, that adhere to one another by means of adherens junctions (red), and have a contractile cortical cytoskeleton (light blue).

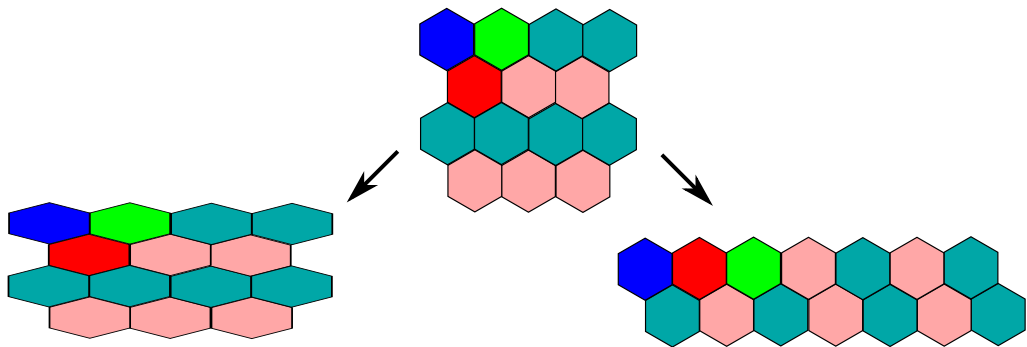


Figure 1.6: Two ways to extend a tissue (center) in one direction. Left, by stretching the cells, right, by intercalation.

with the shortening in another dimension (or two other dimensions). We illustrate two ways to stretch a 2D tissue in Figure 1.6. As in the case of invagination, tissue stretching can be a direct consequence of cell shape changes, if all the individual cells are stretched (Figure 1.6 left). However, often this is achieved by cells moving directionally in between each other, which is called intercalation (Figure 1.6 right). The tissue converges in one direction, and extends in the other, hence the term convergent extension.

As illustrated by these examples, a shape change of the tissue can be due to changes in cell shape, changes in cell rearrangement, or both. Other mechanisms may play a role too, such as directed cell divisions, cell death; these all highlight the cellular origin of tissue morphogenesis. Convergent extension can happen without any external force influencing the tissue

(Bertet et al., 2004); the cells thus generate themselves the force to change the tissue shape.

For convergent extension to happen, the cells need to be spatially coordinated. This information is often provided by proteins of the Planar Cell Polarity (PCP) pathway (Keller, 2002).

The players determining the physical properties of individual, isolated cells are again important in tissues: the cytoskeleton and adhesion (Bertet et al., 2004; Classen et al., 2005; Blankenship et al., 2006; Pilot et al., 2006). It is however difficult to separate both, as cadherin molecules and the cytoskeleton are linked in adherens junctions. In tissues, cell movements are dependent on active remodelling of the adherens junctions that involves the cytoskeleton (reviewed by Carthew, 2005; Lecuit, 2005).

In addition to such collective behaviour, Pezeron et al. (2008) show that cells exhibit a random walk during zebrafish gastrulation. Such individual cell movements often involve adhesion, as was demonstrated in border cell migration in the *Drosophila* oocyte, where E-cadherin is necessary for cell motility (Niewiadomska et al., 1999; Geisbrecht and Montell, 2002), or is the case in tumour metastasis (Halbleib and Nelson, 2006).

In ‘reconstituted tissues’, obtained by dissociation and subsequent re-aggregation of cells, adhesion seems to be the driving force for many types of observed behaviour, notably cell sorting (Steinberg, 1963; Duguay et al., 2003; Foty and Steinberg, 2005). Cell sorting seems to occur in *in vivo* development as well (reviewed by Gumbiner, 2005; Halbleib and Nelson, 2006). A popular interpretation of cell sorting is that cells act analogous to molecules in a liquid, with different cell types having different affinities (Steinberg, 1963; Beysens et al., 2000); we present this analogy in more detail in Section 1.3.1.

Another analogy that is used to interpret the behaviour of cells in tissues is to compare them to bubbles in foams (Thompson, 1942; Stein and Gordon, 1982; Chichilnisky, 1986; Hayashi and Carthew, 2004), as presented in Section 1.3.2. Both analogies are between biological and physical systems, and they are potentially interesting to understand how mechanical cell properties act on the tissue level. To understand both analogies, we need to understand both physical systems first.

1.2 The physics for this thesis in a nutshell

1.2.1 Forces, energy

The mechanical or physical concepts important for cells and tissues, and thus for this thesis, are described here. Some of the vocabulary is used in everyday life, and thus in biology as well, but with different meanings. This first Section 1.2.1 is meant to briefly illustrate the more or less familiar concepts involved in dealing with forces and energy; its goal is to avoid confusion in reading the rest of this thesis. The physicist can skip directly to Section 1.2.2, Section 1.2.3, or Section 1.3.

Mechanics is a science related to physics,* dealing with the forces, displacements and deformations of matter. We only look at soft matter, which is matter that is easily deformed under conditions that one encounters in everyday life: room temperature, atmospheric pressure, and forces that other soft objects exert. Most biological matter is soft matter.

The term ‘force’ has a meaning for everyone. ‘Stress’ is an internal force, which is exerted by one part of the material on other parts, and expressed in force per unit area. ‘Applied stress’ is the result of the application of a force.

The result of the application of a force on a solid object is likely a deformation. The ‘strain’ is a dimensionless deformation: e.g. the change in length, divided by the total length. How an object is deformed when it is subjected to a force, the stress-strain relationship, yields information about the object’s properties.

Energy is a quantity that is conserved during any action. It is an abstract concept, convenient to study how different physical processes interact. It is not directly measurable. One needs thus to calculate forces, displacements, temperatures, etc., to compare predictions made from energetic considerations to experiments.

Energy is conserved, which means that if something happens, one kind of energy might diminish, and one should always find that energy back in other forms. When one knows how much energy one can obtain by burning a certain amount of fuel, one can compare this energy to the energy (or work) required to displace a car, and calculate the amount of fuel needed to go from A to B. Likewise, energy can be stored and released later; an apple hanging in a tree has a potential energy, that is released and converted to kinetic energy when it starts falling; this kinetic energy again is released

*We do not strictly separate mechanics and physics in this thesis, and apologise to those who would like us to do so.

and transformed in something else (e.g. deformation of the apple) when it hits the ground.

There is energy that is not convertible into other energy, that can not be used to do work: heat. It is the ‘randomness’ of molecules. In all systems, when something happens, ‘useful energy’ is converted to heat, which is ‘useless energy’. Although the total energy is conserved, the useful energy diminishes. This stops when no more spontaneous changes are possible, because the useful energy is used: an equilibrium is reached. One should do something (add energy) for the system to continue evolving.

The apple that falls from a tree has a potential energy that is diminished when it falls; it is converted to kinetic energy. When the apple hits the soil, and it (or its pieces) halts. Suppose it did not break, then all kinetic energy is transformed into heat. Now, the apple does not move anymore, it is in mechanical equilibrium. For it to move again, someone should pick it up (thus adding energy) and let it fall, e.g. in the river next to the tree. The apple falls lower than it was, and eventually ends up in the sea. It has then diminished its potential energy even more. Thus, the previous equilibrium, of the apple lying on the ground, was a local equilibrium; after crossing an energy barrier, energy could be diminished further.

If one wants to know where an apple goes when it falls, without bothering about when it does so and at what speed, a simple thing to do is to regard only its potential energy (which on Earth is related to the height), and to minimise this. Finding the lowest point where the apple can go without temporarily increasing its height corresponds to finding a local energy minimum. One might be interested in other local minima in the neighbourhood; if someone kicks the apple, it might fall into one of them. Knowing if an energy minimum is the global energy minimum is usually not relevant; the apple will have been eaten before it reaches the global energy minimum.

Upon heating an ice cube, it melts. In the ice, every water molecule is tied to its fixed neighbours. Heating is a way to add energy, in this case internal energy, that makes the molecules move. When they move, they can escape from the crystalline arrangement in which they were kept in the ice. Even for water above 0°C , the minimum energy configuration of the water molecules is when they are bound to their neighbours. Above 0° the random motion of the molecules (their energy), is too large. Two water molecules tend to stay together, but they can not because their movements tear them apart; they will go on moving, forming bonds with other water molecules, that are broken by the movements, etc. Thus, between 0° and 100°C , the molecules stay more or less together as a liquid. Apparently, their random motions are not large enough to let them disperse themselves everywhere; it allows them to not stay in one minimal energy configuration (the ice), but to

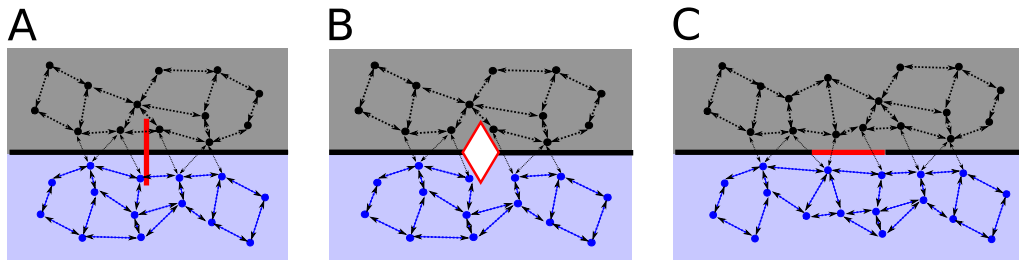


*Figure 1.7: Illustration of surface tension between oil (grey) and water (blue). Bonds between molecules over half a unit of surface have to be broken in both liquids (red line in **A**), giving rise to one unit of free surface in both liquids (red lines in **B**). Apposing these yields one unit of interfacial surface (red line in **C**).*

perpetually change from one (bond with a particular other water molecule) to another (bond with yet another water molecule) configuration.

The analogy with molecular movements is useful when treating other systems. Generally, the amount of molecular movements is correlated to the temperature, but a physically correct definition of temperature requires more subtleness. In what follows, random fluctuations that prevent the system from getting trapped in small energy minima are called ‘temperature’, and increasing these fluctuations corresponds to a higher temperature.

1.2.2 Liquids

In a fluid, the molecules move constantly with respect to one another: they diffuse. A fluid thus adapts to any shape that is imposed to it. Both gases and liquids are fluids; the difference between them is that liquids molecules stay more or less together, forming drops (or pools, when the volume of liquid is large enough to be influenced by gravity), while gas molecules do not.

Because the liquid molecules move constantly, the liquid flows if a stress, however small it may be, is applied. Due to the friction between the liquid molecules, a liquid can resist more or less to flow; this resistance is called viscosity. A liquid at rest has no internal stresses; the shape of a volume of liquid is fully determined by the surface tension and the gravity. In the following we consider drops small enough (below the capillary length), so the surface tension dominates gravity; we thus only introduce the effect of surface tension.

Surface tension (σ) occurs at the boundary of a liquid and another fluid, or a solid; it is the energy change associated with a change in surface area between the two. In Figure 1.7, we consider schematically two liquids, oil

(O) and water (W). The bond energy of a unit of surface between liquid i and j is e_{ij} . In order to create one unit of interface between O and W (Figure 1.7), bonds over half a unit of surface need to be broken in both liquids (requiring an energy $e_{OO}/2 + e_{WW}/2$), and are established over one unit of surface between the liquids (diminishing the energy by e_{OW}). The energy needed to make a unit of surface between O and W , the surface tension, is thus

$$\sigma_{OW} = \frac{e_{OO} + e_{WW}}{2} - e_{OW}. \quad (1.1)$$

For oil and water, σ_{OW} is positive: $e_{OO}/2 + e_{WW}/2 > e_{OW}$, i.e. the molecules of O and W on average have stronger bonds with alike molecules than with the molecules of the other species. They thus do not mix spontaneously; if mixed by force, they demix: energy minimisation requires that the interface be as small as possible.

For a water drop in contact with air (A), the bond energies between the air molecules and between an air and a water molecule are negligibly small; the surface tension now becomes

$$\sigma_W = \frac{e_{WW}}{2}. \quad (1.2)$$

This surface tension is always positive. The same holds for the air-oil surface tension σ_O (note that one usually drops the subscript A for air). If water and oil are mixed, they demix to minimise the interface oil-water. At the same time, the interfaces air-water and air-oil are diminished as well. The associated surface tensions σ_W and σ_O determine the relative positions of the oil and water with respect to the air. We know that $\sigma_W > \sigma_O$. If:

$$\sigma_W > \sigma_O + \sigma_{OW}, \quad (1.3)$$

oil surrounds the water drop; if:

$$\sigma_{OW} > \sigma_O + \sigma_W, \quad (1.4)$$

oil and water separate into two isolated drops. For any intermediate case:

$$\sigma_W - \sigma_O < \sigma_{OW} < \sigma_W + \sigma_O \quad (1.5)$$

the oil partially engulfs the water drop.

Imagine an oil for which this last case applies; then, a point where air, water and oil meet exists (Figure 1.8A). In this point, the surface tensions are in equilibrium, and the contact angles are found by applying Neumann's triangle:

$$\frac{\sigma_W}{\sin a} = \frac{\sigma_{OW}}{\sin b} = \frac{\sigma_O}{\sin c}. \quad (1.6)$$

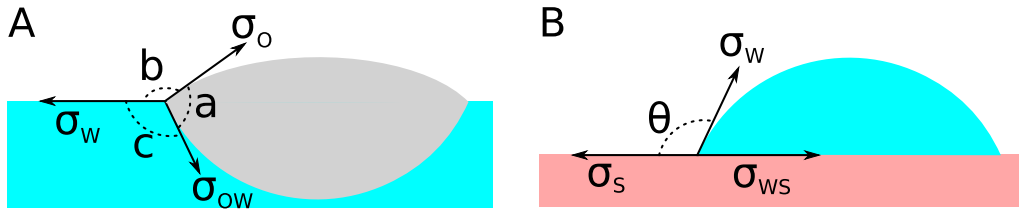


Figure 1.8: **A:** A drop of oil (grey) floating on water (blue). **B:** A drop of water on a solid surface.

For most oils, however, Eq. [1.3] applies: no equilibrium angle is possible, and the oil spreads on the water surface.

When a drop reposes on a solid surface (Figure 1.8B), the geometry is simpler, and the contact angle θ is found by applying the Young-Dupré equation:

$$\sigma_{WS} - \sigma_W \cos \theta = \sigma_S. \quad (1.7)$$

Again, if $\sigma_S > \sigma_W + \sigma_{WS}$, no equilibrium angle exists, and the drop spreads as a thin film on the solid surface, a phenomenon called ‘wetting’.

Below the capillary length, the shape of an interface between a liquid and another fluid is determined by the surface tension. Surface tension minimises the interface, constrained by the volume. The drop’s surface is thus a minimal surface that is curved, with its mean curvature being equal everywhere. As illustrated in Figure 1.8, the surface tensions of the interfaces determine their curvature.

1.2.3 Foams

1.2.3.1 Structure at equilibrium

A single bubble, floating in the air, is spherical; a sphere has the smallest possible surface area for a given volume. This shape is due to surface tension, as in drops (Section 1.2.2). A soap bubble is stable because the soap, a soluble surfactant, diminishes the surface tension of the water and stabilises the water film. When the surface shrinks or expands, surfactant molecules go in or are recruited from the liquid solution. The density of surfactant molecules thus stays more or less constant, and so does the surface tension. The total surface energy varies linearly with the surface, and energy minimisation boils down to surface minimisation.

This also applies in foams, that are merely collections of bubbles. All interfaces between the bubbles form one continuous network (cf Figure 1.9), and surfactant molecules can diffuse freely in this network. All interfaces

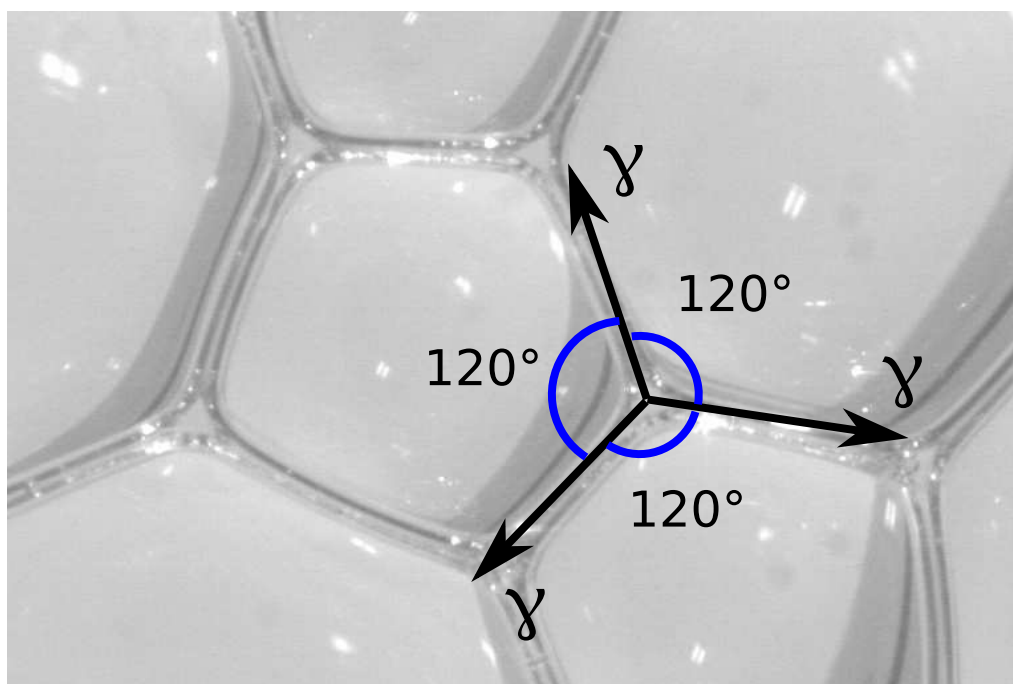


Figure 1.9: Detail of a foam, photo courtesy of S. Courty.

thus have the same chemical composition, and the same surface tension. As a consequence, energy minimisation in a foam also boils down to overall surface minimisation, limited by the volume of each individual bubble.

Plateau (1873) found that, as a result of surface minimisation, films separating bubbles meet by three, and the angles with which the films meet are equal. In the photograph of a bubble monolayer in Figure 1.9, the films themselves are thin, and the vertex where three films meet is a small triangle where most of the liquid is concentrated, known as the Plateau border. Because the tension in the three films is equal, the equilibrium configuration around the vertex has three equal, 120° angles.

Indeed, it can be shown mathematically that in a vertex where four films meet, the total surface can always be reduced by replacing the four-film vertex by two three-film ones. To reproduce the mathematical proof (Almgren and Taylor, 1976) would be beyond the scope of this thesis; a simple illustration is shown in Figure 1.10, where a rectangle is partitioned in four. If the sides of the rectangle are of length $a = 3$ and $b = 4$, then the total length of the lines needed to partition the rectangle as a function of

1. INTRODUCTION

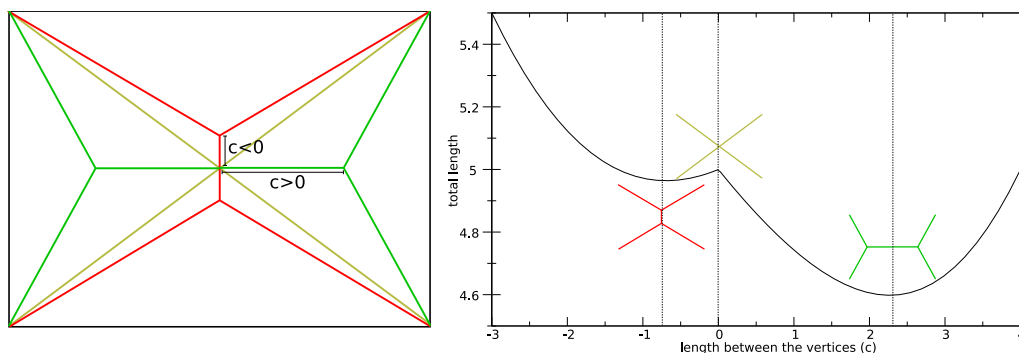


Figure 1.10: Partitioning of a rectangle using minimal lengths. The line segments are fixed in the corners of the rectangle, and are free to move elsewhere. Left: three possible ways of partitioning. The height:width ratio of this rectangle is 3 : 4. $|c|$ is the distance of the vertices to the centre; we choose c to be negative for the red configuration, and positive for the green one. If $c = 0$, there is only one four-way vertex. Right: the total length needed to partition the rectangle, as a function of c .

the distance $|c|$ of the vertices to the rectangle's centre is:

$$L = \begin{cases} 4\sqrt{\left(\frac{a}{2} - |c|\right)^2 + \frac{b^2}{2}} + 2|c| & \text{if } c \leq 0 \\ 4\sqrt{\frac{a^2}{2} + \left(\frac{b}{2} - |c|\right)^2} + 2|c| & \text{if } c > 0 \end{cases}.$$

This length L is plotted in Figure 1.10(right). The configuration associated to the four-way vertex, at $c = 0$, has a higher total length than either of the both configurations with two three-way vertices. If the aspect ratio of the rectangle deviates more from 1 than in this example, only one configuration with two three-way vertices has a shorter length than the four-way vertex one. In general, it is thus always possible to reduce the total length by replacing a four-way vertex by two three-way vertices.

As can be seen in Figure 1.9, the films are not always straight. The curvature is determined by the number of sides a bubble has, and is related to the pressure differences that exist between the adjacent bubbles; see e.g. Weaire and Hutzler (1999).

Euler's equation relates the number of bubbles B to the number of sides S and the number of vertices V ; in 2D, it is:

$$B - S + V = 1 \tag{1.8}$$

The constant at the right hand side can be another small integer number, depending on the boundary conditions of the bubble monolayer. We can

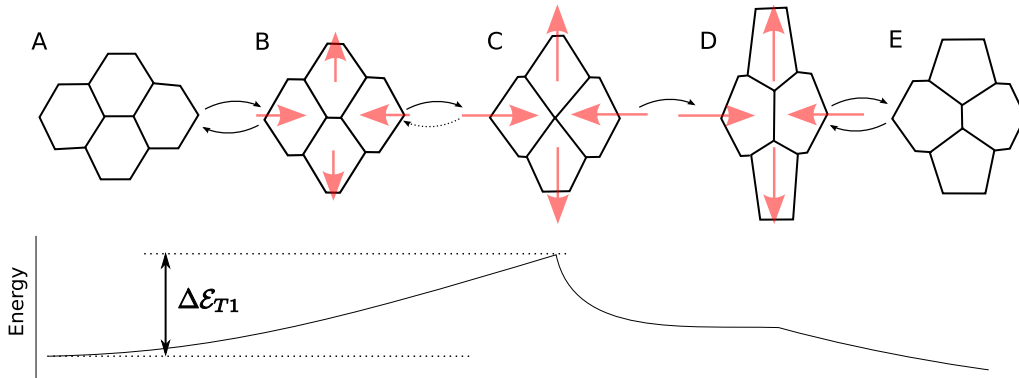


Figure 1.11: A schematic representation of a detail of a foam in extensional shear. The pink arrows indicate the directions of the applied stress. **A**: Bubbles in a foam at rest. **B**: Upon application of a small stress. **C**: An unstable four-fold vertex. **D**: The bubbles have swapped neighbours, and have adopted a new configuration. **E**: A new stable configuration after relaxation. Bottom: a schematic representation of the energy changes during this rearrangement. Two sudden changes in the energy are visible, the first one immediately after the four-fold vertex (**C**) is formed, the second one when the stress is no longer applied.

calculate $\langle n \rangle$, the average number of sides per bubble, as follows. Each side separates two bubbles: $B/2 = S/\langle n \rangle$. Each side connects two vertices; now, Plateau's rules determine the number of sides (3) that join in a vertex; this yields $V/2 = S/3$. When we consider a lot of bubbles ($B \rightarrow \infty$), we can neglect the constant at the right hand side, and we find that $\langle n \rangle = 6$. Euler's equation is very general, for all space tiling patterns; its use with Plateau's rules allows to make predictions in foams, which in fact hold for any pattern where sides join by three.

The *average* number of sides of a bubble is six; this does not allow to make statements of the number of sides regarding an individual bubble in the foam. Many metastable states exist, in which there are only three-film vertices, and the number of sides per bubble can vary (De Almeida and Iglesias, 1989; Graner et al., 2001; Quilliet et al., 2008). Therefore, only seldom, a foam reaches the absolute minimal surface. This also makes it very hard to predict theoretically what this absolute minimal surface is.

1.2.3.2 Foam dynamics

When applying a stress, the foam deforms. In the deformation that results from this stress, three regimes can be distinguished (Höhler and Cohen-

Addad, 2005; Marmottant and Graner, 2007). For small stresses, the deformation is elastic, which means that the foam regains its original shape when the stress disappears. When one applies more stress, one sculpts the foam: it keeps the new shape, or at least does not return to the original one. This is called plasticity. Finally, when we keep on applying a stress, the foam flows. If the stress is high, the deformations are fast, and the viscosity of the foam's liquid fraction plays a role.

These properties can be understood by looking at the foam at the scale of a single bubble and its direct neighbours, Figure 1.11. At small stress, the bubbles will be deformed, as in Figure 1.11B. When the stress disappears, the bubbles go back to their original shape (Figure 1.11A). At larger stress, the bubbles get increasingly deformed, until interfaces disappear, and three-bubble vertices merge with each other to create a four-bubble vertex (Figure 1.11C). Because a four-bubble vertex is always unstable (see Section 1.2.3.1), this configuration immediately relaxes to form again two three-bubble vertices (Figure 1.11D). Once the bubbles are in this configuration, they do not go back to Figure 1.11A when the stress disappears, but instead relax to Figure 1.11E.

The configurations of Figure 1.11A and E are topologically different: a neighbour change has occurred. During such a rearrangement of bubbles, called T1, the total number of bubbles stays constant. There are other kinds of topological events, during which the number of bubbles changes, e.g. the creation or disappearance of a bubble (T2). The changes in the foam from Figure 1.11A to B are geometrical rather than topological; the same from Figure 1.11D to E.

The four-bubble state in Figure 1.11C has the largest total surface of the sketches in Figure 1.11, and it thus has the highest energy. It acts as an energy barrier $\Delta\mathcal{E}_{T1}$ between the states in Figure 1.11A,B and D,E: stress needs to be applied to overcome this barrier. This stress is called the yield stress, which is a threshold stress separating the purely elastic behaviour from the plastic behaviour that involves rearrangements. The corresponding maximal deformation of bubbles before a rearrangement takes place is called the yield strain. The rearrangements are irreversible, because the energy required to provoke them, that was stored by the increase of surface as the foam went from Figure 1.11A to C, is lost (dissipated as heat) between Figure 1.11C and D.

Dollet et al. (2005); Raufaste (2007) blow foam through a channel with an obstacle or a constriction. The foam is able to flow around the obstacle, or through the constriction, because of the rearrangements of bubble. The foam's behaviour is then fluid-like. Foam flow is, however, different from the flow of a so-called 'newtonian' fluid, like water. This is due to the

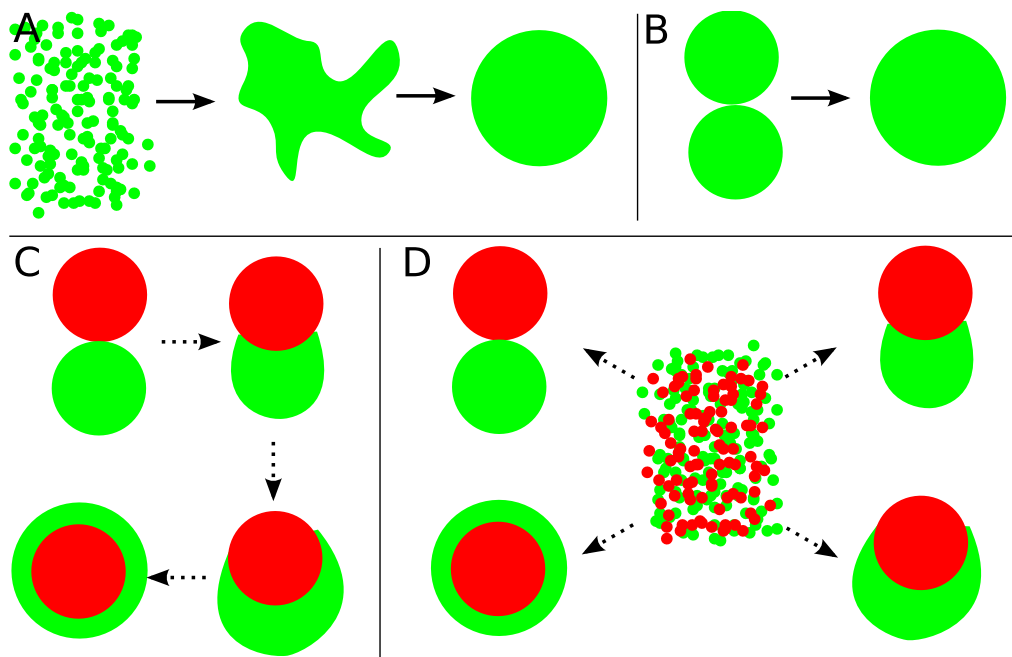


Figure 1.12: A schematic representation of the behaviour of dissociated and reaggregated cells. **A:** Dissociated cells from an aggregate that rounds up. **B:** Two aggregates of the same cell type fuse. **C:** When bringing two aggregates of different types in contact, they either stay separated, or one engulfs the other partially or totally. Arrows thus indicate possibilities; each drawing can be a final state. **D:** Upon dissociation and mixing of two cell types; the final states are equal to those reached by fusion (C).

deformability of the bubbles and way in which the bubbles rearrange (Figure 1.11).

1.3 Analogies between biological and physical systems

1.3.1 Liquids and cellular aggregates

To study how a large assembly of cells behaves, one can study them *in vitro* (Figure 1.12). Cells belonging to one or more cell types are dissociated, and are allowed to re-aggregate. Upon dissociation, positional information (e.g. through chemical gradients) and orientation (e.g. planar cell polarity,

which often requires cell-cell contact) is lost, and all pattern formation is *de novo*, independent of any prepattern.

When cells of only one type are dissociated and allowed to reaggregate, they form a round aggregate (Figure 1.12A); two aggregates of the same type (homotypic aggregates) fuse when brought into contact (Figure 1.12B).

If two aggregates of cells of different types (heterotypic aggregates) are dissociated and mixed, they sort out. Either all cells of one type end up in the center, surrounded by those of the other type, or they separate again, totally or partial (Figure 1.12D). When two non-dissociated aggregates are brought into contact (Figure 1.12C), either one aggregate envelops the other completely, or the envelopment is incomplete, or nothing happens. But in most cases, cell sorting experiments lead to the same final configurations as the aggregate fusion experiments.

Steinberg (1963) proposed that this behaviour was due to differences in adhesion between cells of different types, in what has become known as the Differential Adhesion Hypothesis (DAH). In the DAH, cells are considered analogous to the molecules in a liquid, and cell sorting as analogous to the separation of two immiscible fluids (Beysens et al., 2000). As introduced in Section 1.2.2, in liquids, the surface tensions determine the shape of drops (round), miscibility, and the final configuration of mixed liquids. A liquid's surface tension is due to the difference between bonds with like and unlike molecules (Eq. [1.1]); the stronger the bonds between molecules, the higher the liquid's surface tension. The positions of both cell types in Figure 1.12C and D can be explained by applying Eq. [1.3]-[1.5].

According to the DAH, a cell aggregate has a surface tension that is determined by the adhesion between cells. The DAH predicts that 1) stronger adhesion gives rise to a higher surface tension, and 2) this surface tension determines the result of cell sorting.

Foty et al. (1994) introduced the 'parallel plate compression apparatus' (described in more detail in Chapter 5), which allows to measure the surface tension of an aggregate. They indeed showed that the aggregate with the lower surface tension envelops the one with the larger tension. This is true for multiple aggregates as well: an aggregate with a high surface tension is enveloped by any aggregate with a lower tension (Foty et al., 1996). These findings confirmed the second part of the DAH.

To confirm the first part of the DAH, Foty and Steinberg (2005) correlated the number of adhesion molecules per cell to the surface tension of the aggregates, and found a linear relation. They conclude:

“We have here measured both (1) the number of surface cadherins per cell and (2) the surface tensions of aggregates of cells

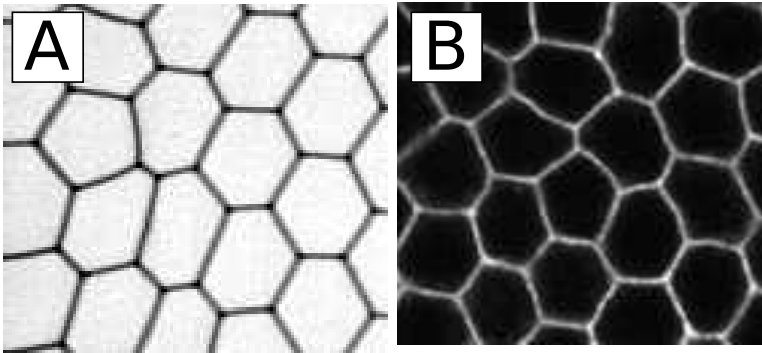


Figure 1.13: Visual resemblance between foams and tissues. **A:** Snapshot of a 2D foam flow, courtesy M. Asipauskas. **B:** Epithelial tissue, reprinted from *Developmental Cell*, Vol. 11(4), Blankenship et al., *Multicellular Rosette Formation Links Planar Cell Polarity to Tissue Morphogenesis*, pp. 459-470, copyright 2006, with permission from Elsevier.

of each cell line and report that the latter parameter is specified almost entirely by the former one, as postulated in the DAH. (...) We regard this as the final verification of the explanation of “tissue affinities” proposed in the DAH.”

As, however, science does not rely upon verifications but upon falsifications and subsequent new falsifiable hypotheses (Popper, 1960), we will see in Chapter 4 that the DAH can be falsified and should be substituted by a more complete ‘hypothesis’.

1.3.2 Bubbles and tissues

The comparison of cells with bubbles is repeated throughout the history of cell biology. Important is the book “On Growth and Form” by Thompson (1942), first published in 1917. A part of this book is dedicated to the comparison of tissues and bubbles, inspired by the work on thin liquid films by Plateau (1873) (see Section 1.2.3.1). Thompson shows many examples of biological tissues resembling clusters of soap bubbles, and argues that this analogy is due to surface minimisation. He also discusses many examples of tissues where this principle of surface minimisation seems to apply, but under constraints: interfaces might have different surface tension, the relaxation of shape might be constrained by underlying membranes, etc.

Indeed, tissues and clusters of soap bubbles can bear striking resemblances. Figure 1.13 shows two pictures that have little in common, but

resemble each other: a foam flowing between two glass plates (Asipauskas et al., 2003) and the germ band of a *Drosophila* embryo (Blankenship et al., 2006). Besides Thompson (1942), this kind of visual analogy has led several other authors (Chichilnisky, 1986; Hayashi and Carthew, 2004; Lecuit and Lenne, 2007; Sun, 2007) to suggest that cells, mainly in epithelial tissues, might be minimising their surface. This suggestion will be tested in Chapter 3.

When a cell is put on a surface to which it adheres, it spreads (Thoumine et al., 1999; Cuvelier et al., 2007): it thus seems strange to describe adhesive cells as surface minimising entities. When comparing cells with bubbles, one finds that they are indeed very different: bubbles are passive, they are volumes of gas surrounded by water and surfactant molecules. Cells, on the other hand, are active and consume energy, they have an inner structure, and their membrane is highly organised. Furthermore, at a bubble-bubble interface, there is one liquid layer, and this film is continuous with the films at other interfaces: in a bubble cluster, there is only one liquid film. Each cell, however, has its own membrane. The cell membrane is associated to the cytoskeleton, which is responsible for the cortex rigidity, as well as for the fluctuations of the membrane.

It is thus obviously a gross simplification to describe cells, with their intricate organisation and multitude of different molecules, as bubbles. The analogy is found on a larger scale: like bubbles in a foam, cells in tissues tile the space without gap nor overlap (Figure 1.13). In foams, the space-tiling arrangement of bubbles determines its static structure (Section 1.2.3.1) and dynamics (Section 1.2.3.2). The physical characteristics of individual cells might be completely different from the characteristics of bubbles, the fact that both are organised in similar ways at the collective level makes the use of tools from foam physics interesting for biology. It is thus not the individual cells and individual bubbles that are analogous, but the collections of cells (tissues, aggregates) and collections of bubbles (foams).

1.4 This thesis

In this thesis, we use the analogy with foams to study tissues and aggregates. We assume that it is a useful analogy, but up to what extent? What new insights can it give us in biological morphogenesis? More specifically, can we infer, qualitatively or quantitatively, cellular properties from collective observations (images, forces)?

We study three specific examples: the retina of a developing *Drosophila* (Chapter 3), sorting of zebrafish germlayer cells (Chapter 4), and the com-

pression of aggregates of embryonic cells (Chapter 5). The examples are thus biological, the tools we use are derived from foam physics. The main tools in this thesis are computer simulations; some basic concepts and theories in foam physics are useful as well; the use of a mathematical model is introduced in Chapter 5.

1.5 Résumé français

La morphogenèse, l'établissement de la forme spécifique d'un organisme, est déterminée par les propriétés physiques des cellules. Ces propriétés sont principalement dues au cytosquelette, responsable de la rigidité de la cellule, et à l'adhésion. Pour étudier comment les propriétés physiques des cellules agissent au niveau d'un tissu, on trouve plusieurs analogies avec des systèmes physiques dans la littérature.

Quand les cellules d'un embryon sont dissociées, elles se réaggrègent grâce à l'adhésion. Si les cellules sont toutes du même type cellulaire, elles forment souvent des agrégats sphériques. Ceci ressemble au comportement d'une goutte liquide, qui est sphérique à cause de la tension de surface.

Si on mélange les cellules dissociées de deux types cellulaires, elles se réaggrègent également, et en plus on observe souvent une séparation des deux types, ce qu'on appelle le tri cellulaire. Ceci ressemble à la démixion de deux liquides immiscibles (eau et huile, par exemple). Dans les cellules, les positions finales qui résultent du tri sont prédites par la tension de surface de l'agrégat, comme pour les liquides.

Les analogies avec les liquides ont donné naissance à l'Hypothèse d'Adhésion Différentielle (*DAH* en anglais). Les énoncés de cette hypothèse sont : 1) pour prédire le résultat final d'une expérience de tri, il suffit de mesurer la tension de surface des agrégats (homotypiques) des deux types de cellules, et 2) cette tension de surface est plus grande si l'adhésion cellulaire est plus forte.

Une autre analogie avec un système physique est celle entre cellules et bulles de savon, qui est née à partir de la ressemblance visuelle entre tissus et mousses. Les bulles dans une mousse pavent le plan sans trou ni recouvrement, et minimisent leur surface. Les cellules pavent le plan dans certains cas, comme on peut le voir souvent dans les épithélia, par exemple. Il est cependant peu probable que les cellules, avec leur activité, cytosquelette et adhésion, ont les mêmes propriétés physiques que les bulles.

Dans les mousses, le pavage de l'espace par les bulles détermine, en partie, les propriétés physiques. Les bulles peuvent se déformer et se réarranger, et la mousse est donc un matériau élastique et plastique à la fois ; en plus,

1. INTRODUCTION

les parois liquides donnent la mousse une viscosité. Comme les cellules dans un tissu peuvent également se déformer, se réarranger, et contiennent du liquide, un tissu pourrait avoir des propriétés comparables.

Dans cette thèse, nous étudions l'effet des propriétés physiques des cellules au niveau collectif. Jusqu'où l'analogie avec les mousses est-elle utile ? Peut-on déduire les propriétés des cellules à partir des observations collectives (images, forces) ?

The Cellular Potts Model (CPM)

2.1 Context

The Potts model and its predecessor, the Ising model, have been developed in statistical mechanics to study magnetisation and phase transitions. The “large- Q Potts model” is used to study a large number (Q) of interaction domains. In the name “Cellular Potts Model” (CPM), ‘cellular’ does not refer to biological cells, but is a general term for systems that consist of coherent domains. In this model, cells are described as deformable, space tiling objects, and interfacial energies are assigned to their boundaries.

The CPM has been applied to studies in several fields of physics before its use in biology, such as grain growth in metals, or coarsening in foams (Glazier et al., 1990). While focusing on the analogy between tissues and foams in this thesis (cf Section 1.3.2), the application to foams is most useful for us. Recently, several studies have highlighted the versatility of the model, treating the (albeit slow) dynamics of foam flow (Raufaste et al., 2007), and modelling large numbers of bubbles to yield statistical data (Thomas et al., 2006).

The CPM has been introduced in biophysics by Graner and Glazier (1992) and Glazier and Graner (1993) to study cell sorting. These first simulations correctly reproduced not only the final configurations of the cell types, but also the dynamics of cell sorting, i.e. the evolution of the contact lengths between the cell types. The fluctuations of the cells’ interfaces are sufficient to let cells rearrange, and find the minimal energy configuration (Graner, 1993; Glazier and Graner, 1993). Since then, studies focusing both on the properties of the CPM (which we will cite later, when applicable), and of biological problems using the CPM have been published. E.g., Mombach et al. (1995) correlated the simulated fluctuations to those observed experimentally in cells, Ouchi et al. (2003) focused on the diffusion of cells in cell masses. Käfer et al. (2006) showed that differential adhesion interacts with chemotaxis, in a way that depends on the cells

2. THE CELLULAR POTTS MODEL (CPM)

being deformable objects. In physiological contexts, the model has been applied to the study of cancer (e.g. Bauer et al., 2007) and the immune system (Beltman et al., 2007).

A striking application is the almost complete modelling of the aggregation and fruiting body formation of the cellular slime mould *Dictyostelium discoideum*. Single cells aggregate by chemotaxis and form crawling slugs. During these first stages, cell sorting takes place, as modelled by Savill and Hogeweg (1997). Marée et al. (1999a,b) extended the model of the slug, and finally modelled the fruiting body formation (Marée and Hogeweg, 2001, 2002). Marée et al. (2007) give an overview of the use of the CPM for several biological problems. These studies highlighted the importance of differential adhesion, and showed how physical processes can provide the information for morphogenesis.

Other methods of simulation are available. In foams, the use of finite element models such as the Surface Evolver (Brakke, 1992) is very popular. They can precisely model the shape of bubbles, but are computer-intensive, while the CPM is useful for obtaining large statistics; for an example of the use of both, see Raufaste et al. (2007). An advantage of the CPM for the simulation of biological cells is its use of a “temperature”, which describes the cells’ fluctuations (Graner, 1993; Glazier and Graner, 1993; Mombach et al., 1995), while bubbles do not fluctuate.

Methods simplifying the description of cells by only looking at their centres of mass or at the vertices are computationally efficient, because only one equation per vertex or center is needed. They are useful in cases where the cell boundaries are approximately straight. However, for shapes as those modelled in Chapter 3, the highly curved boundaries and elongated cells would be difficult to incorporate in the equations of the evolution of the vertices or centres.

2.2 Algorithm

2.2.1 Energy

In a lattice (Figure 2.1), a cell is a set of pixels (lattice sites) with the same number. The organisation of these numbers on the lattice thus give the size and the shape of the cells.

An energy is assigned to the interfaces and the cells

$$\mathcal{E} = \sum_{\text{interfaces}} E_{ij} + \sum_{\text{cells}} U_i, \quad (2.1)$$

4	4	4	4	4	3	3	3	3	3	3
4	4	4	4	4	3	3	3	3	3	3
4	4	4	4	2	2	3	3	3	3	3
5	4	4	2	2	2	2	2	3	3	0
5	5	2	2	2	2	2	2	0	0	0
5	5	2	2	2	2	2	0	0	0	0
5	5	2	2	2	2	0	0	0	0	0
5	5	5	2	2	2	1	0	0	0	0
5	5	5	1	1	1	1	1	0	0	0
5	5	5	1	1	1	1	1	1	0	0

Figure 2.1: A small CPM lattice with 5 cells (coloured) and medium (white).

where E_{ij} is the interfacial energy between cell i and j , and U_i some energy of the cell i itself. This function is a Hamiltonian. For the simulation of cell sorting in 2D, Graner and Glazier (1992) assigned an interfacial energy density γ_{ij} to each contact between two lattice sites belonging to different cells, and used U_i to describe area (the 2D equivalent of volume) conservation:

$$\mathcal{E} = \sum_{\text{interfaces}} P_{ij} \gamma_{ij} + \sum_{\text{cells}} \lambda_A (A_i - A_{0i})^2, \quad (2.2)$$

where P_{ij} is the length of the interface between cells i and j ; P_{ij} is the sum of all pixels of cell i that have a neighbouring pixel that belongs to cell j . A_i is the area of a cell i , A_{0i} its target area (minimum-energy area), and λ_A an area compression modulus. This energy function is used in most studies of biological cells with the CPM, and is applicable also in three dimensions. The extracellular medium (white in Figure 2.1) simply has no area conservation term.

2.2.2 Lattice

We have to define which pixels are neighbours to one another. A simple choice is to consider pixels that touch as neighbours; those are either the first order neighbours (labelled ‘I’ in Figure 2.2a), or both the first and second order neighbours (‘I’ and ‘II’ in Figure 2.2a). The latter have a larger distance to the center pixel ($\sqrt{2}$) than the former (1). This choice influences the lattice anisotropy (Glazier et al., 1990; Holm et al., 1991;

2. THE CELLULAR POTTS MODEL (CPM)

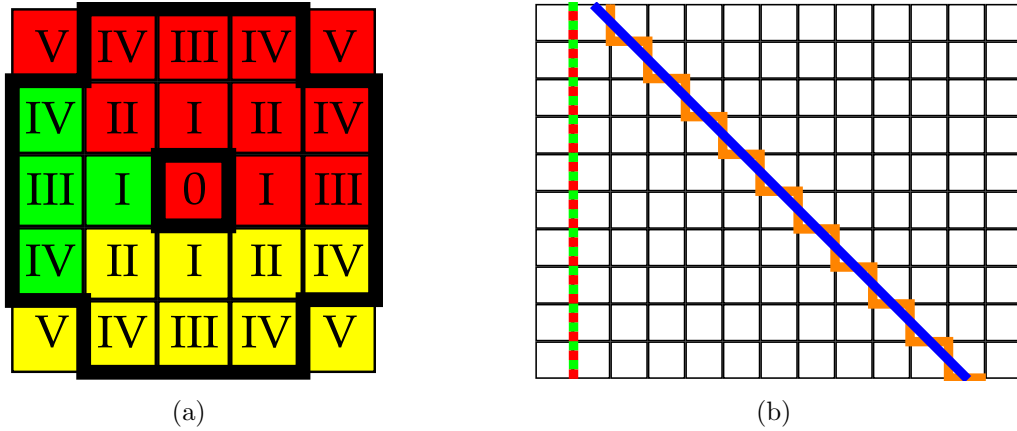


Figure 2.2: a) The neighbourhood of a pixel (marked ‘0’) in a 2D square lattice. First order neighbours are marked ‘I’, second order neighbours ‘II’, etc. The colours represent different cells. The thick line indicates the neighbourhood used for most simulations in this thesis. b) Lattice anisotropy or ‘how to measure the length of a line?’ The green and blue lines show two possible orientations of interfaces, the red and orange lines their representation on a lattice. The green and red line overlap.

Marée et al., 2007; Raufaste, 2007). When using Eq. [2.2], the energy associated to an interface should depend only on its length, not on its orientation. Calculating the energy associated to a vertical interface (green in Figure 2.2b) is easy: we just count its length (10 pixels, red line in Figure 2.2b), and multiply it by γ_{ij} . An interface with an orientation of 45° (blue line in Figure 2.2b) is represented on the lattice as illustrated by the orange line. Adding the length of all segments of the orange line yields a length of 20 pixels, while the blue line has a length of $10\sqrt{2}$ pixels. If we only take first order neighbours (‘I’) into account, we thus overestimate the energy of an interface oriented by 45° by a factor $\sqrt{2} \approx 1.41$.

Increasing the number of pixels considered as neighbours decreases this lattice anisotropy (Glazier et al., 1990; Holm et al., 1991; Marée et al., 2007; Raufaste, 2007). However, it increases the number of interactions that have to be taken into account in the calculations, thereby increasing simulation time. When using interactions up to the fourth order neighbours (‘I’ to ‘IV’ in Figure 2.2a), the overestimation of the energy associated to an interface oriented at 45° is only a factor 1.027 (Raufaste, 2007). This is the compromise we choose.

Note that it is the orientation of the neighbours that counts for the lattice anisotropy (F. Graner, unpubl.). The third order neighbours ('III') are oriented in the same direction as the first order ones ('I'), and adding the third order neighbours does thus not diminish the anisotropy, while it increases calculation time. The precise effect of leaving them out has not been tested here, and we have included them for simplicity.

2.2.3 Energy minimisation

The algorithm to minimise the energy \mathcal{E} uses Monte Carlo sampling and the Metropolis algorithm, as follows. In the lattice, we randomly draw (without replacement) a pixel (which has number i), and randomly choose one of its eight neighbouring pixels (number i'); if both pixels do not belong to the same cell ($i \neq i'$), we try to copy the state of the neighbouring pixel to the first one ($i \rightarrow i'$).

If the copying diminishes the energy \mathcal{E} , we accept it; and if it increases \mathcal{E} , we accept it with probability

$$p = \exp(-\Delta\mathcal{E}_{i \rightarrow i'} / \xi) . \quad (2.3)$$

$\Delta\mathcal{E}_{i \rightarrow i'}$ is the difference in \mathcal{E} that would result from the considered copying, and the random copying allowance ξ (playing the role of an effective temperature) determines to which extent we allow energy-increasing copy events, leading to membrane fluctuations (cf Mombach et al. (1995); Käfer et al. (2006)). As in most other studies using the CPM, one Monte Carlo time step (MCS) is defined as the number of random drawings equal to the number of lattice pixels.

To apply the energy function (Eq. [2.2]) on a lattice with cells (cf Figure 2.1) we calculate

$$\mathcal{E} = \sum_{\text{lattice sites } i} \sum_{\text{neighbour sites } j} (\delta_{ij} - 1) \gamma_{ij} + \sum_{\text{cells } i} \lambda_A (A_i - A_{0i})^2 , \quad (2.4)$$

which expresses that for every pixel (which has number i) in the lattice, we add the interaction energy $(\delta_{ij} - 1) \gamma_{ij}$ with each of its neighbour pixels (with number j). δ_{ij} is the Kronecker symbol; it is 1 if $i = j$ (i.e. i and j belong to the same cell), and 0 otherwise.

When using the total energy as defined in Eq. [2.4], counting the number of neighbouring pixels that cell i loses and the cell i' gains in the local

2. THE CELLULAR POTTS MODEL (CPM)

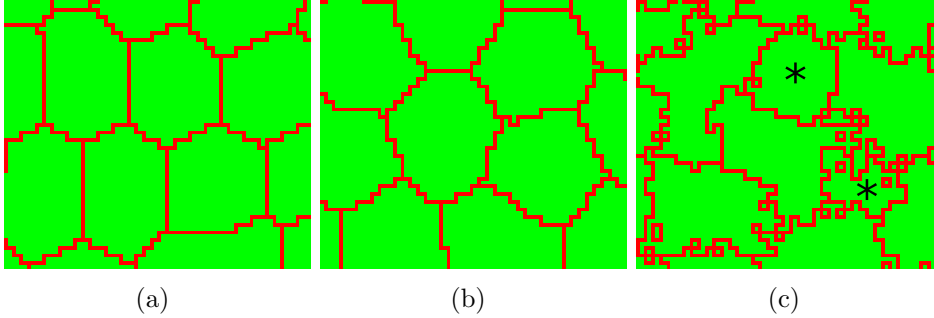


Figure 2.3: Calibration of the fluctuation allowance ξ . a) $\xi = 50$ b) $\xi = 400$ c) $\xi = 6400$; two parts of the same fragmented cell are marked by an asterisk.

neighbourhood (Figure 2.2a) is sufficient to calculate $\Delta\mathcal{E}_{i \rightarrow i'}$ (Eq. [2.3]):

$$\begin{aligned} \Delta\mathcal{E}_{i \rightarrow i'} &= \mathcal{E}_{\text{after}} - \mathcal{E}_{\text{before}} \\ &= \sum_j [(\delta_{i'j} - 1) \gamma_{i'j} - (\delta_{ij} - 1) \gamma_{ij}] \\ &\quad + 2[1 + \lambda_A (A_{i'} - A_{0i'} - A_i + A_{0i})]. \end{aligned} \quad (2.5)$$

The ‘variable tension model’, that will be introduced in Chapter 3, has a perimeter conservation term that can be treated locally as well. In Chapter 4 we will encounter an energy function using interface-specific perimeter moduli, which requires the bookkeeping of considerably more cell characteristics, and which is thus computationally less efficient.

The fluctuation allowance ξ has to be adjusted to avoid lattice anisotropy and prevent cells from falling apart. As shown in Figure 2.3a, at low values of ξ , lattice anisotropy is visible even if we use the fourth order neighbourhood. At high values of ξ (Figure 2.3c), numerous pieces of the cells are disconnected, but communicate with each other (i.e. they are all taken into account in the area of the cell, and thus cell mass can be displaced from one part to the other without physical connection), which is not realistic. Furthermore, it forbids to treat the simulated cells as ‘a space tiling pattern without gaps nor overlaps’ (Section 1.4), and basic equations like Eq. [1.8] can not be applied.

All input parameters related to the energy are arbitrarily scalable: γ_{ij} , λ_A (Eq. [2.2]) and ξ (Eq. [2.3]) can be multiplied by the same factor without affecting the results; the ratios ξ/γ and ξ/λ_A thus determine the amount of fluctuations. Adding extra terms to the energy function adds parameters that co-determine the amount of fluctuations: in Eq. [3.2], these are λ_P and P_0/A_0 . Adjusting ξ as a function of two to four other parameters is

thus not always easy, and is done by ‘eyeballing’ throughout this thesis. In the acceptable range of values of ξ , low values yield a higher precision of the cell shape, and are thus used in Chapter 3, while high values allow energy minimisation to go faster (less MCS), which is used in Chapter 4. The effect of ξ is studied further in Chapter 5.

2.3 Quantitative use

2.3.1 Measurements

The CPM yields output that has to be compared to the available experimental data. In Chapter 3 and 4 the output is mostly graphical, and the goal is a qualitative comparison with the experiments (‘eyeballing’), except for the contact angles between cells. In Chapter 5 we quantitatively compare several measures of the mechanical behaviour of a simulated aggregate.

We here introduce the main measurements, to which in Chapter 5 some more measurements are added.

Area In a 2D lattice, the area of an object is obtained by counting the number of pixels it occupies; each pixel belongs to one object.

Length of interfaces and perimeters As discussed in Section 2.2.1, the measurement of the length of an interface suffers from lattice anisotropy, which is reduced to less than 3% by using interactions up to the fourth order neighbourhood. This value thereby is an estimate for the precision of the determination of the length of an interface.

An interface’s length is determined, up to a prefactor, by counting the number of pixels that interact across it. The prefactor was estimated to be 10.6 in CPM simulations of bubbles by Raufaste (2007), which is the value used in Chapter 3. For Chapter 5, we determine it by comparing the area and measured perimeter P of circles drawn on a lattice, and find a value of 11.3.

In the energy functions, we use the neighbour count as a value for the perimeter. If we want to express it in units comparable to the area, we have thus to divide the neighbour count by 11.3. In Chapter 3 and 4, the modelling is qualitative, and the prefactors are not important; parameter values are thus given uncorrected. In Chapter 5, when quantitative comparisons are important, they are always corrected.

2. THE CELLULAR POTTS MODEL (CPM)

Angles Where three interfaces meet, the contact angles are measured by fitting straight lines through these interfaces, starting from the meeting point. Due to lattice anisotropy, the number of orientations that a short line can have is limited; for a line of one pixel (where the length here, exceptionally, is measured as the number of first order neighbour interactions across that line), only two orientations (0° and 90°) are possible; for a length of two pixels, four orientations, etc. The fitted lines should not be too long, as the curvature (if any) of the interface would bias the measured angle. When the interface that meet are long enough (> 100 pixels), lines fitted through 10 to 15 interacting pixels closest to the meeting point are used.

Energy The total energy of a simulated pattern is found by evaluating the energy function. For one cell i , the energy corresponding to Eq. [2.2] is

$$\mathcal{E}_i = \sum_{\text{neighbour cells } j} P_{ij} \gamma_{ij} + \lambda_A (A_i - A_{0i})^2 . \quad (2.6)$$

Pressure In 2D simulations, the pressure of a cell is the derivative of its energy to its area, without changing its perimeter:

$$\Pi_i = -\frac{\partial \mathcal{E}_i}{\partial A_i} = -2\lambda_A (A_i - A_{0i}) . \quad (2.7)$$

Interfacial tension An interface between cells i and j has an energy

$$\mathcal{E}_{ij} = P_{ij} \gamma_{ij} .$$

The interfacial tension is its derivative to the interface length

$$\frac{\partial \mathcal{E}_{ij}}{\partial P_{ij}} = \gamma_{ij} . \quad (2.8)$$

Here again, γ should be corrected with the prefactor for lengths when making quantitative comparisons; in Chapter 5, all given values are corrected.

2.3.2 Length and time scales

The minimal size of a simulated object is one pixel, which is also the minimal size of a fluctuation (one copy event). Objects with the size of one pixel thus have a high probability to disappear. This holds for interfaces as well; when the contact between cells is one pixel long, a neighbour change (cf

Figure 1.11) easily occurs. Raufaste et al., 2007 used the discreteness of the CPM at their advantage in simulations of foams: they found that the size of the bubbles compared to the pixel size enables them to simulate the critical distance between bubbles for a rearrangement to occur, a distance attributed to the liquid/gas ratio in real foams.

The CPM finds a minimum energy configuration of a pattern; its energy minimising algorithm is however not useful to study the dynamics of the relaxation to an energy minimum. It is possible to study the shape changes or movements of the simulated objects if these changes are slow enough: the shape stays at an energy minimum while changing, and the dynamics are thus a succession of equilibria. Jiang et al. (1999); Raufaste et al. (2007) thus simulate foam shearing and flow, and Savill and Hogeweg (1997); Marée et al. (1999a); Marée and Hogeweg (2001) simulate the dynamics of morphogenesis in *Dictyostelium*. The time scale for such studies should be chosen with care, as the simulated objects can move with a maximal speed around 1 pixel per MCS.

2.4 Implementation, use and resources

The code for computer simulations is based on the ‘extended CASH libraries’ (excalib) written by A. Marée (Theoretical Biology and Bioinformatics, Utrecht University, the Netherlands). CASH is a collection of libraries for ‘Cellular Automata in Simulated Hardware’, written by R. de Boer and A. Staritsky (Theoretical Biology and Bioinformatics, Utrecht University, the Netherlands). CASH is freely available.*

Both excalib and CASH are written in the C programming language, and work on UNIX systems with X11 display graphics and graphical output in the Portable Network Graphics (png) format.

Excalib’s algorithms include the implementation of Eq. [2.2], Metropolis algorithm, Monte Carlo sampling, which have been optimised for simulation speed on a single processor. New code for the simulations presented here is either based on excalib functions (as is the case for the measurements of cell shape changes and rearrangements, Section 5.2.5) or written from scratch (e.g. force and aggregate shape measurements, Section 5.2.1 and Section 5.2.2).

A new code that uses more low-level functions is developed, based on CASH, to study either single cells on micro-patterned substrates (Vianay, Guillou, in prep.) or anisotropic cell shapes in tissues (collaboration with Y. Bellaïche).

*<http://www-binf.bio.uu.nl/rdb/software>

Simulations are either run on a desktop computer with two 3.2 GHz processors, or on the clusters available at the Laboratoire de Spectrométrie Physique.[†]

2.5 Résumé français

Le Modèle de Potts Cellulaire (*CPM* en anglais) est une méthode de simulation qui a ses bases dans la physique (mousses, transitions de phase), et qui a premièrement été utilisée en biologie pour étudier le tri cellulaire. Aujourd'hui, le CPM intervient dans de nombreuses études des problèmes biologiques, variant de la croissance des tumeurs à la morphogenèse. Le CPM permet de décrire la forme des membranes et ses fluctuations, et est relativement rapide comparé aux autres méthodes.

Dans le CPM, une cellule est un ensemble de pixels sur un réseau. Dans cette thèse, nous utilisons uniquement des réseaux carrés en deux dimensions. Dans la forme la plus simple, l'énergie des cellules est une énergie d'interaction associée aux interfaces, et une conservation de l'aire. L'algorithme tire des pixels au hasard, et essaie de changer l'état d'un pixel par l'état d'un des voisins. Si l'énergie totale est diminuée, le changement est toujours accepté, sinon le changement peut être accepté avec une probabilité qui décroît avec l'augmentation de l'énergie.

Le CPM ne peut pas décrire la dynamique de la relaxation vers un minimum d'énergie, mais peut être utilisé pour décrire l'évolution d'un système, si elle est suffisamment lente : la dynamique, dans ce cas, est quasi-statique.

Pour comparer les résultats des simulations avec les expériences, nous utilisons premièrement la sortie graphique, où la comparaison se fait à l'oeil. Deuxièmement, nous utilisons des mesures quantitatives de forme (l'aire et le périmètre des cellules et les angles de contact), et des quantités physiques qui peuvent être déduites de l'énergie (notamment la pression et la tension de l'interface). D'autres mesures sont décrits dans les chapitres de résultats.

[†]<http://browalle.ujf-grenoble.fr:8080/Cluster>

Cell topology and geometry in *Drosophila* eye facets

3.1 Introduction

Epithelial cells can bear striking resemblances with soap bubbles or foams, as has been pointed out by Thompson (1942), and by several others since then. Recently, Hayashi and Carthew (2004) compared the packing and shape of the so-called cone cells in *Drosophila* retina facets (Figure 3.1) to those of soap bubbles (Figure 3.2). They also showed that the cell shape depends on cadherin expression. Both observations led them to conclude that “surface mechanics mediate pattern formation”.

We will show in this chapter that the cell’s surface mechanics, however, is not overall surface minimisation as in bubbles. We propose an other energy function: minimising the energy according to this function allows us to describe cell shape and packing in each facet, for the wild type and a range of mutants.

In the compound eye of *Drosophila*, the basic unit, the ommatidium, is repeated approximately 800 times. All ommatidia have the same cell packing, which is essential for correct vision. One ommatidium consists of four cone cells and two primary pigmented cells, surrounded by six secondary and three tertiary pigment cells and three bristle cells (Figure 3.1). The cone cells can be subdivided into a polar, equatorial, anterior and posterior cone cell, according to their position. The events of cell differentiation, movements, shape changes, and death leading to this configuration are described by Wolff and Ready (1993); Cagan and Ready (1989).

This chapter is based on published work: Käfer, Hayashi, Marée, Carthew and Graner, Proc. Natl. Acad. Sci. U.S.A., vol. 104, no. 47, pp. 18549-18554, 2007. Between the publication of this paper and the writing of this thesis, several related papers appeared. These are discussed in Section 6.3

3. CELL SHAPE IN THE DROSOPHILA RETINA

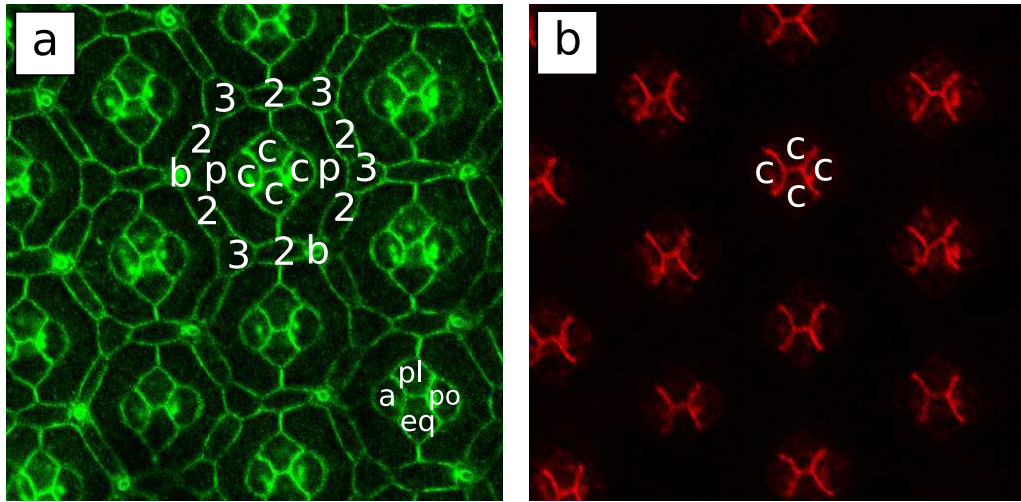


*Figure 3.1: Confocal microscopy images of the Drosophila retina. The pictures measure $100 \times 100 \mu\text{m}^2$. a) β -catenin, a component of the adherens junction, is stained green. Nearly all catenin fluorescence between the cone cells is seen in a $1.26 \mu\text{m}$ thick layer. Indicated are the cone cells (c), primary pigmented cells (p), secondary (2) and tertiary (3) pigment cells, and bristle cells (b). In this particular ommatidium, one bristle cell is replaced by a tertiary pigment cell. Cone cells are the polar (pl), equatorial (eq), anterior (a) and posterior (po) ones. b) N-cadherin fluorescence in the same plane of focus. N-cadherin is restricted to the cone - cone interfaces. Reprinted by permission of the National Academy of Sciences: *Proc. Natl. Acad. Sci.* 104(47), 18549-18554, copyright 2007.*

Hayashi and Carthew (2004) showed that cadherin expression influences ommatidial cone cell packing. Two cadherin types, E- and N-cadherin, are expressed in different cells: all interfaces bear E-cadherin, while N-cadherin is present only at interfaces between the four cone cells (Figure 3.1). Cadherin-containing adherens junctions form a zone close to the apical cell surface, allowing the retina epithelium to be treated as a 2D tissue. In the wildtype and in *Roi*-mutant ommatidia with two to six cone cells, these cone cells assume a packing (or topology, that is, relative positions of cells) strikingly similar to that of a soap bubble cluster (Figure 3.2). When cadherin expression is changed in a few or all of the cells, the topology sometimes changes, and in almost all cadherin mutants, the geometry (individual cell shapes, contact angles at the vertices, interface lengths) is different from the wildtype.

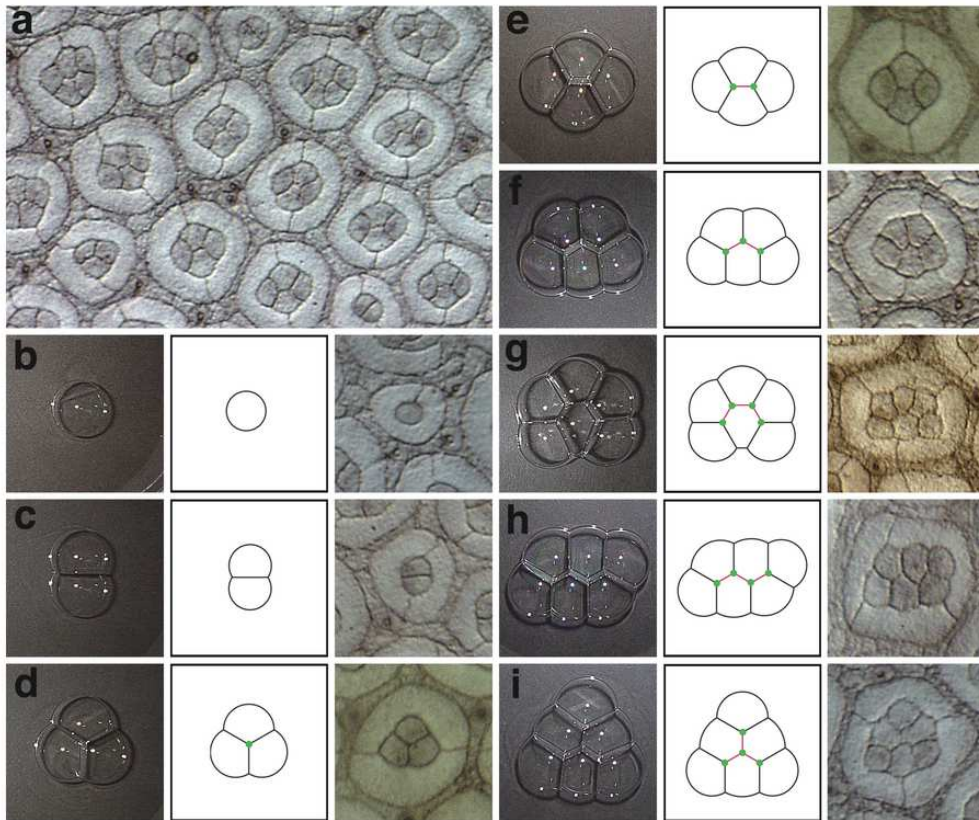


Figure 3.2: Comparison of ommatidia of Roi-mutants containing various numbers of cone cells, from Hayashi and Carthew (2004). Reprinted by permission from Macmillan Publishers Ltd: *Nature* 431, 647-652, copyright 2004.

It has been proposed that cells minimise their surface, like soap bubbles (Thompson, 1942; Chichilnisky, 1986; Hayashi and Carthew, 2004). To simulate this, we use the classical energy function of the CPM, Eq. [2.2]. Here, the only biological ingredient is differential adhesion: an interface between two cells has a *constant tension*, that is lower when the adhesion is stronger (Chichilnisky, 1986; Graner and Glazier, 1992; Glazier and Graner, 1993).

Cells, however, differ greatly from bubbles, both in their membrane and internal composition. Surface tension has been shown to be determined up to a large extent by the cortical cytoskeleton (Sheetz and Dai, 1996; Raucher and Sheetz, 1999; Dai and Sheetz, 1999; Morris and Homann, 2001). Adhesive cells have a tendency to increase their contact interfaces (Thoumine et al., 1999), not to minimise them. Tension generated by the cortical cy-

toskeleton is thus diminished by adhesion. These are the ingredients of a second model (Graner and Sawada, 1993; Ouchi et al., 2003), which we call *variable tension model*.

We test both models, using our knowledge from the experiments, and require that mutants are modelled by only changing existing parameters. This yields the following assumptions and requirements:

1. The adhesion strength is determined by the presence of the cadherins: when the two of them are present (i.e. at interfaces between cone cells), adhesion is thus stronger.
2. To model *Roi*-mutants, we should only need to change the number of cone cells
3. To model the cadherin mutant ommatidia, only the adhesion for the mutant cells should be changed (i.e. diminished for deletion, increased for overexpression)
4. All cells of a cell type that share the same mutation should be modelled using the same parameter values.

3.2 Methods

3.2.1 Experiments

Most experiments were conducted by Takashi Hayashi (Department of Biochemistry, Molecular Biology and Cell Biology, Northwestern University, Evanston, USA, and Department of Biophysics and Biochemistry, Graduate School of Science, University of Tokyo, Japan). Experimental procedures are described in Hayashi and Carthew (2004) and Hayashi et al. (1998).

In short, pupae were dissected between 38 and 40 hours after pupal formation (AFP) at 25°C (which corresponds to 35% of pupal life), to separate the eye discs from the rest of the pupa. The discs were stained with fluorescently labelled antibodies against DE-cadherin, DN-cadherin (referred to as E- and N-cadherin, respectively, in the rest of the text), β -catenin, or β -spectrin for confocal microscopy. Rough-eye (*Roi*) flies were used to examine the topology and geometry of variable number of cone cells.

The effect of eliminating or overexpressing cadherin molecules was studied in mosaic retinas composed of wild-type and mutant cells generated by the FLP-out method. More than five retinas were examined in each experiment. Thus, at least several hundred ommatidia (500) were examined for

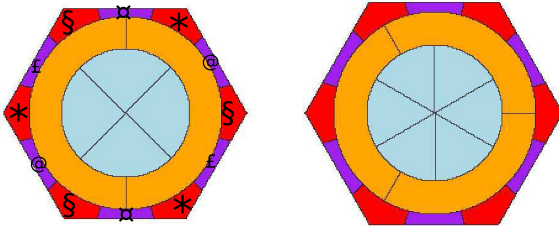


*Figure 3.3: Initial conditions of each simulation with four cone cells and two primary pigment cells (left), and six cone cells and three primary pigment cells (right). Periodic boundary conditions imply that the secondary pigment cells (purple) and tertiary pigment cells (red) that are marked with the same symbol, are treated as parts of the same cell. Reprinted by permission of the National Academy of Sciences: *Proc. Natl. Acad. Sci.* 104(47), 18549-18554, copyright 2007.*

the wild type and each mutation, except E- and N-cadherin overexpression, in which cases 100 ommatidia were examined.

3.2.2 Simulations

We model single ommatidia, using a hexagonally shaped field, with sides of approximately 100 pixels (the surface of the hexagon is 25160 pixels), and periodic boundary conditions, as if we were simulating an infinite retina with identical ommatidia. Simulations start from unstable initial conditions (Figure 3.3) designed to favour the random search of final, stable topologies. They can be started with different seeds of the random number generator, to explore whether multiple solutions are possible. We do not expect to find a quantitative correspondence between the frequency of topologies in simulations and experiments. We regard only the final result of the model simulations: we have found a local equilibrium, when the simulated shape does not change anymore. Initially, three to six cone cells meet in the center, in a n -fold vertex ($3 \leq n \leq 6$). We regard bristle cells as tertiary pigment cells, because they can substitute one another (Figure 3.1a) without visible influence on the other cells.

When the simulation starts, quickly the n -fold vertex disappears (if $n \geq 4$) and eventually, constraints are balanced. On a 3.2 GHz processor of a PC, it takes four to twenty seconds (corresponding approximately to 600 to 4000 MCS) to attain a shape that does not evolve anymore. We test

if topological changes occur by running the simulation longer (up to a few minutes).

In reality, interstitial fluid can enter from above or below the plane of interest, which we need to model to see whether cells lose contact or not. Since the model is in 2D and the algorithm normally does not allow nucleation at distant sites, at each MCS we randomly choose one pixel at a cell interface and change its state into ‘intercellular space’, a state without area and perimeter constraints and no adhesion. These simulations typically take longer times (more MCS) to run.

We compare this shape with the experimental results (topology, geometry). Distinguishing between topologies is trivial. But, due to the variability of membrane fluctuations, we find that it is difficult to describe the geometrical characteristics (e.g. contact angles for the mutant ommatidia, interface lengths, elongation of cells) by quantitative measurements: one obtains more information by looking at the image (‘eyeballing’). Quantitative measurements serve as a complement to eyeballing when enough data are available (cf Figure 3.6), not as replacement. Since the relation between cell shapes and the ingredients of the models is a complex one, we search for optimal parameters by trying and adjusting. We determine for each model which parameters do influence the shape of the cone cells; for the other parameters, we choose reasonable values (e.g., a compromise between simulation speed and precision, cf Marée et al. (2007)).

3.2.3 Image analysis

In experimental pictures by Hayashi et al. (1998), we measured contact angles in 22 wildtype ommatidia by hand, aided by the program ImageJ (Rasband, 2005). Ommatidia have two axes of symmetry, and we considered the ommatidia to consist of four equal quarters, which gave us 88 measurements for each angle (and 44 measurements of the angles that are intersected by the axes of symmetry).

In simulations, we measured the contact angles of straight lines fitted through the interfaces that meet in the vertex. The line should be long enough to avoid grid effects; we fitted a straight line using the first 15 first-order neighbouring sites. Since the simulated cells show random fluctuations, statistics were obtained by measuring the contact angles several times during the simulation, or in simulations with different random number seeds.

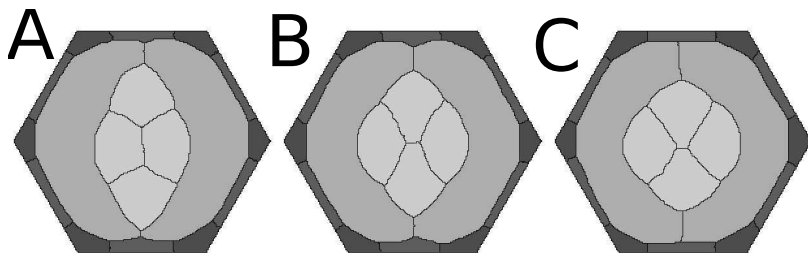


Figure 3.4: Constant tension model simulations. **A:** $\gamma_{CC} = 40$, $\gamma_{CP} = \gamma_{PP} = 80$. **B:** Same as (A), but with lower tension (stronger adhesion) between the polar and equatorial cone cell, $\gamma_{polar, equatorial} = 20$. **C:** Same as (A), but with lower tension (stronger adhesion) between the primary pigment cells: $\gamma_{PP} = 40$. Reprinted by permission of the National Academy of Sciences: *Proc. Natl. Acad. Sci.* 104(47), 18549-18554, copyright 2007.

3.3 Modelling cells as soap bubbles

The simplest model to try is a soap-bubble like model, based on surface minimisation, as suggested by the resemblance in Figure 3.2. In this ‘classical’ energy function of the CPM (Eq. [2.2]), a stronger adhesion between cells i and j is represented by a lower interfacial tension (Chichilnisky, 1986; Graner, 1993; Graner and Glazier, 1992; Glazier and Graner, 1993). This tension γ_{ij} (≥ 0), is constant, and depends only on the cell types of i and j . We name this model the ‘constant tension model’.

We are using a 2D model, and repeat Eq. [2.2]:

$$\mathcal{E} = \sum_{\text{interfaces}} \gamma_{ij} P_{ij} + \lambda_A \sum_{\text{cells}} (A_i - A_{0i})^2 . \quad (3.1)$$

P_{ij} is the length of the interface between cells i and j , A_i is the cell’s area (the 2D equivalent of volume), A_{0i} is the cell’s preferred area (target area), and λ_A is the area modulus (a lower value allows more deviations from A_0). The values of A_{0i} are adjusted by eye to the areas observed in the experimental pictures, with cone (C) cells being smaller than primary pigment (P) cells.

We assume C - C adhesion γ_{CC} , mediated by both E- and N-cadherin, to be stronger than C - P and P - P adhesion, γ_{CP} and γ_{PP} , which are mediated by E-cadherin alone. We assume the latter two to be equal: $\gamma_{CC} < \gamma_{CP} = \gamma_{PP}$. Only three parameters need to be explored extensively: γ_{CC} , γ_{CP} ($= \gamma_{PP}$), and λ_A . The tensions γ influence the cell shapes directly, whereas λ_A determines a cell’s deviations from the target area.

3. CELL SHAPE IN THE DROSOPHILA RETINA

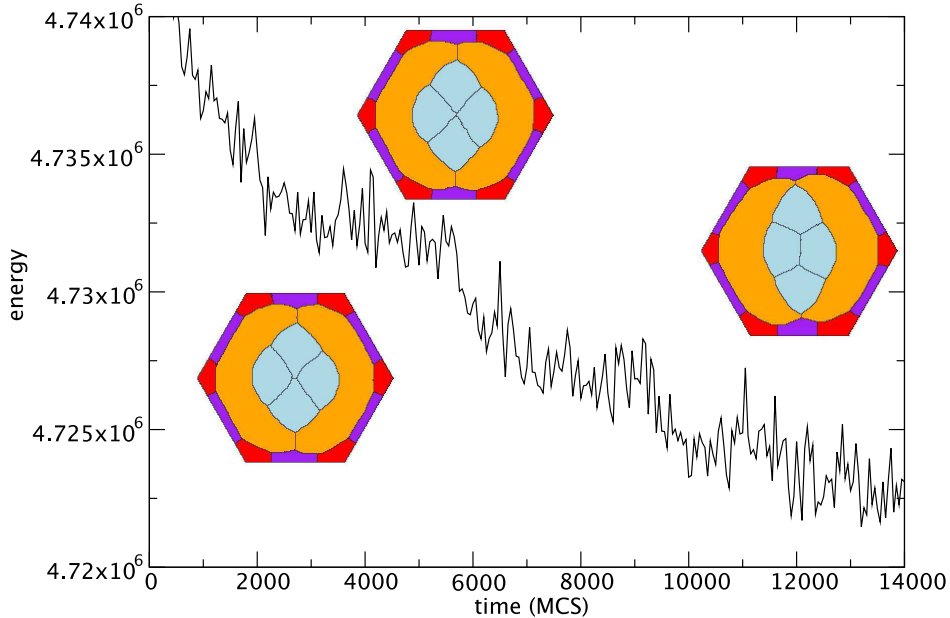


Figure 3.5: The total energy \mathcal{E} in the constant tension model (Eq. [3.1]) during a simulation that is forced to start with a contact between the polar and equatorial C cells. Insets show simulation snapshots.

Starting the simulations with a four-cell vertex (Figure 3.3A), we systematically find an incorrect topology (Figure 3.4A): the anterior and posterior C cell touch. Even if we force the correct one, where the polar and equatorial C cell touch, it is unstable and decays into the incorrect one: the interfaces between the P cells are under tension, and pull the polar and equatorial C cells apart. Figure 3.5 shows an example of a simulation with a forced contact between the polar and equatorial C cells: as the simulation progresses and the neighbours are changed, the energy keeps decreasing, showing that there is only one equilibrium configuration.

To obtain the correct topology, we need another assumption: either that the adhesion between polar and equatorial C cells is stronger (Figure 3.4B); or that the P cells pull less on them (by having a stronger adhesion, Figure 3.4C). Still, the geometry is quite different from the experiments: notably the interface between the polar and equatorial C cell is too short

in simulations. Besides, there is no experimental evidence to support these assumptions.

Another optimisation strategy is to determine (up to a prefactor) the tensions of three interfaces that meet in a vertex from the experimentally observed contact angles by using Eq. [1.6]. We inject those tensions in the model. By construction we obtain the correct contact angles, and thus topology; but the overall geometry (especially the interface lengths) differs considerably from observations (results not shown).

For the mutant ommatidia, the requirements (2) to (4) (page 56) could not be satisfied with this model: there are too many cases where other parameters need to be changed as well. We conclude that this model is insufficient to coherently describe the experiments.

To obtain the observed shapes, it would certainly be possible to choose a tension for each individual interface. But if the tension was just an input parameter without biological basis, then the model would not be predictive, nor help to understand the differences between the cells.

3.4 Adhesion and the contractile cytoskeleton

3.4.1 Variable tension model

Adhesion between two cells tends to extend their contact length; it thus contributes negatively to the energy, $-J_{ij}P_{ij}$, where $J > 0$: in agreement with intuition, a higher J describes a stronger adhesion, while $J = 0$ in absence of adhesion (Graner and Sawada, 1993; Ouchi et al., 2003). This extension is compensated by an elastic cell cortex term, $\lambda_P (P_i - P_{0i})^2$, where λ_P is the perimeter modulus, and P_{0i} is the target perimeter of cell i . The cell perimeter is the sum of its interfaces, $P_i = \sum_j P_{ij}$. We thus minimise the energy:

$$\mathcal{E} = - \sum_{\text{interfaces}} J_{ij}P_{ij} + \sum_{\text{cells}} [\lambda_P (P_i - P_{0i})^2 + \lambda_A (A_i - A_{0i})^2] . \quad (3.2)$$

The interfacial tension $\gamma_{ij} = \partial\mathcal{E}_{ij}/\partial P_{ij}$ (cf Eq. [2.8]) between cells i and j is the energy change associated with a change in membrane length; Eq. [3.2] yields:

$$\gamma_{ij} = -J_{ij} + 2\lambda_P (P_i - P_{0i}) + 2\lambda_P (P_j - P_{0j}) . \quad (3.3)$$

As in the previous model, γ_{ij} is positive, else the cell would be unstable. However, it is no longer an input parameter. A stronger adhesion (high J)

decreases the tension: this will usually cause an extension of the perimeter, which increases this tension again.

We represent all adhesion terms as combinations of E- and N-cadherin mediated adhesion (J_E and J_N , respectively). In the wildtype, the adhesion between C cells is mediated by both cadherins, so $J_{CC} = J_E + J_N$; whereas all other interfaces only have E-cadherin, so $J_{PP} = J_{CP} = J_E$. Values of A_0 are estimated from pictures. The target perimeter P_0 (expressed in units of $2\sqrt{\pi A_0}$) should be larger for cells that deviate more from a circular shape, i.e. for the P cells.

We thus adjust 6 main parameters: J_E , J_N , P_{0C} , P_{0P} , λ_P , λ_A , which is too much to explore systematically. We adjust the parameters by hand, for wildtype and mutant configurations simultaneously, since the wildtype alone does not sufficiently constrain the parameter combinations.

Unless indicated, throughout this paper, and for all figures except Figure 3.4, we use Eq. [3.2] with the same set of parameters (Table 3.1) for wildtype and mutants.

3.4.2 Wildtype

Starting the simulations with a four-cell vertex (Figure 3.3A), the cells relax either into the correct topology where the polar and equatorial cells touch (Figure 3.6); or into the incorrect one where anterior and posterior cells touch (analogous to Figure 3.4A). Both topologies are stable, i.e. they are local energy minima: Figure 3.7 shows that they are separated by an unstable state with a four-cell vertex, that has a higher total energy than the two topologies with only three-cell vertices. Which one of the topologies is reached, depends on the developmental history, which is outside the scope of this chapter; however, once reached, either one of them is stable.

In the correct topology, the geometry of the simulated ommatidium resembles well the experimental pictures. More quantitatively, the contact angles measured in simulations and in experiments agree as well (Figure 3.6). In contrast to the constant tension model, we do not need additional assumptions.

We find that the adhesion of secondary and tertiary pigment cells should be much stronger than can be expected from E-cadherin alone ($J_{23} > J_E$, Table 3.1), otherwise they lose contact. Experimentally, deleting the E-cadherin of these cells does not induce any geometrical or topological change (Hayashi and Carthew, 2004). Both experiments and simulations thus suggest that secondary and tertiary pigment cells might have other adhesion molecules than E- and N-cadherin.

Table 3.1: Simulation parameters of the wildtype in the variable tension model. ¶: Free parameter adjusted to compare to wildtype observation. †: Parameters which value has little effect on the images. ‡: Parameter of no effect on the images, since cone cells almost never touch secondary or tertiary pigment cells. Target perimeters are expressed as a factor times the perimeter of a circle having the specific target area. E.g. a prefactor of 1 indicates that the target perimeter of the cell equals the perimeter if the cell is round and has an area equalling its target area. A cell with a prefactor > 1 (like the primary pigment cells) can deviate much from a round shape. Abbreviations: N , N-cadherin; E , E-cadherin; C , cone cell; P , primary pigment cell; 2, secondary pigment cell; 3, tertiary pigment cell.

Parameter	Symbol	Value	
E-cadherin mediated adhesion	J_E	150	¶
N-cadherin mediated adhesion	J_N	450	¶
C - C adhesion	J_{CC}	$J_N + J_E$	
C - P adhesion	J_{CP}	J_E	
P - P adhesion	J_{PP}	J_E	
P - 2, P - 3 adhesion	J_{P2}, J_{P3}	J_E	
2, 3 adhesion	J_{23}, J_{22}, J_{33}	800	†
C - 2, C - 3 adhesion	J_{C2}, J_{C3}	70	‡
Random fluctuation allowance	T	125	†
Area modulus	λ_A	0.75	¶
Perimeter modulus	λ_P	0.5	¶
Size of total hexagon	A_{hex}	25160	†
Sum of all target areas	$\sum_{cells} A_{0i}$	$0.95 A_{hex}$	
Target area of C	A_{0C}	$(\sum_{cells} A_{0i}) / 16$	
Target area of P	A_{0P}	$11 (\sum_{cells} A_{0i}) / 40$	
Target area of 2	A_{02}	$(\sum_{cells} A_{0i}) / 30$	
Target area of 3	A_{03}	$(\sum_{cells} A_{0i}) / 20$	
Target perimeter of C	P_{0C}	$0.75 \times 2\sqrt{\pi A_{0C}}$	¶
Target perimeter of P	P_{0P}	$1.5 \times 2\sqrt{\pi A_{0P}}$	¶
Target perimeter of 2,3	P_{02}, P_{03}	$1 \times 2\sqrt{\pi A_{02}}$	†

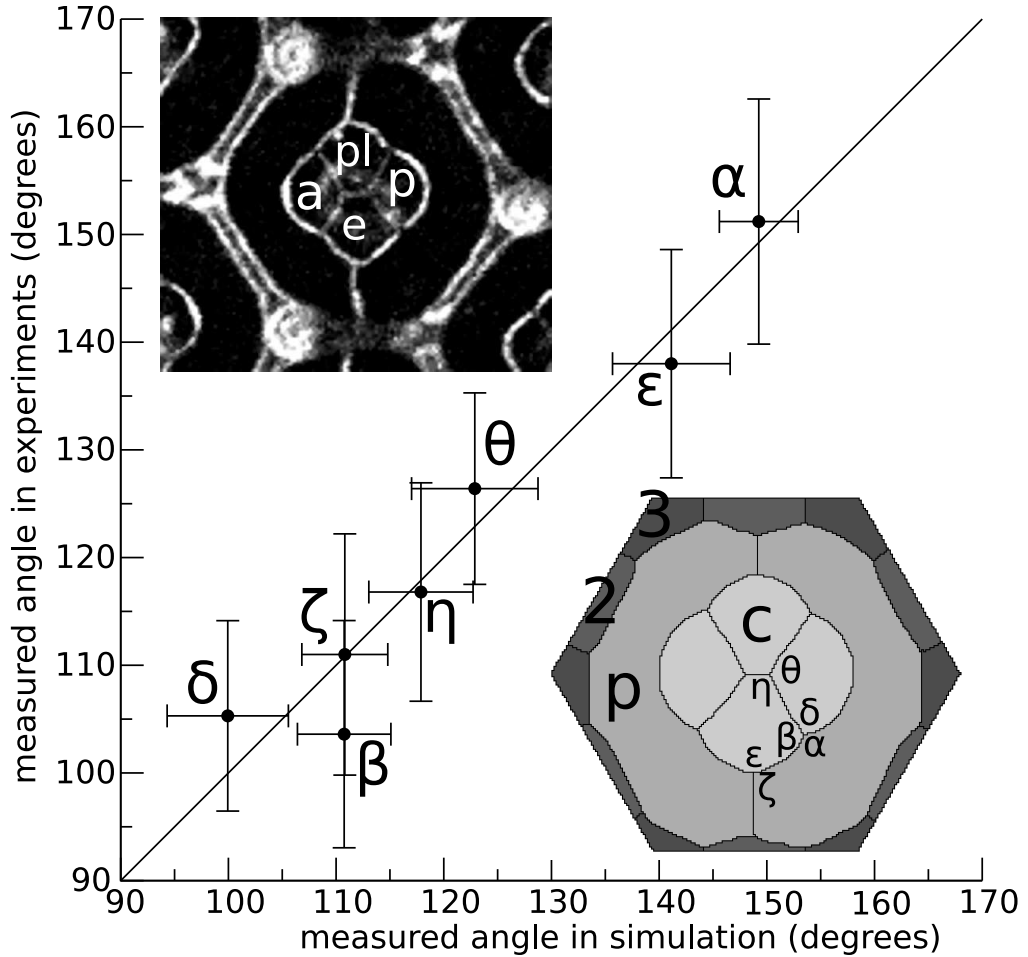


Figure 3.6: Wildtype. Contact angles measured in experiments and in simulations are plotted as average \pm statistical standard deviation; the straight line represents $y = x$. Inset left: an ommatidium stained for E-cadherin; anterior (a), posterior (p), polar (pl) and equatorial (e) cone cells. Inset right: variable tension model simulation, with cone cells (C), and primary (P), secondary (2) and tertiary (3) pigment cells. One ommatidium contains four times the angles α , β , δ , η , and ζ , and two times ϵ and θ .

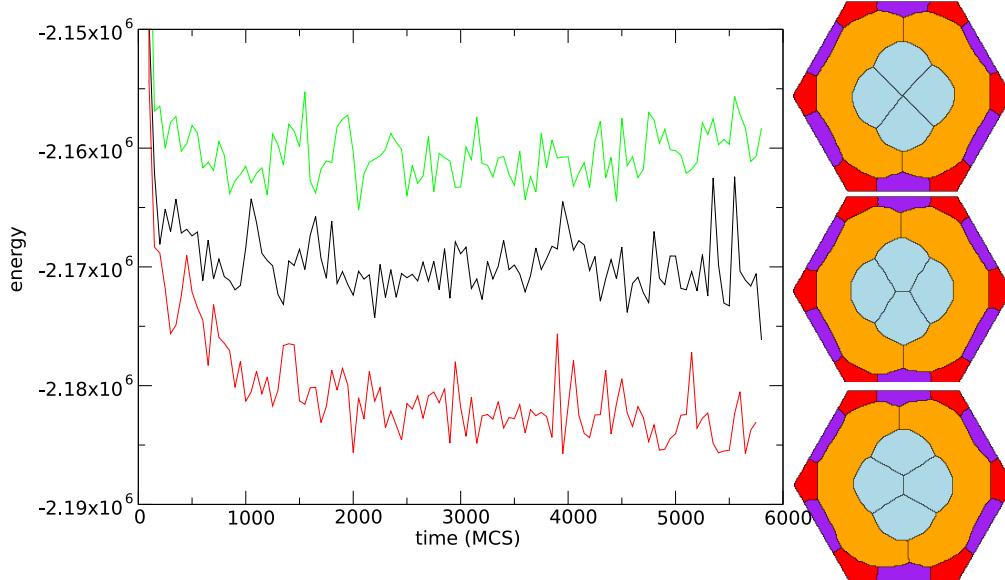


Figure 3.7: Comparison of the total energy \mathcal{E} in the variable tension model, Eq. [3.2]. The green line corresponds to the simulation with a fixed four-cell vertex (upper inset), the black line to the wildtype configuration (middle inset), and the red line to the topology where the anterior and posterior C cells touch (lower inset).

3.4.3 *Roi* mutants

Without any additional parameter, we simulate ommatidia with different numbers of C cells (*Roi*-mutants); the total size of the simulation lattice is adjusted accordingly. For one, two, three and five C cells, only one topology is observed in experiments, the same one as in simulations (Figure 3.8A-C and G-I).

For six C cells, three topologies are observed experimentally (Figure 3.8D-F). Theoretically, there are two more possible equilibrium topologies for 6-cell aggregates, which are never observed although one of them has a smaller total interface length (simulations using the Surface Evolver, S. Cox, unpublished results 2004). We have performed here a total of 42 CPM simulations with different random seeds (Section 3.2), and found only three topologies (Figure 3.8J-L): they correspond to the observed ones.

In contrast to the almost perfect arrangement of the ommatidia in a hexagonal pattern in wild-type flies, ommatidia of *Roi*-mutants do not all

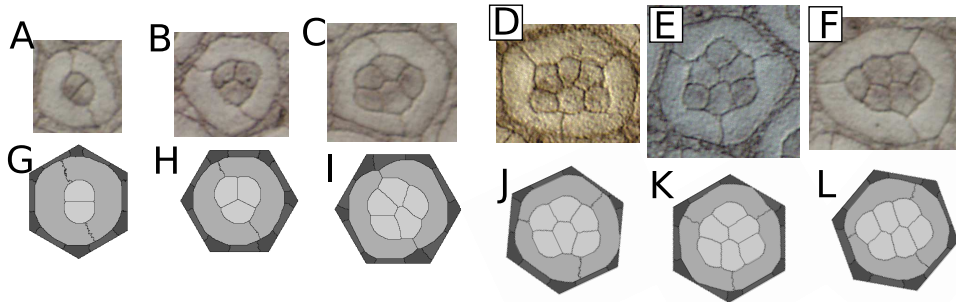


Figure 3.8: *Roi* mutants with 2, 3, 5 and 6 cone cells. **A-F**: Experimental pictures from Hayashi and Carthew (2004) [Reprinted by permission from Macmillan Publishers Ltd: *Nature* 431, 647-652, copyright 2004]. **G-L**: Corresponding simulations, reprinted by permission of the National Academy of Sciences: *Proc. Natl. Acad. Sci.* 104(47), 18549-18554, copyright 2007.

have six sides and are assembled into a disordered pattern (Quilliet et al., 2008). Thus, in *Roi*-mutants, ommatidia have variable shapes, which origin is not easily understood. Since in turn the shape of the ommatidium influences the geometry of its *C* cells, studying the geometry of the *C* cells in more detail would only be possible by adding more free parameters.

3.4.4 N-cadherin mutants

Again without any additional parameter, simply by suppressing J_N , we predict the pattern of ommatidia with N-cadherin deficient *C* cells. Since N-cadherin is only present on interfaces between *C* cells, deletion means we set the adhesion between mutant and wildtype *C* cells as $J_{cC} = J_{cc} = J_E$ (mutant cells are denoted by lower case letters).

We predict the correct topologies (Figure 3.9A-F and I-N), most of which are the same as in the wildtype. We predict qualitatively the main geometrical differences between mutants and wildtype: (i) the length of the interfaces between mutant cells and wildtype *C* cells decreases; (ii) the contact angles change; (iii) the interface length between the remaining wildtype *C* cells increases (Figure 3.9A-B and I-J); and (iv) the length of the central interface increases (Figure 3.9D and L).

When the polar or equatorial cell is the only *C* cell without N-cadherin, we simulate (Figure 3.9M-N) both topologies that coexist in experiments (Figure 3.9E-F).

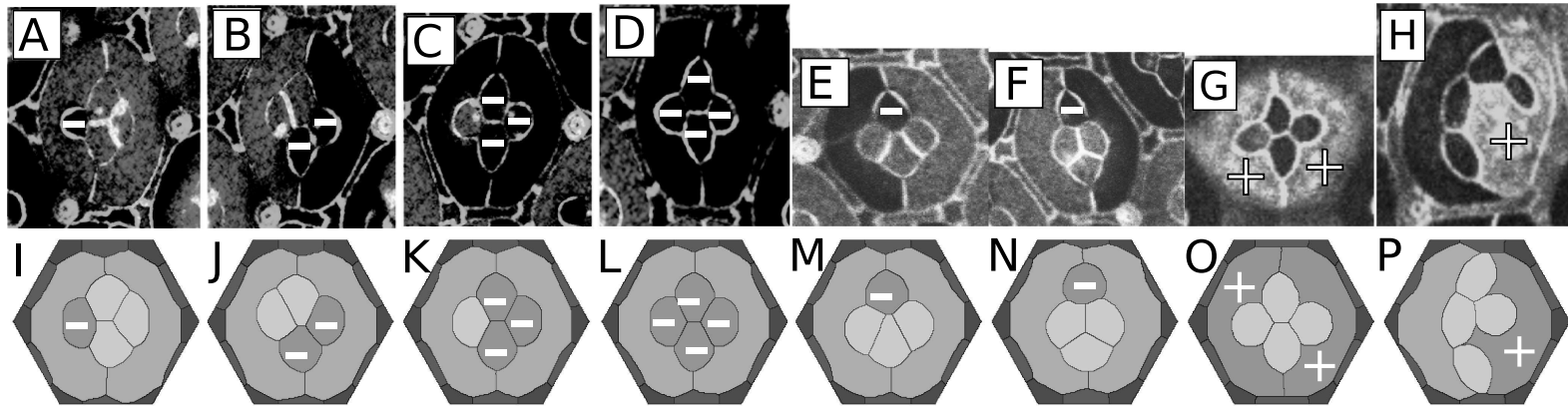


Figure 3.9: *N*-cadherin mutants. Mutant cells are indicated with a "+" for overexpression, "-" for deletion. **A-H**: Experimental pictures. **I-P**: Corresponding simulations. A-D reprinted by permission from Macmillan Publishers Ltd: *Nature* 431, 647-652, copyright 2004, other images reprinted by permission of the National Academy of Sciences: *Proc. Natl. Acad. Sci.* 104(47), 18549-18554, copyright 2007.

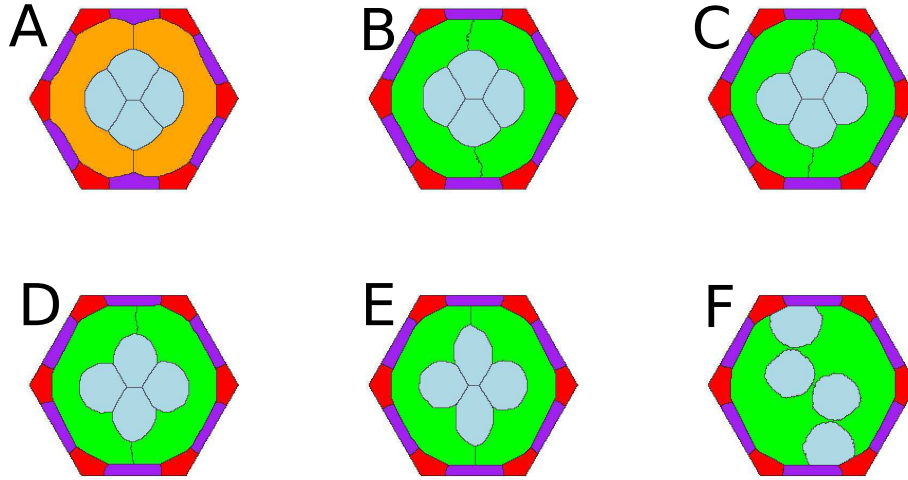


Figure 3.10: Determination of the adhesion between cone cells and two N-cadherin mis-expressing pigment cells. Simulations are shown with values $J_{Cp} = 150$ (A), 600 (B), 700 (C), 750 (D), 800 (E), 850 (F). (A) corresponds to wildtype, (D) corresponds best to the mis-expression experiment (Figure 3.9G). Reprinted by permission of the National Academy of Sciences: *Proc. Natl. Acad. Sci.* 104(47), 18549-18554, copyright 2007.

To simulate one mutant P cell that mis-expresses N-cadherin, we optimise J_{Cp} . While for the wildtype $J_{CP} = J_E = 150$, we find an increase for the mutant, $J_{Cp} = 150 + 600$. The high adhesion of this P cell with the C cells severely disrupts the normal configuration. Many topologies that differ considerably from the wildtype are observed in experiments and simulations (e.g. Figure 3.9H,P). When both P cells mis-express N-cadherin, they balance each other and the topology (but not the geometry) is back to normal (Figure 3.9G). Optimisation yields $J_{pp} = 150 + 700$ (Figure 3.9O and Figure 3.10). Both J_{Cp} and J_{pp} are higher than the wildtype value of C - C adhesion ($J_{CC} = J_E + J_N = 150 + 450$).

3.4.5 E-cadherin mutants

The mutant C cell in Figure 3.11A does not express E-cadherin, and it lacks adherens junctions at the interfaces with the P cells (Hayashi and Carthew, 2004). To simulate it, it would seem natural to suppress J_E at all interfaces, that is, $J_{cP} = 0$ and $J_{cC} = J_N$. With this assumption, we

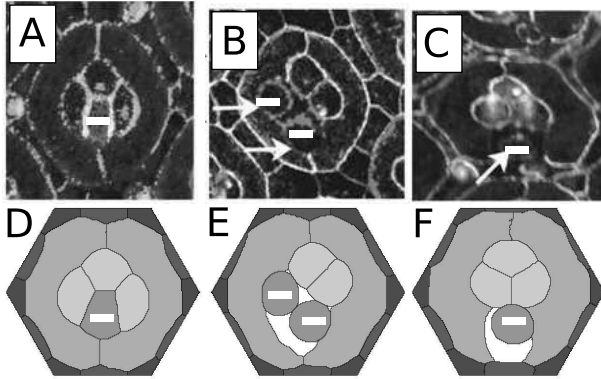


Figure 3.11: Loss of adhesion. Mutant cells are indicated with a “-”. **A:** A mutant cone cell lacking *E-cadherin*. **B-C:** Double mutant cone cells for *E-cadherin* and *N-cadherin*. **D-F:** Corresponding simulations. A-C reprinted by permission from Macmillan Publishers Ltd: *Nature* 431, 647-652, copyright 2004; D-F reprinted by permission of the National Academy of Sciences: *Proc. Natl. Acad. Sci.* 104(47), 18549-18554, copyright 2007.

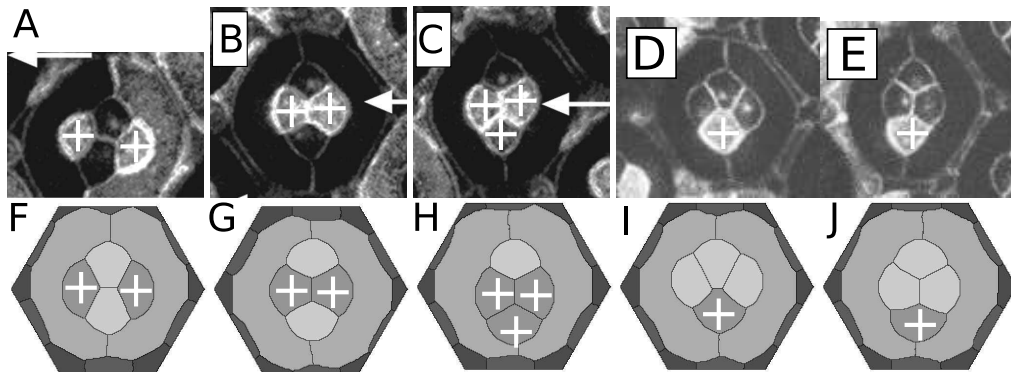


Figure 3.12: *E-cadherin* overexpression. Mutant cells are indicated with a “+”. **A-E:** Experimental pictures, **F-J:** Corresponding simulations. A-C reprinted by permission from Macmillan Publishers Ltd: *Nature* 431, 647-652, copyright 2004, other images reprinted by permission of the National Academy of Sciences: *Proc. Natl. Acad. Sci.* 104(47), 18549-18554, copyright 2007.

obtain the correct topology, which is the same as in the wildtype; however, the simulated geometry (not shown) is also the same as the wildtype, while the experiment is significantly different (Figure 3.11A). If we rather assume that C - C adhesion is unchanged by this mutation ($J_{cC} = J_{CC}$), we obtain a good agreement (Figure 3.11D).

E-cadherin overexpression in C cells (but not in P cells) significantly affects the pattern, yielding a coexistence of different topologies: in Figure 3.12A and B, the same cells are mutants, but the topologies differ; the same holds for Figure 3.12 D and E. We predict the observed topologies (all stable) and, qualitatively, the geometries (Figure 3.12F-J) when we increase the C - P cell adhesion from $J_{CP} = J_E = 150$ to $J_{cP} = 300$; while we find that the adhesion between a wildtype and mutant C cells should not change, $J_{cC} = J_{CC} = J_E + J_N$, we should change it if both are mutants, $J_{cc} = 350 + J_N$. Since E-cadherin overexpression in P cells rarely induces geometrical or topological changes (Hayashi and Carthew, 2004), we do not change their adhesion values.

3.4.6 E- and N-cadherin mutants

We predict the effect of both E-cadherin and N-cadherin missing in C cells by setting $J_{cC} = J_{cP} = J_{cc} = 0$. Mutant C cells do not adhere to any of their neighbours, Figure 3.11E-F: intercellular space becomes visible between the cells, and the cells have shrunk. This agrees well with experiments, where mutant C cells lose the apical contacts with their neighbours (Figure 3.11B-C).

3.5 Discussion

3.5.1 Constant and variable tension models

When surface tension is a constant model parameter, only modified by adhesion, the surface mechanics are soap-bubble-like: minimisation of the interfaces with cell type dependent weights (Chichilnisky, 1986; Graner, 1993; Graner and Glazier, 1992; Glazier and Graner, 1993; Brodland and Chen, 2000). This model proves to be insufficient here. In a rarely cited paper, Stein and Gordon (1982) predicted surface tension variation between cell-cell interfaces by treating “epithelia as bubble rafts”. They concluded that with this approach, the predicted surface tension variation is large, and therefore a bubble-like description is not always correct.

However, in studies focusing on larger aggregates (10^2 to 10^4 cells) (Graner, 1993; Brodland and Chen, 2000; Käfer et al., 2006), constant surface tension was sufficient to explain tissue rounding and cell sorting, and even *Dictyostelium* morphogenesis (Marée and Hogeweg, 2001). This constant tension model catches two important features of tissues of adherent cells: first, cells tile the space without gaps or overlap; second, the interface between cells is under (positive) tension, which implies for instance that three-cell vertices are stable, unlike four-cell ones (Plateau, 1873; Weaire and Hutzler, 1999), and thus severely constrains the possible topologies (Weaire and Hutzler, 1999).

In the present example of retina development, we show that interfacial tension should be variable, as described in a second model (Graner and Sawada, 1993; Ouchi et al., 2003). Tension results from adhesion-driven extension of cell-cell interfaces, balanced by an even larger cortical tension (Eq. [3.3]). It explains correctly the topologies of many observations, and correctly simulates the geometries. It requires more free parameters; but they are tested against many more experimental data; and their origins, signs and variations are biologically relevant. In particular, it does not require to assume any difference between the cone cells (anterior, posterior, polar, equatorial, cf Figure 3.1 and 3.6).

In the variable tension model, adding more refinements (and thus more free parameters) would be easy, but does not seem necessary to describe the equilibrium shape of ommatidial *C* cells. The parameters should not be taken as quantitative predictions, since *in vivo* biophysical measurements to compare them to are lacking.

Why certain shapes are observed more often than others depends on the developmental history of the tissue, which is determined by e.g. the sequence of cell differentiation, and cell divisions and deaths. Since a lot is still unknown about the developmental history, we do not include it in the modelling. However, if cells are in mechanical equilibrium at any moment in development, future insights in developmental gene regulation could be translated in parameter changes that permit the modelling of the dynamics of development.

3.5.2 Adhesion

By adjusting a set of 6 independent free parameters in the variable tension model, we obtain topological and geometrical agreement between the simulations and the pictures of 16 different situations: the wildtype (Figure 3.6), the six topologies observed in the *Roi*-mutants (Figure 3.8); as well as

the nine cadherin deletion mutants (Figure 3.9A-F, Figure 3.11) by setting the corresponding parameter to zero.

We also simulate 7 cadherin overexpression mutants, by re-adjusting the corresponding parameter (Figure 3.9G,H, Figure 3.12): adhesion is increased. The strongest increases are found when two overexpressing cells touch: this corresponds to the idea that the adhesion strength depends on the availability of cadherin molecules in both adhering cells.

We find two cases where a mutation does not seem to change the adhesion strength: first, when deleting E-cadherin from one C cell, its adhesion with a normal C cell is unchanged (Figure 3.11D); second, we did not observe shape changes in E-cadherin overexpressing P cells in experiments (cf Hayashi and Carthew, 2004), and do not model them.

Indeed, while a linear relation between cadherin expression and adhesion strength has been found *in vitro* (Foty and Steinberg, 2005), this need not be true *in vivo*, since cells have many more ways to regulate protein levels. These exceptions, thus, do not contradict the conclusion that the shapes observed in mutants are the effect of altered adhesion: an increase in the case of overexpression, a decrease in the case of deletion.

3.5.3 Cortical tension

In the variable tension model, the perimeter modulus λ_P and the target perimeter P_0 reflect the role of the cortical cytoskeleton. The target perimeter is always smaller than the perimeter, therefore the interfacial tension γ_{ij} (Eq. [3.3]) is always positive, else the cell would be unstable and fall apart or disappear. The cortex of the simulated cells is contractile, and generates tension. This tension depends on the perimeter P of the cell, which length depends on the cell's shape, which in turn depends on the tension: there is a feedback between tension and shape, and thus between each cell and its neighbours.

To understand the effect of this feedback, let us consider the wildtype ommatidium. We assume that the four C cells have equal adhesion properties. The tension at the interfaces between the two P cells pulls at the polar and equatorial C cell. When the tension is constant, these cells will therefore be pulled apart (Figure 3.4A): the cells do not react on their deformation. When the tension, however, depends on the cell's perimeter, pulling at those cells deforms them, and increases their tension: energy minimisation thus requires that they stay in contact.

The prediction that cytoskeletal contractility is essential for the establishment of cell shape should be tested, e.g. by treating the cells with cytoskeletal inhibitors (Raucher and Sheetz, 1999; Bar-Ziv et al., 1999), or

genetically modifying the cytoskeleton. Since the cytoskeleton has multiple functions that could interfere with adhesion (cf Geisbrecht and Montell, 2002; Gumbiner, 2005), the results will be difficult to interpret. Preliminary experimental results (not shown) do indicate that genetically disturbing Rho-family GTPases influences the cell shape. The role of the cytoskeleton has been confirmed in various tissues and organisms (e.g. Schock and Perrimon, 2002; Bertet et al., 2004; Pilot et al., 2006). We here present a computational framework able to test this hypothesis, which can be extended to other tissues, ranging from patterns of few cells to large-scale aggregates.

3.6 Conclusions

Hayashi and Carthew (2004) compared the topology of the cone cells in the ommatidium to the topology of soap bubble clusters. Here, by taking the whole ommatidium into account, we confirm and refine the conclusion that surface mechanics are involved in the establishment of cell topology and geometry. These surface mechanics are more complicated than the overall surface minimisation that governs bubble shape, but 1) they are still surface mechanics, and 2) the model is quite simple, compared to the complexity of cells.

We can model the shape of cells using energy minimisation. This does not imply that cells actually minimise an energy; energy minimisation is a way to take tension, pressures, and forces into account, without solving these forces at each point of the cell explicitly (Marée et al., 2007). We conclude that cell shape arises as the result of physical forces: cells control their physical properties to control their shape.

3.7 Résumé français

La drosophile a, comme tous les insectes, des yeux composés de plusieurs centaines de facettes identiques. Au milieu de chaque facette se trouvent quatre cellules, les cellules cône, qui sécrètent la lentille. Hayashi et Carthew (2004) ont étudié les arrangements et la forme de ces cellules. Ils ont observé premièrement que, dans un mutant dans lequel le nombre de cellules cône change par facette (entre une et six cellules), ces cellules s'arrangent comme s'arrangent des bulles de savon en nombre égal. Deuxièmement, la forme, et parfois l'arrangement de ces cellules change si l'expression des molécules d'adhésion est changée. Deux molécules sont importantes, la E- et la N-

cadhérine : la première se trouve sur toutes les interfaces cellulaires de la facette, la deuxième seulement entre les cellules cône.

La première observation décrite ci-dessus donne lieu à l'hypothèse que l'arrangement des cellules est gouverné par les mêmes propriétés physiques que l'arrangement des bulles de savon. La deuxième observation semble confirmer que la tension des interfaces y est pour quelque chose, puisqu'une diminution de l'adhésion augmente la tension d'interface, ce qui se voit dans un changement des angles de contact aux jonctions de trois cellules.

Nous testons d'abord cette hypothèse, en modélisant les cellules comme des entités qui minimisent leur surface. Cette minimisation prend en compte un seul paramètre biologique, l'adhésion différentielle. Puisque les interfaces entre les cellules cône portent deux types de cadhérines, et les autres n'ont qu'un type, nous supposons que l'adhésion entre les cellules cône est plus forte qu'ailleurs, donc la tension est plus faible.

Ce modèle ne réussit pas à décrire à la fois le type sauvage avec des paramètres simples, et les mutants en changeant seulement le paramètre correspondant à la propriété biologique mutée.

Dans un deuxième modèle, nous tenons compte du fait que chaque cellule a sa propre membrane, qui est tendu à cause de la contractilité du cytosquelette sous-jacent, et qui a tendance à s'étendre à cause de l'adhésion. Avec ce modèle, nous trouvons un jeu de paramètres qui permet de décrire le type sauvage et 22 mutants, avec 6 paramètres libres.

Ceci montre que l'analogie entre cellules et bulles n'est pas due à une ressemblance des propriétés physiques individuelles : les cellules ne minimisent pas leur périmètre total. Toutefois, les cellules constituent, comme les bulles, un système qui pave le plan sans trous ni recouvrements, dont les constituants individuels sont sous tension. On peut décrire leur forme par la minimisation d'une autre énergie, qui tient compte de l'adhésion et la contractilité du cytosquelette.

Adhesion and contraction in cell sorting of zebrafish germ layers

4.1 Introduction: the zebrafish and gastrulation

The zebrafish (*Danio rerio*) is a model organism for vertebrate developmental biology. It is easy to observe, because the embryos develop outside of the body, and are transparent (Montero and Heisenberg, 2004). The reader is invited to look for movies of zebrafish development on the Internet to appreciate these properties.

Gastrulation is the transformation of the unstructured blastula to an embryo with three germ layers (endoderm, mesoderm and ectoderm; this definition from Solnica-Krezel (2005)); it happens very early in development, and is conserved throughout vertebrates. As described by e.g. Montero and Heisenberg (2004); Solnica-Krezel (2005), in early zebrafish development, the dividing cells initially stay at the animal pole, on top of a big yolk cell. They spread over the yolk cell, a process called epiboly. The first separation of the germ layers is brought about by ‘internalisation’, a process during which cells that become ‘mesendoderm’ move inwards through the blastopore (the arrow in Figure 4.1). Then, ‘convergent extension’ elongates these layers and establishes a body axis.

Gastrulation thus involves engulfment of the yolk, differential movement of ectoderm and mesendoderm cells, intercalation: processes which seem to require coordination between cells. This is achieved by signalling pathways that often have cadherin or cytoskeletal molecules as their downstream targets (Montero and Heisenberg, 2004). Since the different germ layers move

This chapter is based on a publication: Krieg, Arboleda-Estudillo, Puech, Käfer, Graner, Müller and Heisenberg, *Nat. Cell Biol.*, vol. 10, no. 4, pp. 429-436, 2008. For more information on the experimental methods, readers are advised to consult that publication.

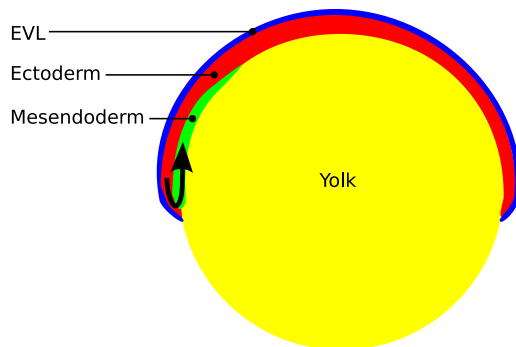


Figure 4.1: Schematic representation of early gastrulation in the zebrafish. EVL = enveloping cell layer. The green cell layer gives rise to both the mesoderm and endoderm, hence the term mesendoderm. The animal pole of the embryo is at the top, the vegetal pole at the bottom. At the margin (blastopore), cells move as indicated by the arrow.

in different directions (the ectoderm engulfs the yolk and moves towards the vegetal pole, while at the same time the mesendoderm moves towards the animal pole), the adhesive properties of the cells could be crucial to ensure tissue integrity.

Schötz et al. (2008) mixed cells of different germ layers, and saw that they sorted out: the positions that were adopted by the germ layers in these experiments could be predicted by their aggregate surface tensions. Because differences in cadherin expression are known to exist (Montero and Heisenberg, 2004), and changing cadherin expression changes the aggregate surface tensions as well as the sorting behaviour (Schötz et al., 2008), the Differential Adhesion Hypothesis (Section 1.3.1) seems to explain germ layer positioning.

In this chapter, we will see that more detailed experiments are not compatible with this simple picture, suggesting that adhesion is not the only parameter determining cell sorting in the zebrafish germ layers.

4.2 Overview of experiments

4.2.1 General

The experiments (this Section 4.2 and Figure 4.2-4.6) were conducted by M. Krieg (BIOTEC, *Technische Universität Dresden*) and Y. Arboleda (Max-Planck-Institute for Molecular Cell Biology and Genetics, Dresden).

To generate ectoderm cells, *MZ-oepl* mutants were used, which contain only ectoderm cells. Endo- and mesoderm-only embryos were created by injecting mRNA and morpholinos. Morpholinos are chemically altered antisense DNA oligomers (Heasman, 2002); these antisense sequences bind to the corresponding translated mRNA, which causes the destruction of the mRNA molecule. In this way, a gene is ‘silenced’. The injection of mRNA just causes a protein to be produced. To obtain embryos containing uniquely endoderm cells, *casanova* mRNA was injected, while for mesoderm cells, *cyclops* mRNA was injected together with *casanova* morpholino. These embryos containing one cell type were dissociated at the blastula stage, by placing them in medium containing EDTA, which sequesters the calcium ions needed for cadherin-mediated adhesion. The embryos were gently mixed, and the isolated cells could then be used for the experiments.

4.2.2 Cell sorting

Cells of two types were mixed, and allowed to aggregate in hanging drops. Figure 4.2 shows snapshots of the three different combination of the three cell types. The ectoderm cells always end up at the center of the aggregate, while neither meso- nor endoderm completely envelops the other.

Classically, cell sorting experiments are interpreted using the Differential Adhesion Hypothesis (DAH, Steinberg, 1963; Section 1.3.1). It suggests that an aggregate of ectoderm cells has 1) a higher surface tension and thus 2) that ectoderm cells adhere more strongly to one another than cell of the other types do. The difference between the mesoderm and the endoderm cells would be smaller: as expressed by Eq. [1.3] and Eq. [1.4], complete surrounding of cell type 1 by cell type 2 occurs if $\sigma_1 > \sigma_2 + \sigma_{12}$, where σ_1 and σ_2 are the aggregate-medium surface tensions, and σ_{12} is the surface tension at the interface of the cell types 1 and 2.

4.2.3 Adhesion strength

To estimate the strength of the adhesion of the cells, the force necessary to separate two adhering cells was measured using atomic force microscopy (AFM; Puech et al., 2005; Helenius et al., 2008). The substrate and the cantilever were both coated with concanavalin A, to which the cells adhere firmly. As illustrated in Figure 4.3, the cells were brought into contact, and left during 1-60 sec. Then, the cantilever moved away from the substrate with a speed of 10 $\mu\text{m/s}$, until the cells were completely separated. The maximum force (F_{max}) was taken as a measure of the adhesion strength. The force required to separate the cells depends on their contact time,

4. CELL SORTING: ADHESION AND CONTRACTION

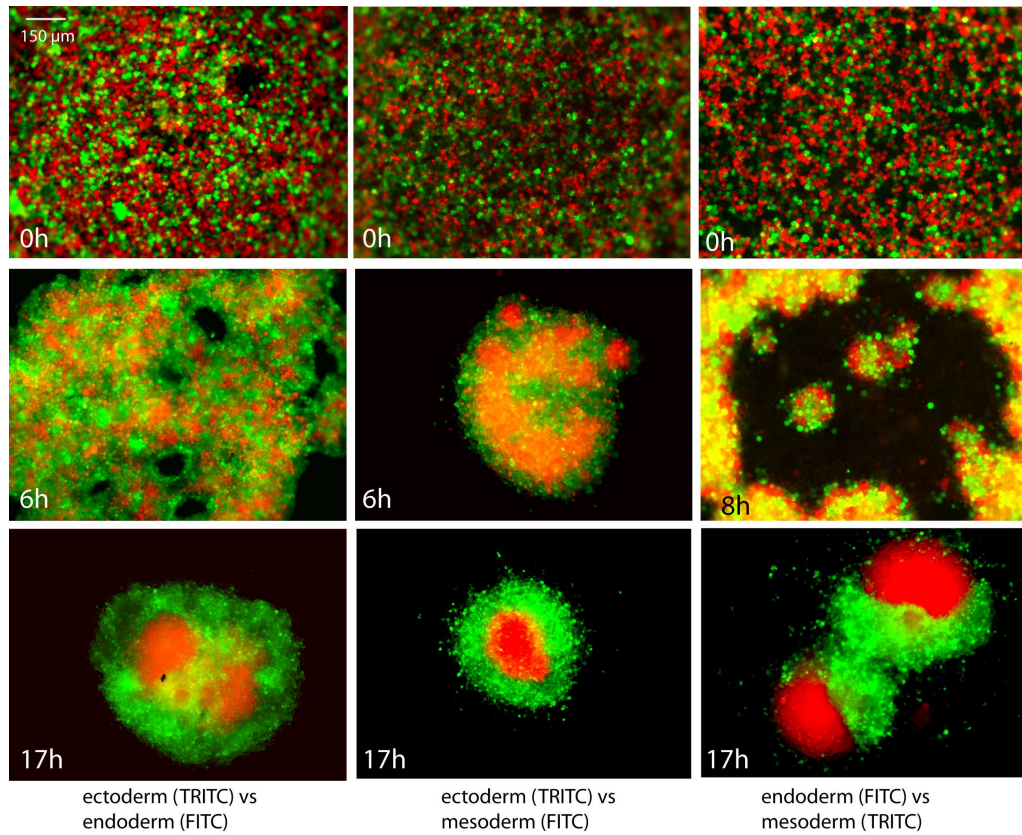


Figure 4.2: Cell sorting experiments. Cells are fluorescently labelled red (TRITC) or green (FITC). Columns present one experiment (two out of three cell types) at 0, 6 and 17 hours. Ectoderm cells (red in the left and middle experiment) are always enveloped by the other types, while endoderm partially engulfs mesoderm. The right bottom image shows two separate aggregates with complete cell sorting. Images courtesy M. Krieg.

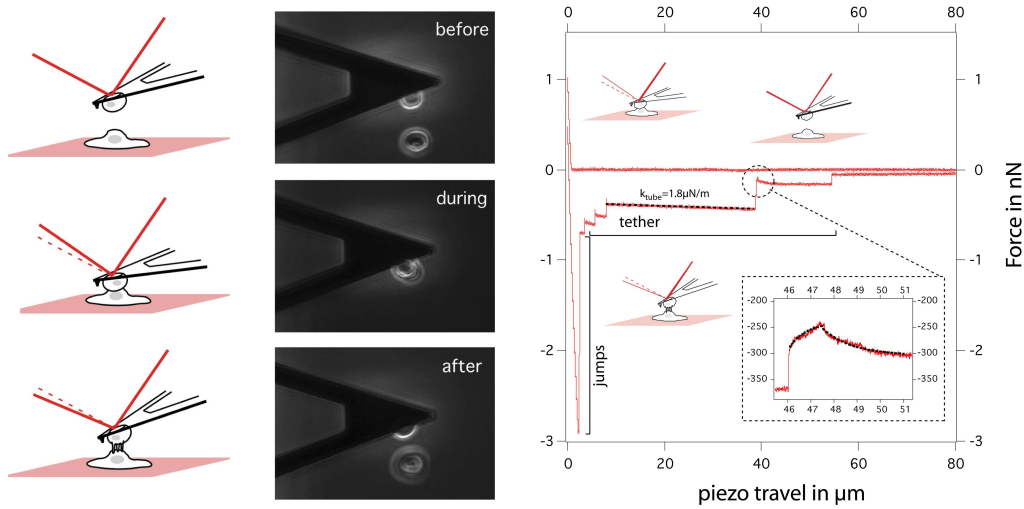


Figure 4.3: Atomic force microscopy (AFM) used to measure adhesive forces. Cells are brought into contact and separated again. The force is measured by the deflection of the cantilever. The force-distance curve shows the largest forces immediately after the cantilever starts moves away from the substrate. Separation of the cells is visible as a stepwise decrease of the force (“jumps”). At the end, tethers connect both cells, and complete separation is achieved at distances equalling several cell diameters. Images courtesy of M. Krieg.

but for all contact times, qualitatively the same results are found: the force required to separate two cells was smaller for ectoderm cells than for endoderm or mesoderm cells (Figure 4.4a). Furthermore, the adhesion strength between two cells of different cell types (heterotypic adhesion) was significantly lower than the adhesion strength of two endoderm or mesoderm cells (Figure 4.4b).

Figure 4.4c shows that the maximum force diminished dramatically when cadherin was not functional (when depleting the medium of calcium) or not present (when *E-cadherin* was silenced by a treatment with morpholinos), and that the differences between the cell types disappeared. In addition, western blot analysis (data not shown) revealed that ectoderm cells had less membrane-bound cadherins than the other cell types.

Thus, both the AFM and cadherin experiments suggested that the ectoderm cells adhere less to each other than both other cell types. This contradicts the predictions of the DAH based on the cell sorting experiments.

4. CELL SORTING: ADHESION AND CONTRACTION

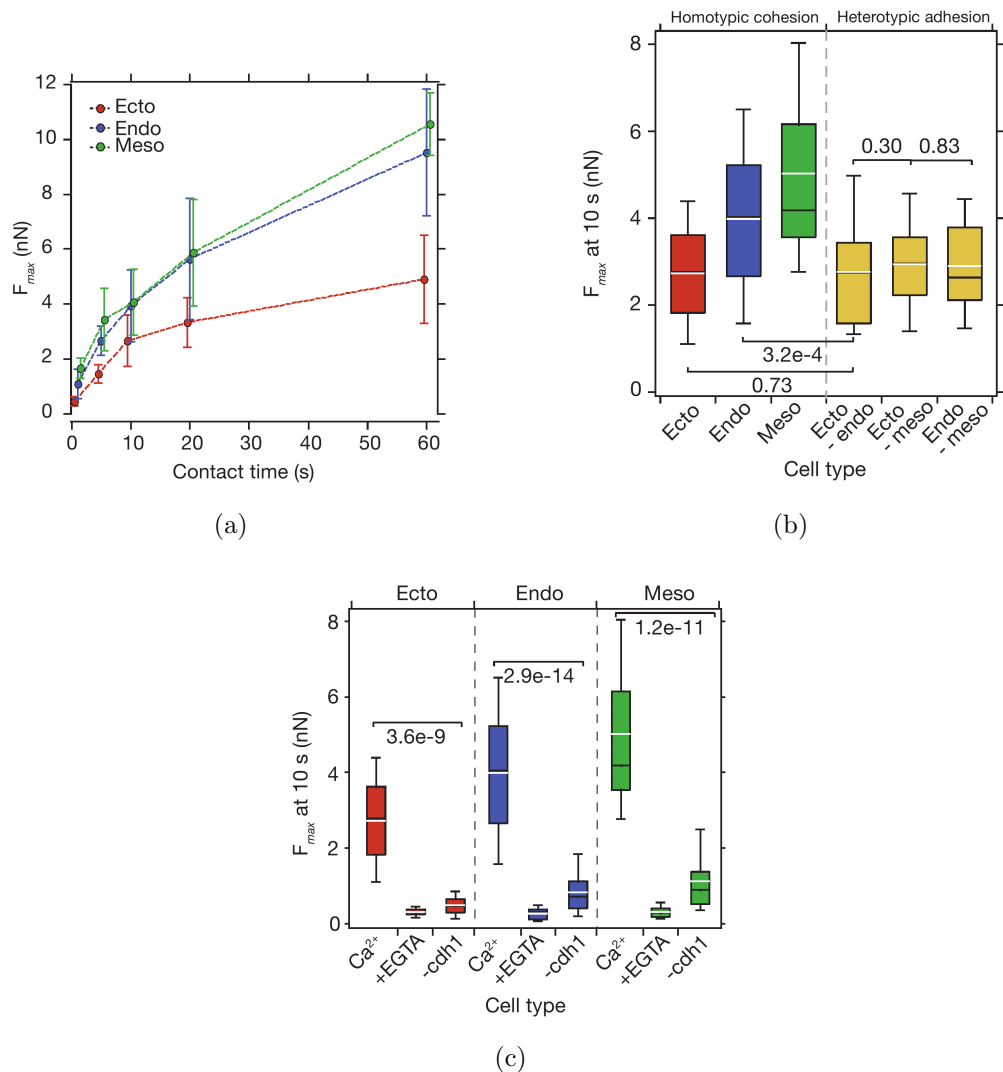


Figure 4.4: Measurement of adhesion forces by atomic force microscopy (AFM). (a) The maximum adhesion force as a function of the contact time between two cells of the same cell type. Plotted are the median values, \pm the median of the deviations. For each data point, at least 7 cells were used to obtain at least 21 measurements. (b) Homotypic versus heterotypic adhesion forces after 10 seconds of contact. Values of significance of the differences, calculated with the Mann-Whitney U tests are mentioned. In these box plots, the median values are represented by a black bar, the average values by a white one. (c) Cadherin determines the adhesion force. The force measured after a contact of 10 seconds in calcium-containing 'normal' medium (Ca^{2+}) is compared to measurements in calcium-depleted medium (EGTA) and measurements on cells treated with E-cadherin-morpholino (-cdh1). Reprinted by permission from Macmillan Publishers Ltd: Nature Cell Biology, 10 (4) 429-436, copyright 2008.

4.2.4 Cortical tension

In search for an alternative explanation, the cortex tension of the cells was measured, again using AFM (Figure 4.5a). A bead with a diameter of 5 μm was attached to the AFM cantilever, and moved towards non-adherent a cell at 1 $\mu\text{m/s}$. The indentation caused by the bead was stopped when the force measured on the cantilever reached 500 pN. The force-indentation curves (Figure 4.5b) were fitted with a linear model, to find the cortex tension T_c using the following equation (the cortical shell-liquid core or liquid droplet model (Rosenbluth et al., 2006)):

$$F = \left(2T_c \left(\frac{1}{R_c} + \frac{1}{R_b} \right) 2\pi R_b \right) \delta$$

Here, F is the force, R_c and R_b are the cell and bead radii, and δ is the indentation depth.

Ectoderm cells appeared to have a higher cortex tension than both other cell types (Figure 4.5c-d). The cortex tension was substantially reduced, and differences between cell types disappeared when treating the cells with the myosin-inhibitor blebbistatin (Figure 4.5d).

The differences of the cortical cytoskeleton between the three cell types were also seen when staining the actin filaments (Figure 4.6): in ectoderm aggregates, actin was concentrated at the interfaces of the cells with the medium, while in the other cell types the difference between cell-cell and cell-medium interfaces was less obvious or non-existent. The differences in the organisation of the cortical cytoskeleton and the cortex tension could determine the outcome of the sorting experiments.

4.3 Role of contraction in tissue surface tension

4.3.1 Cortical tension as a cell property

These experiments show that the cells with the weakest adhesion, the ectoderm cells, sort out to the center of an aggregate when mixed with endo- or mesoderm cells. Differences in the cortical tension could play a role. In a “critique” on Steinberg’s DAH, Harris (1976) proposed the ‘Differential Surface Contraction Hypothesis’, in which cells at the surface of an aggregate would have different contractile properties from those in the center.

Indeed, tissue surface tension is the result of the difference between the interfacial energies at the cell-medium and the cell-cell interface (Graner,

4. CELL SORTING: ADHESION AND CONTRACTION

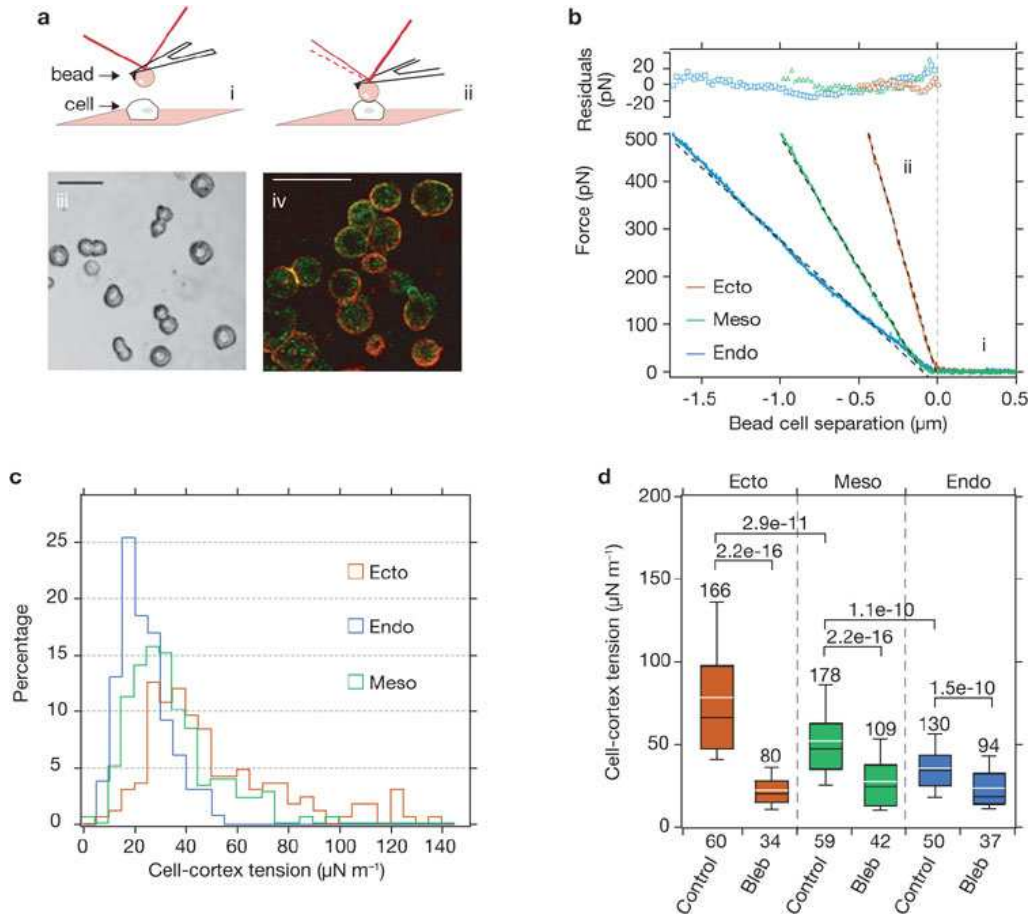


Figure 4.5: Measurement of the cortical tension using atomic force microscopy (AFM). (a) Illustration of the indentation method (i and ii), phase-contrast micrograph of the cells (iii), and actin (red, phalloidin) and myosin (green, anti-phospho-myosin antibody) stained cells (iv). Scale bars are 50 μm. (b) Examples of force-indentation curves for the three different cell types. Dotted lines are the linear fits, residuals of these fits are shown in the upper graph. (c) Histograms of the fitted cortex tensions of the three cell types. (d) Comparison of the cortex tension for the three cell types, without and with treatment with 50 μM blebbistatin (Bleb). In the boxplots, the median is represented by a black line, the mean by a white one. Sample size is indicated above each box, the number of different cells below the x-axis. The values above the brackets are the significance values for the tested combinations (Mann-Whitney U test). Reprinted by permission from Macmillan Publishers Ltd: Nature Cell Biology, 10 (4) 429-436, copyright 2008.

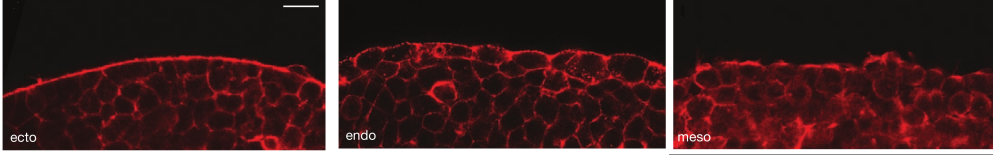


Figure 4.6: *F-actin stained with phalloidin, in aggregates of ectoderm, endoderm, and mesoderm. Reprinted by permission from Macmillan Publishers Ltd: Nature Cell Biology, 10 (4) 429-436, copyright 2008.*

1993). We have seen in Chapter 3 that adhesion energy and cortex tension add up to determine the interfacial tension (Eq. [3.3]); more precisely, the contractile cortical cytoskeleton creates tension which is diminished by adhesion (Graner, 1993; Brodland and Chen, 2000; Lecuit and Lenne, 2007).

In Eq. [3.3], it is the adhesion energy density J that co-determines the interfacial tension, while the AFM measurements yield forces. We do not know how exactly the force needed to separate two cells F_{max} (Figure 4.4) is related to this surface energy: the force depends on the speed of pulling (Bell, 1978; Merkel et al., 1999) and the cell deformation (Bell et al., 1984). We would thus need a complete model of the cell deformation, including the membrane tension and elasticity, and possibly the viscosity of the cytoplasm and cortex, to calculate the adhesion energy density from force measurements. Such a model is not available; we therefore only use a weak hypothesis that the force correlates with the adhesion energy density, and we model the experiments qualitatively.

We further simplify the modelling, and use a 2D energy function based on Eq. [3.2]:

$$\mathcal{E} = - \sum_{\text{interfaces}} J_{ij} P_{ij} + \sum_{\text{cells}} [T_i P_i + \lambda_P (P_i - P_0)^2 + \lambda_A (A_i - A_0)^2] . \quad (4.1)$$

The interfacial tension is an energy change associated with a perimeter change (Eq. [2.8]); in this case it is given by:

$$\gamma_{ij} = \frac{\partial \mathcal{E}}{\partial P_{ij}} = -J_{ij} + T_i + T_j + 2\lambda_P (P_i - P_0) + 2\lambda_P (P_j - P_0) . \quad (4.2)$$

The differences in the cortical tension measurements are represented by T_i , an extra tension term, that we first assume to be determined by the cell type of cell i only. T_i acts as a constant increment of the cortical tension T_i^c . The cortical tension of cell i is now:

$$T_i^c = T_i + 2\lambda_P (P_i - P_0) , \quad (4.3)$$

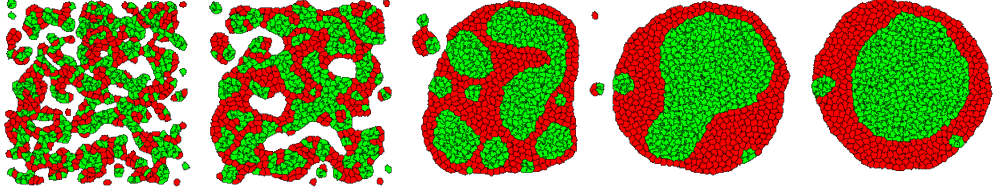


Figure 4.7: Simulation of cell sorting of ectoderm (red) and endoderm (green) cells, with cell specific extra tensions T_i (Eq. [4.1]). Snapshots are shown at 16, 100, 2600, 107900, and 300000 MCS. Parameters are $J_{ecto,ecto} = J_{ecto,endo} = 200$, $J_{endo,endo} = 300$, $T_{ecto} = 50$, $T_{endo} = 0$, $A_0 = 50$, $\lambda_A = 25$, $P_0 = 0.8 \times 11.3 \times 2\sqrt{\pi A_0}$, $\lambda_P = 0.5$, $\tau = 300$. Simulations are performed on a square grid of 230×230 pixels.

so we can write:

$$\gamma_{ij} = -J_{ij} + T_i^c + T_j^c. \quad (4.4)$$

The adhesion J_{ij} depends on the cell types of cells i and j . The types can be *ecto*, *endo*, and *meso*, and the medium is represented by M . Thus, to qualitatively model the experiments, we use $J_{ecto,ecto} = J_{ecto,meso} = J_{ecto,endo} = J_{endo,meso}$, and $J_{ecto,ecto} < J_{endo,endo} < J_{meso,meso}$. There is no adhesion with the medium, $J_{i,M} = 0$. Taking the cortical tension measurements into account yields $T_{ecto} > T_{meso} > T_{endo}$. We can model the difference in cortical tension as a difference in λ_P or P_0 per cell: this yields qualitatively the same results.

Figure 4.7 shows an example of an attempt to model cell sorting with these assumptions. The endoderm cells, that have the strongest adhesion, sort out to the center of the aggregate, as expected according to the DAH, and thus in contradiction with the experiments: the extra tension T_i does not play a role. To understand why, we consider the macroscopic aggregate surface tensions σ . We have related the surface tension in Section 1.2.2 to molecular affinities for liquids, and in Section 1.3.1 to adhesion energies for cells.

We use this same approach to understand how the cortical tension of cells influences the aggregate surface tension. On the cell scale, the interfacial tension γ_{ij} is given by Eq. [3.3]; it is the energy needed to increase an interface by one unit, and is equivalent to the surface energy. In the following, we denote with capitals the cell types I , J and the medium M . Analogous to Figure 1.7, to establish one unit of interface between I and J with surface energy γ_{IJ} , in each cell type, cells have to be separated over half a unit of surface, requiring an energy of $\gamma_{II}/2 + \gamma_{JJ}/2$. The following equations thus express the aggregate surface tensions as a function of the

cell interfacial tensions:

$$\begin{aligned}\sigma_{IJ} &= \gamma_{IJ} - \frac{\gamma_{II} + \gamma_{JJ}}{2} \\ \sigma_{IM} &= \gamma_{IM} - \frac{\gamma_{II}}{2} .\end{aligned}\quad (4.5)$$

We calculated the interfacial tensions γ_{ij} before (Eq. [4.4]), and substitute them in the equations for the aggregate surface tensions σ :

$$\begin{aligned}\sigma_{IJ} &= -J_{IJ} + \frac{J_{II} + J_{JJ}}{2} \\ \sigma_{IM} &= \frac{J_{II}}{2} .\end{aligned}\quad (4.6)$$

Here, the cortex tension terms cancel out. In this way, the extra tension T^c does not contribute to aggregate surface tension, and does not determine the outcome of cell sorting.

4.3.2 Interface-specific cortical tension

As Figure 4.6 shows, in the ectoderm cells, the cortical actin cytoskeleton is denser at cell-medium than at cell-cell interfaces. The extra tension T should thus be interface-specific, which we note T_{ij} . T_{ij} is a property of cell i at its interface with cell j , and cell j can have another extra tension T_{ji} at its interface with i . The energy function now is:

$$\mathcal{E} = \sum_{\text{interfaces}} (-J_{ij} + T_{ij} + T_{ji}) P_{ij} + \sum_{\text{cells}} [\lambda_P (P_i - P_0)^2 + \lambda_A (A_i - A_0)^2] .\quad (4.7)$$

One interface consists of two cortices, that both should be counted. The interfacial tension is:

$$\gamma_{ij} = \frac{\partial \mathcal{E}}{\partial P_{ij}} = -J_{ij} + T_{ij} + T_{ji} + 2\lambda_P (P_i - P_0) + 2\lambda_P (P_j - P_0) ,\quad (4.8)$$

which we can rewrite as:

$$\gamma_{ij} = -J_{ij} + T_{ij}^c + T_{ji}^c\quad (4.9)$$

defining the effective cortical tension as:

$$T_{ij}^c = T_{ij} + 2\lambda_P (P_i - P_0) .\quad (4.10)$$

The surface tensions for the aggregates of cell types I and J are then (Eq. [4.5]):

$$\begin{aligned}\sigma_{IJ} &= -J_{IJ} + T_{IJ}^c + T_{JI}^c - \frac{-J_{II} + 2T_{II}^c - J_{JJ} + 2T_{JJ}^c}{2} \\ \sigma_{IM} &= \gamma_{IM} - \frac{\gamma_{II}}{2} = T_{IM}^c - \frac{-J_{II} + 2T_{II}^c}{2}.\end{aligned}\quad (4.11)$$

In contrast to Eq. [4.6], the cortex tension here does influence the aggregate surface tensions, and can thus influence cell sorting.

We test in simulations whether, with this model, it is indeed possible to have strongly adhering cells surrounding weakly adhering ones. The cortical tensions that have been measured and shown in Figure 4.5 are supposed to be representative for the cell-medium interface: $T_{ecto,M} > T_{meso,M} > T_{endo,M}$ (as also suggested by Figure 4.6). There are no data available to assess the hierarchy of the cortical tensions at cell-cell interfaces. From the actin staining experiments (Figure 4.6) we assume that $T_{ecto,ecto} < T_{ecto,M}$; for simplicity we set all values $T_{IJ} = 0$ when $I, J \neq M$.

As Figure 4.8 shows, we find parameters for which the simulations agree with the experiments: the weakly adhering ectoderm cells end up in the middle of the aggregate. The differences between the mesoderm and endoderm are too small to cause complete envelopment of either one of the cell types, in agreement with the experiments (Figure 4.2).

According to Eq. [4.2] and Eq. [4.8], γ varies with perimeter fluctuations of the cells (cf Chapter 3). In the preceding calculations, we assumed that it is, on average, constant: the agreement between the predictions made by Eq. [4.6] and Eq. [4.11] and the simulations in Figure 4.7 and Figure 4.8 indicate that, on the scale of the aggregate, this is a reasonable assumption.

There are more ways to model interface-specific cortex tension. In Chapter 3 we argued that the term $2\lambda_P(P - P_0)$ in Eq. [3.3] (which appears also in Eq. [4.2] and Eq. [4.8]) described the cortex tension. It can thus be adapted to model interface-specific cortex tension, by making the perimeter modulus λ_P interface-specific, λ_{ij}^P . We require that the model boils down to Eq. [3.2] when there are no differences in cortex contractility between the interfaces. The energy function then becomes:

$$\begin{aligned}\mathcal{E} &= \sum_{\text{interfaces}} \left(-J_{ij} + \lambda_{ij}^P \frac{(P_i - P_0)^2}{P_i} + \lambda_{ji}^P \frac{(P_j - P_0)^2}{P_j} \right) P_{ij} \\ &+ \sum_{\text{cells}} \lambda_A (A_i - A_0)^2.\end{aligned}\quad (4.12)$$

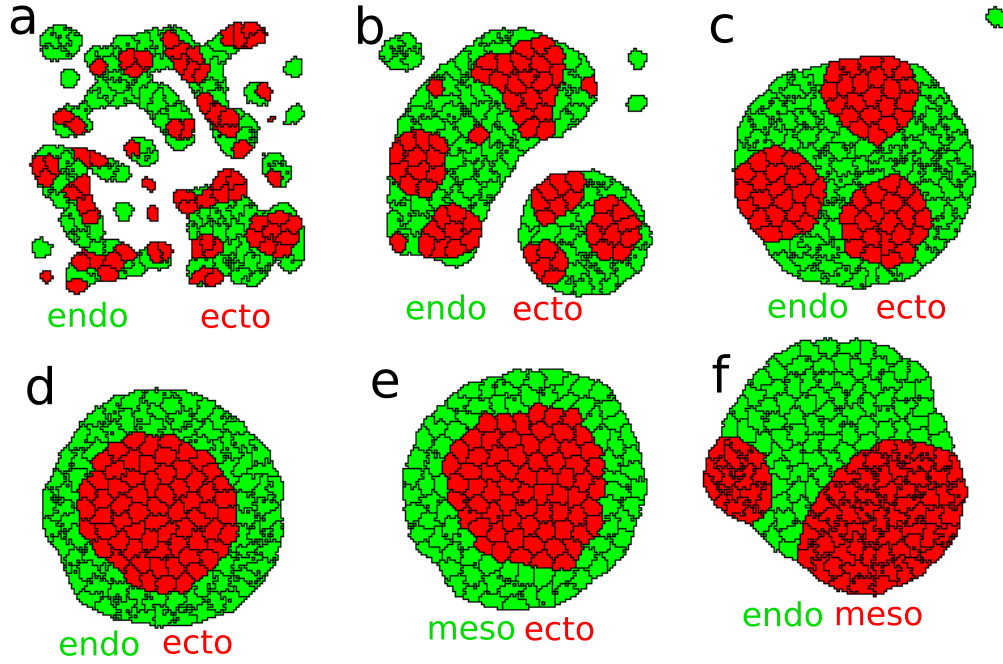


Figure 4.8: Cell sorting simulations, assuming interface specific cortex tension, Eq. [4.7]. **a-d**: Snapshots of the simulation of the sorting of ectoderm (red) and endoderm (green) cells (a: 16 MCS, b: 512 MCS, c: 16384 MCS, d: 32768 MCS). **e**: Simulation of ectoderm (red) and mesoderm (green) cell sorting, snapshot at 32768 MCS. **f**: Simulation of mesoderm (red) and endoderm (green) cell sorting, snapshot at 32768 MCS. The adhesion energies are $J_{ecto,ecto} = J_{ecto,endo} = J_{ecto,meso} = J_{endo,meso} = 200$, $J_{endo,endo} = 300$, $J_{meso,meso} = 400$, while there is no adhesion with the medium ($J_{i,M} = 0$). The extra tensions are $T_{ecto,M} = 210$, $T_{meso,M} = 50$, and $T_{ij} = 0$ at all other interfaces. Other parameters are $A_0 = 50$, $\lambda_A = 25$, $P_0 = 0.1 \times 11.3 \times 2\sqrt{\pi A_0}$, $\lambda_P = 0.3$, $\tau = 300$. Simulations are performed on a square grid of 130×130 pixels.

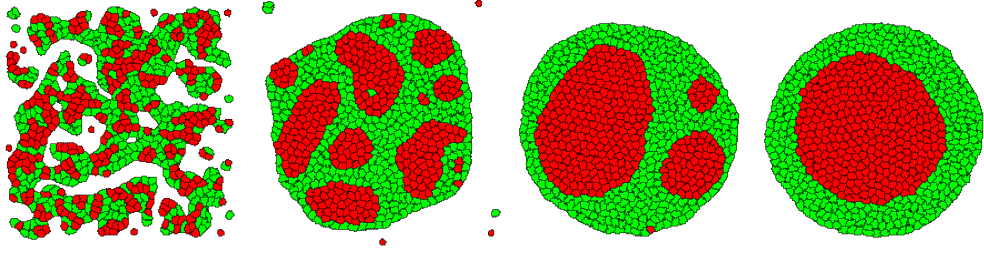


Figure 4.9: Cell sorting of ectoderm (red) and endoderm (green) cells, using differential contractility, Eq. [4.12]. Snapshots are shown at 32, 4096, 65536 and 262144 MCS. Parameters are $J_{ecto,ecto} = J_{ecto,endo} = 200$, $J_{endo,endo} = 300$, $\lambda_{ecto,M}^P = 0.8$, $\lambda_{endo,M}^P = \lambda_{endo,ecto}^P = \lambda_{ecto,endo}^P = 0.3$, $A_0 = 50$, $\lambda_A = 25$, $P_0 = 0.1 \times 11.3 \times 2\sqrt{\pi A_0}$, $\tau = 300$. The grid is 230×230 pixels.

This considerably complicates the calculation of $\Delta\mathcal{E}_{i \rightarrow i'}$ (Eq. [2.3]) for each copy attempt, because a change in the length of one interface influences the energy of the whole cell perimeter in a nonlinear way. This increases the calculation time.

When using the same adhesion energies as in used for the other models, we simulate the cell sorting of endo- and ectoderm cells. Differential cortical contractility is here modelled as $\lambda_{ecto,M}^P > \lambda_{endo,M}^P$, and this causes the weakly adhering ectoderm cells to sort out to the center (Figure 4.9), leading qualitatively to the same results as in experiments (Figure 4.2) and previous simulations with differential cortical tension (Figure 4.8). To distinguish between the implementations of the differences in the cortical cytoskeleton, a quantitative analysis would be necessary, but data are lacking.

4.3.3 Gastrulation

The cells that sort out to the aggregate's center are the ectoderm cells which occupy a more outward position than the endo- and mesoderm cells in the intact embryo (Figure 4.1). One explanation for the inverted positions could be the developmental history: gastrulation is not a random sorting process, and the cells differentiate approximately at the position of invagination (arrow in Figure 4.1). The sorting experiments indicate that the cells do not mix: once the layers are established, position inversion will be difficult.

A difference between the *in vitro* sorting experiments and the gastrulation (*in vivo*) is the presence of other cell types. The ecto- and endoderm cells partially surround a huge syncytial yolk cell, and are surrounded by an 'enveloping cell layer' (EVL), as shown in Figure 4.1. Can adhesive

and tensile properties of the ectoderm and mesoderm at the interfaces with these other tissues change their positions?

We simulate cell sorting of ectoderm and mesoderm cells in the presence of EVL cells and a yolk cell, Figure 4.10A-C. Measurements of the adhesion of the germ layer cells to either the yolk or the EVL cells are lacking. We assume that the adhesion of the germ layer cells to the yolk is equal to their homotypic adhesion, $J_{yolk,meso} = J_{meso,meso}$ and $J_{yolk,ecto} = J_{ecto,ecto}$, and that the EVL cells have the same adhesive properties as ectoderm cells, $J_{EVL,ecto} = J_{EVL,meso} = J_{EVL,EVL} = J_{ecto,ecto}$. Furthermore, neither the yolk nor the EVL cells have differences in cortical tension, and the cortical tension of the germ layer cells at interfaces with EVL cells or the yolk is the same as at other cell-cell interfaces. With these minimal assumptions, we need to adjust only one additional parameter, the adhesion of the EVL cells to the yolk, $J_{EVL,yolk}$, which should be lower than $J_{ecto,yolk}$, in order to obtain the *in vivo* position of all four cell types (Figure 4.10A-C).

We further investigate whether these same properties can explain the cell movements that take place at the germ ring margin during gastrulation (arrow in Figure 4.1). At this position, ectoderm cells differentiate into mesendoderm cells, that move towards the animal pole in between the ectoderm and the yolk. We simplify the geometry of the germ ring margin, and simulate this behaviour, Figure 4.10D-F. In addition to the parameters used for the simulation of cell sorting of the four cell types (Figure 4.10A-C), we only need to diminish the adhesion between the yolk and ectoderm cells, $J_{yolk,ecto}$. This does not influence the cell sorting: the same results as in Figure 4.10A-C are obtained.

4.4 Discussion

4.4.1 Cortical tension and the DAH

The aggregate surface tension σ is a collective property of a group of cells. The experiments and simulations mentioned above help to understand which cell-level parameters determine σ . In Figure 4.11, the quantities that act on different levels are summarised. First, at the collective level, Figure 4.11A, the aggregate surface tension σ is the result of a difference between the tension at the cell-medium interface, γ_{iM} , and the tension at cell-cell interfaces, γ_{ij} (see Eq. [4.5]). These interfacial tensions γ are effective tensions, which are determined by the cell-level properties of cortical tension, T^c , and adhesion, J (Figure 4.11B, Eq. [4.9]).

4. CELL SORTING: ADHESION AND CONTRACTION

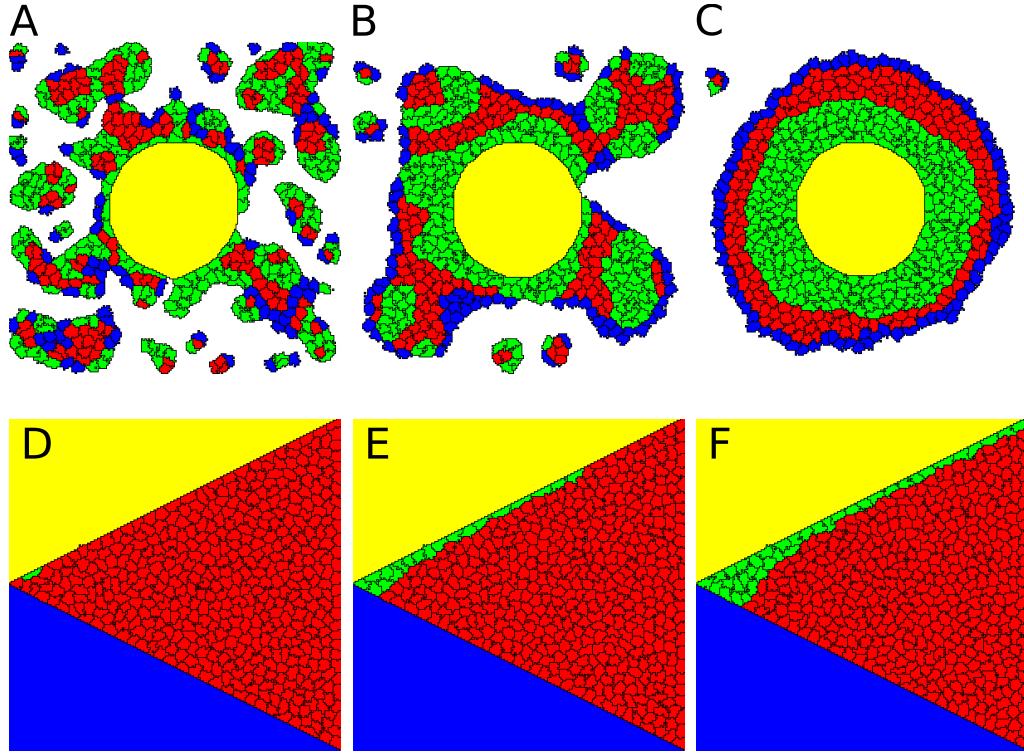


Figure 4.10: Simulation of ectoderm (red) and mesoderm (green) cells, in the presence of EVL cells (blue) and a yolk cell (yellow). **A-C**: Cell sorting, snapshots at 100, 2500 and 17800 MCS. Parameters are as in Figure 4.8 and $J_{EVL,ecto} = J_{EVL,meso} = J_{EVL,EVL} = 100$, $J_{EVL,yolk} = 0$, $J_{yolk,ecto} = 100$, $J_{yolk,meso} = 400$, $J_{yolk,M} = J_{EVL,M} = 0$, and $T_{EVL,i} = T_{yolk,i} = 0$ for all cell types i . **D-F**: Involution at the germ ring margin. At regular intervals (each 800 MCS), the leftmost ectoderm cell differentiates into a mesoderm cell. Parameters are the same as for A-C, except that $J_{yolk,ecto} = 50$, and the yolk and EVL are fixed, and do not have area or perimeter conservation ($\lambda_P = \lambda_A = 0$).

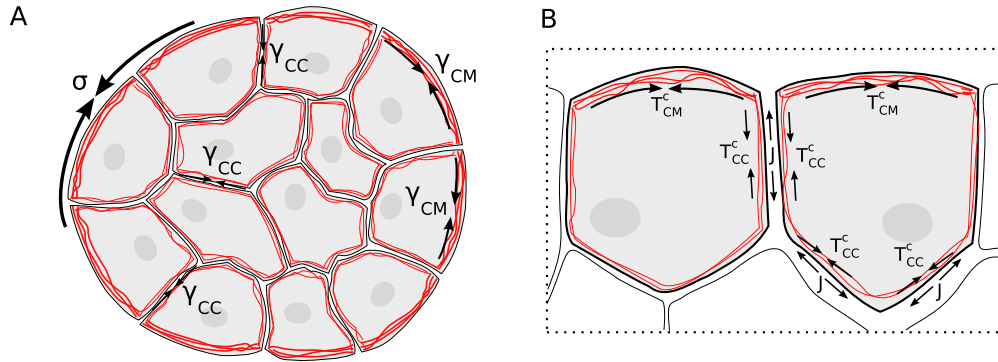


Figure 4.11: Schematic representation of a cell aggregate and the tensions. Original image courtesy M. Krieg.

Only those cellular properties that are different at cell-cell interfaces and cell-medium interfaces thus contribute to the aggregate surface tension. As was postulated (Steinberg, 1963) and shown (Foty and Steinberg, 2005) in the work on the DAH, adhesion typically increases the aggregate surface tension: no cadherin-mediated adhesion is possible with the medium. There are, however, multiple other ways in which cell-cell interfaces can differ from cell-medium interfaces. Differences in cortical tension, as presented here, are one of them, but other mechanisms are not excluded (cf Harris, 1976).

4.4.2 Towards a quantitative description

Eq. [4.11] can in principle be tested quantitatively, but at the moment, not all terms have yet been quantified. Table 4.1 summarises the available measurements. Of these, the adhesion force is not directly linked to the adhesion energy density, which acts in cell sorting. It is reasonable to assume that the adhesion force is positively correlated to the adhesion energy density.

In order to use Eq. [4.11], we have to make two strong assumptions; we discuss their validity afterwards:

1. treatment with E-cadherin morpholino does not change the cortex tension;
2. the adhesion energy density is directly proportional to the adhesion force.

4. CELL SORTING: ADHESION AND CONTRACTION

Table 4.1: Measured quantities for the zebrafish germ layers cells and aggregates. *e-cadMO* is E-cadherin morpholino. Aggregate surface tensions by Schötz et al. (2008), given as mean±standard error. Adhesion forces for homotypic contacts, after 10 seconds of contact time, values are median±mad (median absolute deviation), measured as described in Section 4.2.3. Cortex tension values read from Figure 4.5. Schötz et al. (2008) used lower amounts of E-cadherin morpholino than those used for the measurements in Figure 4.4: the amount of morpholino used probably affects the reduction in adhesion (C.-P. Heisenberg, pers. comm.).

cell type	aggregate surface tension (mN/m)	adhesion force (pN)	cortex tension (μN/m)
ectoderm	0.75 ± 0.06 0.80 ± 0.07	2767 ± 925	≈ 70
ectoderm + e-cadMO	0.33 ± 0.02	441 ± 32	-
mesoderm	0.43 ± 0.08	4178 ± 1199	≈ 50
endoderm	-	4028 ± 1310	≈ 35

Then, the difference in the surface tension of a wild-type ectoderm aggregate $\sigma_{ecto,M}$ and an E-cadherin morpholino treated aggregate $\sigma_{ecMO,M}$ is

$$\begin{aligned}
 \sigma_{ecto,M} - \sigma_{ecMO,M} &= T_{ecto,M}^c + J_{ecto,ecto}/2 - T_{ecto,ecto}^c \\
 &\quad - T_{ecto,M}^c - J_{ecMO,ecMO}/2 + T_{ecto,ecto}^c \\
 &= (J_{ecto,ecto} - J_{ecMO,ecMO})/2.
 \end{aligned}$$

Thus, $(J_{ecto,ecto} - J_{ecMO,ecMO})/2 = 0.75 - 0.33$ mN/m = 0.43 mN/m. Using assumption (2), $J_{ecMO,ecMO} = (4.4/28) J_{ecto,ecto}$ then yields $J_{ecto,ecto} = 1.0$ mN/m. Again from Eq. [4.11], we can obtain an estimate for the difference in cortical tensions at the cell-cell and cell-medium interfaces for the ectoderm: $T_{ecto,M}^c - T_{ecto,ecto}^c = \sigma_{ecto,M} - J_{ecto,ecto}/2 = 0.25$ mN/m.

Cortical tension has been measured experimentally for other cell types. E.g. Thoumine et al. (1999) report values for adherent fibroblasts that lie between 200 and 400 μN/m, significantly higher than those listed in Table 4.1. The adhesion energy $J_{ecto,ecto} = 1.0$ mN/m is comparable to the estimations of Frisch and Thoumine (2002) for fibroblasts (0.6 mN/m).

This adhesion energy $J_{ecto,ecto}$ (1.0 mN/m) is about 15 times larger than the measured cortex tension (Table 4.1). According to Eq. [4.8], this would lead to negative values of the interfacial tension, which is not realistic. The difference between the cortical tensions at cell-cell and cell-medium

interfaces ($T_{ecto,M}^c - T_{ecto,ecto}^c$, 0.25 mN/m) is about four times larger than the measured cortex tension.

The values of $J_{ecto,ecto}$ and $T_{ecto,M}^c - T_{ecto,ecto}^c$ are estimated using the macroscopic measurements of the aggregate surface tension σ . These estimations do thus not agree with the cortex tension values measured on the level of the cell. We will study in Chapter 5 if this difference can be due to cellular properties.

4.4.3 Gastrulation

By means of the simulations where both yolk and EVL cells are present (Figure 4.10), we show that the cellular properties that determine *in vitro* cell sorting can also partially explain *in vivo* morphogenesis. When the cells at the blastopore become mesoderm and change their adhesive properties, cell sorting alone is sufficient for these cells to internalise towards the yolk. Subsequently, the spreading of these cells between the ectoderm and the yolk could be driven by the cells' interfacial properties as well.

Pezeron et al. (2008) show that during early gastrulation, the endoderm cells spread over the yolk cell after internalisation by means of undirected diffusion. This is compatible with the arrangement of the germ layers because of their interfacial properties: the two mechanisms together offer a simple and complete hypothesis to explain the positioning of the endoderm.

4.5 Conclusion

The ‘Differential Adhesion Hypothesis’ correctly explains how aggregates with different aggregate surface tensions sort out, but its focus on adhesion as the main parameter determining aggregate surface tension is too restricted. Adhesion undeniably influences aggregate surface tension, as was shown by Foty and Steinberg (2005) and more recently by Schötz et al. (2008). We show here that interface specific cortical tension co-determines aggregate surface tension. As is the case here, it can be even more important than adhesion, leading to results that are the contrary of the predictions of the DAH.

Differential adhesion and ‘differential surface contraction’ (Harris, 1976) are thus not contradictory. Our new hypothesis, in which both adhesion and contractility are at the origin of the cellular tensions that determine aggregate surface tension, synthesises the DAH and its alternatives.

The final configuration of cell sorting is predicted by the aggregate surface tension σ . On a collective scale, the aggregate behaviour is thus pre-

dicted by considering it as a liquid. But the properties of cells are unlike those of liquid molecules; their interactions are more than just attractive forces, and involve also cortical contractility. Describing these interactions as an interfacial tension γ allows to make the link between cell-level and collective properties.

4.6 Résumé français

Pendant la gastrulation, trois feuilletts embryonnaires (endoderme, ectoderme et mésoderme) sont créés à partir du blastula, qui est uniforme. Quand les cellules de deux des trois feuilletts sont dissociées et mélangées, elles forment un agrégat où les cellules des deux types se séparent. Schötz et al. (2008) ont montré que, conformément à l'Hypothèse d'Adhésion Différentielle (*DAH*), les positions finales de chaque type sont prédites par la tension de surface des agrégats homotypiques : l'ectoderme a la tension la plus grande, et se trouve donc entouré par les autres types cellulaires. En utilisant la *DAH*, on conclut que les cellules de l'ectoderme auraient une adhésion plus forte entre elles que les cellules des autres types.

Les propriétés adhésives des cellules ont été sondées par microscopie à force atomique (AFM), où la force maximale atteinte pendant la séparation de deux cellules est mesurée pour estimer l'adhésion. L'adhésion de deux cellules de l'ectoderme est plus faible que celle entre deux cellules des autres types, ce qui contredit la prédiction selon la *DAH*. D'autres mesures au niveau cellulaire montrent que les cellules de l'ectoderme ont la tension corticale la plus grande des trois types. La distribution d'actine dans les agrégats homotypiques est visualisée par marquage avec anticorps, ce qui montre que pour l'ectoderme, il y a plus d'actine associée aux interfaces entre les cellules et le milieu qu'aux interfaces entre cellules.

Nous testons l'effet de l'adhésion et la tension corticale par simulations. Effectivement, quand la tension corticale est uniforme, elle n'a pas d'effet sur le résultat du tri. Par contre, quand la tension corticale est plus grande aux interfaces des cellules de l'ectoderme et le milieu qu'aux autres interfaces, les simulations reproduisent le résultat des expériences de tri : les cellules de l'ectoderme finissent à l'intérieur de l'agrégat, malgré leur faible adhésion. La tension de surface de l'agrégat est déterminée par les différences entre les tensions interfaciales cellule-cellule et cellule-milieu, et les tensions interfaciales sont la somme des tensions corticales des cellules qui touchent, moins l'adhésion entre eux. Il n'est pas possible pour l'instant de quantifier l'effet des propriétés cellulaires sur la tension de l'agrégat : les

estimations des propriétés cellulaires basées sur les mesures collectives sont beaucoup plus grandes que les valeurs de tension corticales mesurées.

Dans l'embryon du poisson zèbre, l'ectoderme se trouve à l'extérieur des autres feuillets embryonnaires. En tenant compte de deux autres types cellulaires présents dans l'embryon, nous pouvons modéliser cette inversion observée *in vivo*. Les propriétés adhésives des autres types pourraient également guider les cellules du meso- ou endoderme pendant l'involution.

La DAH lie alors bien la dépendance du résultat du tri aux différences de tension de l'agrégat, mais n'inclut pas l'effet de la tension corticale, qui est ici dominante sur l'adhésion : nous proposons ici une nouvelle hypothèse.

Aggregate compression

5.1 Introduction

5.1.1 Cell aggregates

The study of aggregates of priorly dissociated cells is an important tool in the understanding of developmental processes. Its main use nowadays is associated to the study of tissue organisation (e.g. Chapter 4, Schötz et al., 2008; Ninomiya and Winklbauer, 2008). In this chapter, we try to gain insight in the behaviour of aggregates, and how this behaviour is influenced by cell-level properties. While classical approaches only use the aggregates that behave as liquids, we try to extract information from non-liquid behaviour. This is possible by using a more physical description, and opens perspectives to use the study of aggregates to predict more cellular properties than just adhesion differences.

As reviewed by Steinberg (1963), in the first half of the 20th century, several researchers noticed that dissociated cells reaggregate. If cells from different tissues or organs were dissociated and mixed, they reaggregated as well, but they also sorted out. The positions that the cells from the different tissues occupied at the end of the sorting was always the same, and often reflected the relative positions of the tissues in the intact body. Most of the hypotheses to explain this involved the action of adhesion; Steinberg (1963) hypothesised that non-selective adhesion could be the cause of this behaviour. In what has become known as the Differential Adhesion Hypothesis (DAH), he argued that quantitative difference in adhesion would be sufficient to explain cell sorting, as in the demixing of immiscible liquids (see Section 1.3.1).

This liquid analogy has been extended to the quantitative study of aggregates by Foty et al. (1994), who developed a method to estimate an

The contents of this chapter are the subject of a publication in preparation

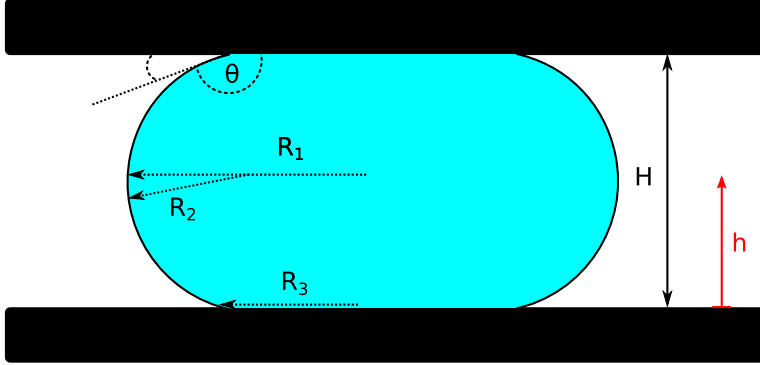


Figure 5.1: A liquid drop in a parallel plate compression apparatus, viewed sideways. R_1 and R_2 are radii of curvature, R_3 is the radius of the contact surface; θ is the contact angle; H is the distance between the plates, and h a vertical coordinate.

aggregate's surface tension. It relies on the fact that for a liquid drop in equilibrium, the only resistance to deformation comes from the surface tension (see Section 1.2.2). The surface of a liquid drop is uniformly curved, and its curvature depends on the surface tension and the pressure inside the drop. For a liquid drop at equilibrium, Laplace's law relates the curvature κ , pressure Π and surface tension σ :

$$\Pi = 2\sigma\kappa = \sigma \left(\frac{1}{R_1} + \frac{1}{R_2} \right). \quad (5.1)$$

The curvature κ is the “mean curvature”, which is the average of the principal curvatures of the surface (the minimal and maximal curvatures, which are in directions perpendicular to one another). For interfaces of liquids in equilibrium, κ is constant, but the principal radii can vary. In parallel plate compression experiments, Figure 5.1, radii are most easily measured in the plane corresponding to $h = H/2$; the radii are then R_2 , measurable in the plane of the picture, and R_1 , perpendicular to the plane of the picture.

The force that a compressed drop exerts on the plates depends on this pressure, but also on the direct pulling of the interface itself. Norotte et al. (2008) write the force balance for a drop confined between two plates, which is valid at each height $0 \leq h \leq H$ of the aggregate. One convenient plane to write the force balance, is at the surface of the plates ($h = 0$ or $h = H$):

$$\begin{aligned} F &= \Pi (\pi R_3^2) - \sigma (2\pi R_3 \sin \theta) \\ &= \sigma \left[\pi R_3^2 \left(\frac{1}{R_1} + \frac{1}{R_2} \right) - 2\pi R_3 \sin \theta \right]. \end{aligned} \quad (5.2)$$

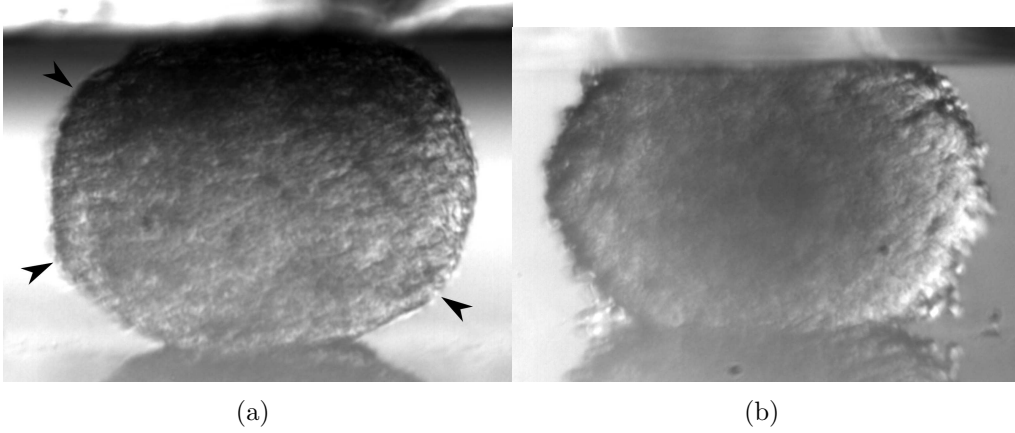


Figure 5.2: Two examples of deviations from liquid behaviour in compressed aggregates. a) At the surface of an aggregate of embryonic chicken retina cells, areas with high curvature (arrowheads) exist. b) Chinese Hamster Ovary (CHO) cells, with a very rough aggregate-medium interface. Both aggregates are about 300 μm in diameter. Images courtesy of A. Mgharbel.

The first term is the effect of the pressure, which acts on the area πR_3^2 . The second term is due to the surface, which pulls at the plates with a force $\sigma \sin \theta$, over the perimeter $2\pi R_3$ of the contact area. When the aggregate profile is convex, both contributions have opposite actions.

It is convenient as well to write this force balance for a plane halfway between the plates, $h = H/2$:

$$\begin{aligned}
 F &= \Pi (\pi R_1^2) - \sigma (2\pi R_1) \\
 &= \sigma \left[\pi R_1^2 \left(\frac{1}{R_1} + \frac{1}{R_2} \right) - 2\pi R_1 \right] \\
 &= \sigma \pi R_1 \left(\frac{R_1}{R_2} - 1 \right). \tag{5.3}
 \end{aligned}$$

The force due to the pressure here acts on an area πR_1^2 , and the force due to the surface tension (which now acts perpendicular to the plates) at the perimeter with length $2\pi R_1$.

Using the parallel plate compression apparatus allowed e.g. Duguay et al. (2003) to predict the final positions of several cell types in pairwise cell sorting experiments. Foty and Steinberg (2005) found a linear relation between the measured surface tension and the number of cadherins per cell.

However, aggregate behaviour is not always that of a liquid. In Figure 5.2a, there seem to be ‘angles’ in the profile where the curvature is very high

(arrowheads), and more flat parts. In Figure 5.2b, the aggregate profile is very irregular, and again the curvature seems unequally distributed. This indicates a more solid-like behaviour, where the shape of the aggregate is not determined by surface properties, but by stresses inside the aggregate. How can we reconcile that with the many successful applications of the compression tests?

5.1.2 Liquid and solid behaviour

The terms liquid-like and solid-like can be practical descriptors of the mechanical behaviour of tissues, if we define them better. Therefore, we need to know how materials are characterised. Three kinds of dynamic material behaviour exist: elastic, plastic, and viscous behaviour. Each material can be characterised by one, two or three of these; the three are thus compatible.

Elastic behaviour is reversible. During elastic deformation, energy is stored. This energy is released again when the object returns to its original shape. How much an object deforms (strain) as a function of the applied stress is determined by the elastic modulus.

Viscous behaviour dissipates energy, and is thus irreversible. Viscosity is the resistance to flow. It arises from the friction of elements (mostly molecules) that move relative to one another; the dissipation and the viscous force depends thus on the speed of the flow.

Plastic behaviour is also dissipative and thus irreversible. In contrast to the viscous behaviour, it is characterised by a threshold, and by a dissipation force that is independent of the flow speed. A purely plastic material resists to some stress, but for a stress higher than the threshold, it yields, and assumes a new shape. Due to the existence of a threshold, this shape change is permanent, until again a stress higher than the yield stress is applied.

Now, a simple liquid is characterised by a viscosity, which is constant for so-called Newtonian fluids, like water. Any stress is dissipated if one waits long enough. A simple solid has an elastic modulus, and a threshold: above the threshold, it either breaks, or is plastic.

A wide range of materials with intermediate properties exist: granular matter, glassy materials, foams, emulsions, gels, pastes. Marmottant and Graner (2007); Marmottant et al. (2008) describe the behaviour of a foam as viscous, elastic, and plastic, which is due to its structure: a foam consists of tightly packed (space-tiling) bubbles, that can deform, rearrange, and that contain liquid. Bubble deformation is elastic, and can thus store energy; for the rearrangements, an energy barrier separating two local energy minima

(cf Figure 1.11) acts as a threshold; the friction of the liquid molecules during flow causes the viscosity.

Figure 5.3 shows the behaviour of a foam confined between two movable plates (Rosa and Fortes, 2006; Vaz, 2008). First, we note that the interfaces between the foam and the surrounding air are concave (Figure 5.3a-c) or convex (d-e), according to the affinities between the foam and the plates; this is as expected for a liquid. Second, the profiles are irregular, and there are differences between the left and the right profile; this is a difference between the foam and a liquid drop, which has a uniform curvature (Eq. [5.1]).

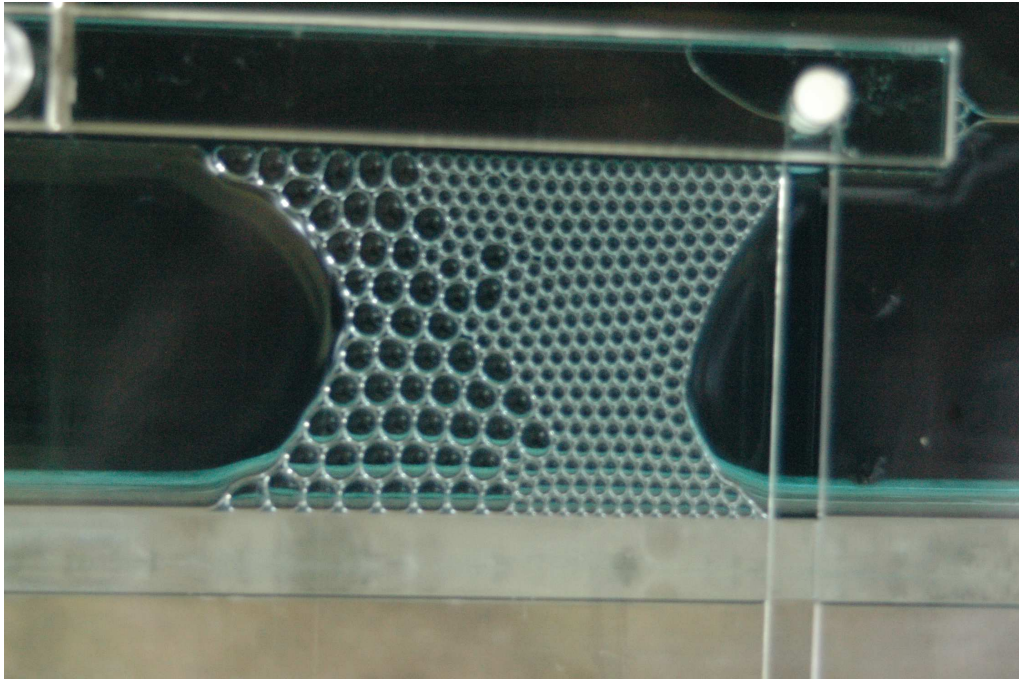
If one compresses a foam a little, the bubbles are only deformed: the foam's behaviour is elastic. If one compresses more, the bubbles start to rearrange; one has applied enough energy for the bubbles to overcome the energy barrier $\Delta\mathcal{E}_{T1}$ associated to rearrangements (see Figure 1.11). Raufaste et al. (2007) show that facilitating rearrangements, which we can interpret as decreasing $\Delta\mathcal{E}_{T1}$, by increasing the water/air ratio in the foam, diminishes the force that a flowing foams exerts on an obstacle.

Indeed, the foams in Figure 5.3b and c have a lower water/air ratio than the one in Figure 5.3a, and the bubbles are more deformed. The direction of elongation of the bubbles differs between compression (Figure 5.3b: the bubbles have a horizontal orientation) and stretch (Figure 5.3c: the bubbles have a vertical orientation). Any deformed bubble produces a force that counteracts the compression or stretch of the foam. If the barrier $\Delta\mathcal{E}_{T1}$ is high, the bubbles deform more before rearranging, and thus store more elastic stress. This stress contributes to the force that is exerted on the plates that compress the foam.

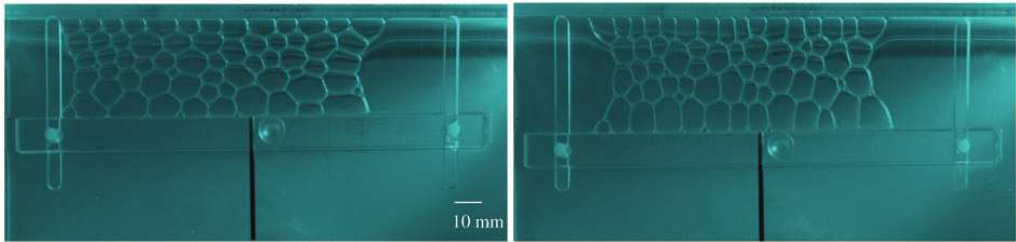
5.1.3 Time scales

The question whether or not cells in aggregates store non-released stress was studied by Phillips et al. (1977); Phillips and Steinberg (1978). They fixed aggregates before and at different times during centrifugation and performed electron micrography of these aggregates (Figure 5.4), to observe the shape of individual cells. After centrifugation starts, cells first flatten (Figure 5.4b), and at the long term become isotropic in shape again; after 35 hours of centrifugation, the cells are relaxed (Figure 5.4c). At sufficiently long timescales, these aggregates thus behave as liquids, and the shape of centrifuged aggregates is entirely determined by the balance between surface-tension-driven rounding and the centrifugal force.

5. AGGREGATE COMPRESSION

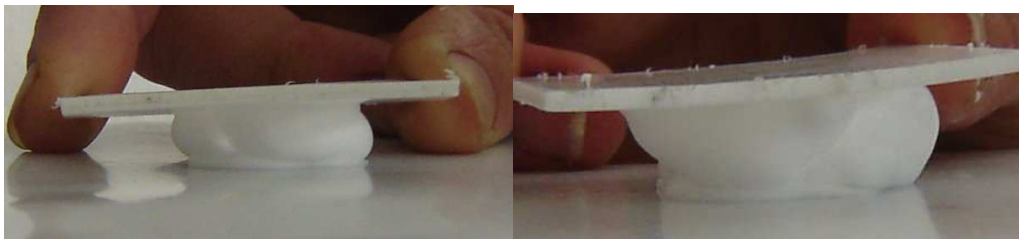


(a)



(b)

(c)



(d)

(e)

Figure 5.3: Compression (a,b,d,e) and stretching (c) of foams. (a-c) soap bubble monolayers confined between two movable plastic plates, and (d,e) shaving foam between two Teflon interfaces. (a) experiments by M.F. Vaz, (b) and (c) reprinted with permission from Vaz (2008), (d) and (e) experiments by C. Quilliet.

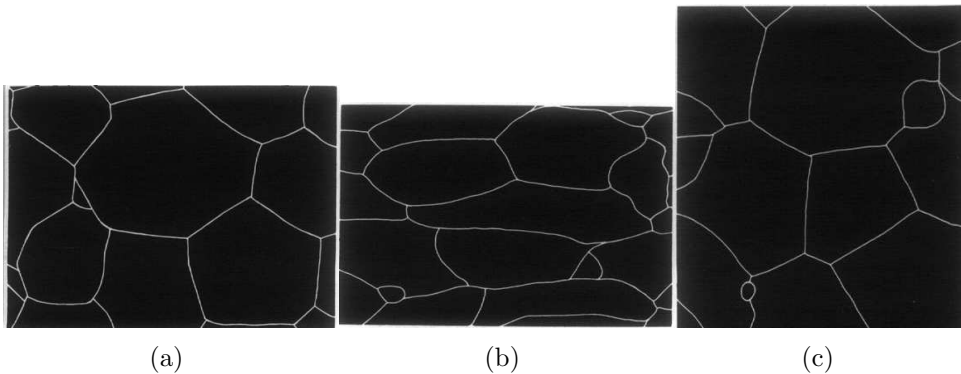


Figure 5.4: Cell perimeters traced from electron micrographs of cross-sectioned fixed aggregates before (a), after five minutes (b) and after 35 hours (c) of centrifugation. The width of each drawing corresponds to 15 to 20 μm . Reprinted with permission from Phillips et al. (1977).

However, the timescales at which Phillips et al. (1977) observed their aggregates, the rounding up of an aggregate, the fusion of aggregates (Schötz et al., 2008; Jakab et al., 2008) or cell sorting (e.g. Chapter 4, Duguay et al., 2003; Beysens et al., 2000) are of 1 to 3 days. For the assessment of surface tension, the time between two successive compression is much shorter, varying from 30 minutes to 2 hours (Foty et al., 1994; Jakab et al., 2008). Forgacs et al. (1998); Beysens et al. (2000) and Jakab et al. (2008) show that an equilibrium force seems to be attained 2 to 10 minutes after compression. Is a tissue that behaves as a liquid on the timescale of a day also doing so at a timescale of several minutes?

5.1.4 This chapter

The response of an aggregate of biological cells to a deformation is not simple: Phillips et al. (1977); Phillips and Steinberg (1978); Forgacs et al. (1998) describe it as visco-elastic. As we have seen in Section 1.3.2 and Chapter 3, on a collective level, tissues (and aggregates) share characteristics with foams: they consist of deformable units that can rearrange, and contain liquid. Their behaviours might be comparable: visco-elasto-plastic (Section 5.1.2).

However, there are many important differences between cells and bubbles (cf Chapter 3). Notably, for cell sorting to occur, active fluctuations of the cells are necessary (Glazier and Graner, 1993; Graner, 1993), while bubbles are inert on short timescales. It is thus not useful to directly ap-

ply the physics of foams to aggregates. Instead, we use some of the tools from foam physics to obtain a distinctive description of the mechanics of aggregates.

CPM simulations have been used in cases where the foam-like packing of cells is important (e.g. Chapter 3) as well as for liquid-like behaviour (as cell sorting, e.g. Chapter 4). We use it here as a tool to study how the visco-elasto-plastic behaviour of an aggregate depends on the biological cellular properties.

We show that the interfacial tension and fluctuations of cells determine whether the aggregate behaves as a liquid, or not. When it does not, we study both the effects at equilibrium and during the dynamics of relaxation. We determine qualitative links between cell-level and collective characteristics.

This opens a perspective to a quantitative study, which goal is to infer cellular properties from aggregate measurements. Up to now, the study of aggregates has been confined to those that behave as liquids, other types of behaviour were neglected or discarded. We expect many aggregates not to behave as liquids; the methods presented here are meant to extract useful information from their behaviour.

5.2 Methods

In simulations, we either compress a liquid drop (for validation purposes, Section 5.2.6), which corresponds to one large CPM cell with a fixed surface tension, or an aggregate of cells that are modelled either with the ‘constant tension model’, Eq. [3.1], or the ‘variable tension model’, Eq. [3.2]. All simulations presented in this chapter are 2D; this allows to run a large number of simulations and explore qualitatively the effect of the parameters. In order to compare the simulations quantitatively to experiments, 3D simulations are more suitable. They are currently being developed; the first tests show that the same methods are applicable.

5.2.1 Compression and forces

Drops or cell aggregates are confined between two plates. Each plate’s zero-energy vertical position z_0 can be changed. The potential energy of the plate interface is

$$\mathcal{E}_C = \frac{1}{2}k (\langle z \rangle - z_0)^2, \quad (5.4)$$

where $\langle z \rangle$ is the averaged vertical position of the plate interface, and k the stiffness of the plate. From this potential energy, the force F on the plate can be defined and measured as:

$$F = k |\langle z \rangle - z_0| . \quad (5.5)$$

We choose it to be positive when the aggregate pushes against the plate.

Some care is required in dealing with a discrete lattice. We define the position z as the average of the positions i and $i + 1$ of two adjacent pixels, where one pixel is of state ‘plate’. Therefore, z always has a value of an integer number plus 0.5. Equally, z_0 is situated between two pixels.

The methods to determine the surface tension rely on the correct estimation of the pressure and force. For this reason, k and λ_A (Eq. [3.1] or Eq. [3.2]) have to be optimised: for high values, the plates or the cells, respectively, are too rigid to allow a statistically reliable measurement; for low values, they deform too much. Indeed, in simulations as well as in experiments in general, the stiffness of the measuring device should always be adapted to the one of the object to measure.

5.2.2 Aggregate shape

The shape of the aggregate is quantified by the descriptive variables R_1 , R_2 and R_3 and θ (Figure 5.1). In 2D, there is only one radius of curvature, which is R_2 ; the contact length between the plate and the aggregate is $2R_3$, and the length halfway between the plates is $2R_1$. R_1 and R_3 are measured as straight horizontal lines.

R_2 is obtained by fitting a parabola to the aggregate profile (we have tried to fit circular arcs and fourth-order polynomials, but both suffer too much from fluctuations in the aggregate profile). From this polynomial $y = a + bx + cx^2$ we take the second derivative as an estimate for the curvature: $1/R_2 = \kappa = |2c|$. The sign of the curvature is determined separately: convex aggregates have a positive curvature, concave aggregates a negative one.

The contact angle θ is estimated by the fit of a straight line (least squares fit with perpendicular offsets) to the aggregate profile close to the plate; the angle of this fitted line with a horizontal line is the estimate of θ . It can alternatively be estimated by calculating the angle at which the fitted parabola intersects the plates; this yields estimations similar to those obtained the first method (results not shown), so we only use the first method here.

At each time of measurement, we have one estimate of R_1 , two of R_3 (one at each plate), two of κ (one on each side), and four of θ (one at each

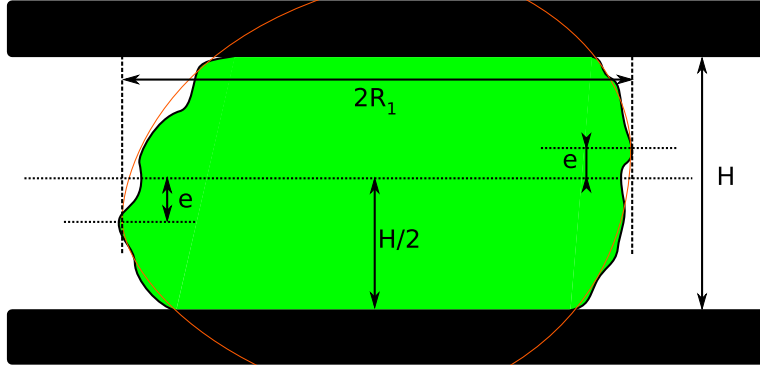


Figure 5.5: Quantification of the deviation of the shape of an aggregate with respect to the sketch in Figure 5.1. The aggregate profiles are depicted by black lines, the fitted profiles by orange lines.

contact point): these are averaged to give one single estimate per shape variable per time of measurement.

We quantify the deviations of the aggregate shape to the shape of a drop by means of the fits to the profiles (Figure 5.5). To quantify small scale deviations, we use the goodness of fit ($r^2 = 1 - SS_{res}/SS_{tot}$, where SS_{res} and SS_{tot} are the residual and total sum of squares). To quantify deviations on a larger scale, note that the cross-section of a liquid drop (Figure 5.1) has two planes of symmetry. We quantify the top-bottom asymmetry by the distance e/H of the extreme of the fitted parabola to the horizontal mid-plate plane ($0 \leq e/H \leq 0.5$). As a measure of the left-right asymmetry of the aggregate, we take the normalised difference of the curvatures, $\Delta\kappa = 2|\kappa_1 - \kappa_2| / (|\kappa_1| + |\kappa_2|)$ ($0 \leq \Delta\kappa \leq 2$; $\Delta\kappa = 2$ if the curvatures are of opposite signs). At each measurement, two profiles are fitted, so we take the average r^2 for the goodness of fit, and the average of e/H for the top-bottom asymmetry.

5.2.3 Surface tension

The surface tension σ of a drop D is equal to the interfacial tension between the drop and the medium M ,

$$\sigma = \gamma_{DM}, \quad (5.6)$$

where γ_{DM} is an input parameter of the constant tension model. In contrast to the previous chapters, for all parameter values listed in this chapter, values corrected by the prefactor 11.3 (see Section 2.3) are given.

The theoretical value of the aggregate surface tension is calculated, as the difference between the cell-medium interfacial tension γ_{CM} and the cell-cell interfacial tension γ_{CC} . We repeat for convenience Eq. [4.5]:

$$\sigma = \gamma_{CM} - \frac{1}{2}\gamma_{CC}. \quad (5.7)$$

In the constant tension model, γ_{CM} and γ_{CC} are directly determined by the input parameters. For the variable tension model, we calculate the interfacial tensions according to Eq. [3.3].

From the interfacial tensions we can also calculate a theoretical contact angle (adapted from Eq. [1.7]),

$$\cos \theta_{th} = \frac{\gamma_{CP} - \gamma_{CC}/2 - \gamma_{MP}}{\gamma_{CC}/2 - \gamma_{CM}}. \quad (5.8)$$

5.2.4 Estimations

Although in 2D, the surface tension σ actually is a line tension, we will nevertheless use the term ‘‘surface tension’’. Its dimensions are energy \times length⁻¹, which is equivalent to force. For simplicity, tension values are given without units.

We adapt Eq. [5.1]-[5.3] to use them in 2D simulations. This yields three methods to estimate the surface tension:

Laplace: We measure the pressure (Π) and curvature (κ) in simulations, and apply a 2D version of Laplace’s law (Eq. [5.1]):

$$\sigma = \frac{\Pi}{\kappa} = \Pi R_2. \quad (5.9)$$

Π is calculated at any time of the simulation through Eq. [2.7] as the average pressure of all cells.

Force balance at $h = H/2$: We measure the force F (as described in Section 5.2.1) and curvature κ , and adapt Eq. [5.3] to 2D:

$$\sigma = \frac{F}{2R_1\kappa - 2}. \quad (5.10)$$

Force balance at $h = 0$: or equivalently, the force balance at $h = H$. We adapt Eq. [5.2] to 2D:

$$\sigma = \frac{F}{2R_3\kappa - 2 \sin \theta}. \quad (5.11)$$

The contact angle θ is measured as described in Section 5.2.2.

The aggregate is compressed progressively. The intervals between two successive compressions should be long enough to allow the aggregate to relax to equilibrium. For surface tension estimations, measurements of all variables in the second half of an interval between compressions are averaged. For the ‘Laplace’ method (Eq. [5.9]), σ is the slope of the straight line fitted to the average values of Π and κ of each compression. For ‘force balance’ methods (Eq. [5.10]-[5.11]), it is the slope of the linear fit to the averages of F and $f(\kappa)$, where $f(\kappa) = 2R_1\kappa - 2$ for the force balance at $h = H/2$, or $f(\kappa) = 2R_3\kappa - 2\sin\theta$ for the balance at $h = 0$, respectively. When error bars are given, these are the standard deviations s of the fit parameters, which are calculated from the standard errors SE and the number of compressions n : $s = SE \times \sqrt{n}$.

5.2.5 Cell shape and spatial behaviour

We use the statistical tools developed by Graner et al. (2008) to quantify the ‘intercellular cell shape’. In short, the cell texture is quantified by the length and direction of the links between centres of neighbouring cells (Figure 5.6a,c). The pattern at each moment is represented as a 2×2 matrix, the texture matrix $\bar{\bar{M}}$ (Aubouy et al., 2003); its two eigenvalues (e_{max}, e_{min}) describe the longest and the shortest axis (Figure 5.6b,d). The anisotropy a of a pattern then is

$$a = 1 - e_{min}/e_{max}, \quad (5.12)$$

with $0 \leq a < 1$, where $a = 0$ for an isotropic pattern. The anisotropy of the cells is a measure for the stored elastic stress (Graner et al., 2008; Marmottant et al., 2008).

Similar tools can be used to describe the changes in the pattern. Disappearance and appearance of links (as in the case of rearrangements) are quantified by the matrix $\bar{\bar{T}}$, which can be represented by its two eigenvalues, a positive and negative one (Figure 5.6e-g). Here, we use the (more robust) cumulative matrix ($\Sigma \bar{\bar{T}}$) to describe the history of rearrangements in the aggregate.

5.2.6 Validations and optimisation

We simulate the compression of a liquid drop, which serves as a reference to compare the aggregate compressions with. A drop (D) is modelled as one cell with constant surface tension; it has the interfacial tensions γ_{DP} and γ_{DM} with the plates (P) and the medium (M). The plates are considered

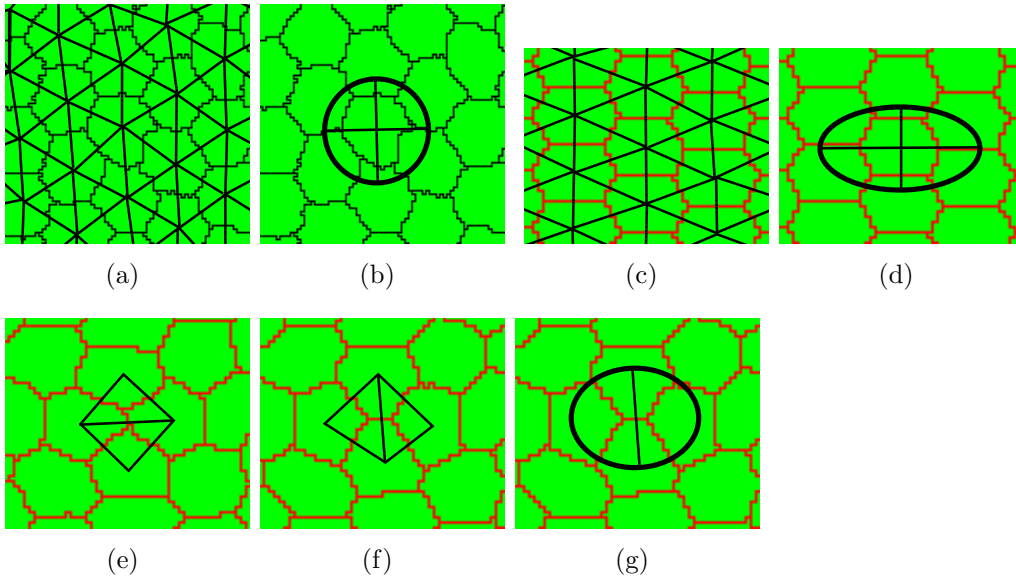


Figure 5.6: Measurement of average cell shape anisotropy and rearrangements. The cell shape is characterised by the links between their centres (a,c) and can be represented as an ellipse (b,d) that has the largest and smallest eigenvalue as axes, and is oriented in the direction of the pattern. In (a-b), the pattern is nearly isotropic, in (c-d) anisotropic. Rearrangements are characterised in a sequence of pictures. A link that was present in (e) has been substituted by another one in (f). The appeared link corresponds to the positive eigenvector (drawn line) in the ellipse in (g), the disappeared link to the negative eigenvector (which is not drawn, by convention).

adhesive when the drop ‘wets’ them; more precisely, when the contact angle θ (Figure 5.1) is smaller than 90° . For a drop, the contact angle is given by the Young-Dupré equation, $\cos \theta_{th} = (\gamma_{MP} - \gamma_{DP}) / \gamma_{DM}$. Figure 5.7 shows two examples of simulations, one with adhesive plates (left), one with non-adhesive plates (right).

Figure 5.8 shows some of the raw data for the simulation of Figure 5.7 (right). The force and the pressure peak immediately after each successive compression, which is a sudden decrease of the distance between the plates. Both force and pressure relax quickly, and plateau at a stable value, showing that an equilibrium has been attained. The contact angle is significantly lower than the expected $\theta_{th} = 180^\circ$, and decreases slightly with compression. In fact, one or two pixels wide wedges get filled by fluctuations (necessary to let the drop relax within a reasonable simulation time), and once the wedge is filled, it is difficult to reopen.

5. AGGREGATE COMPRESSION

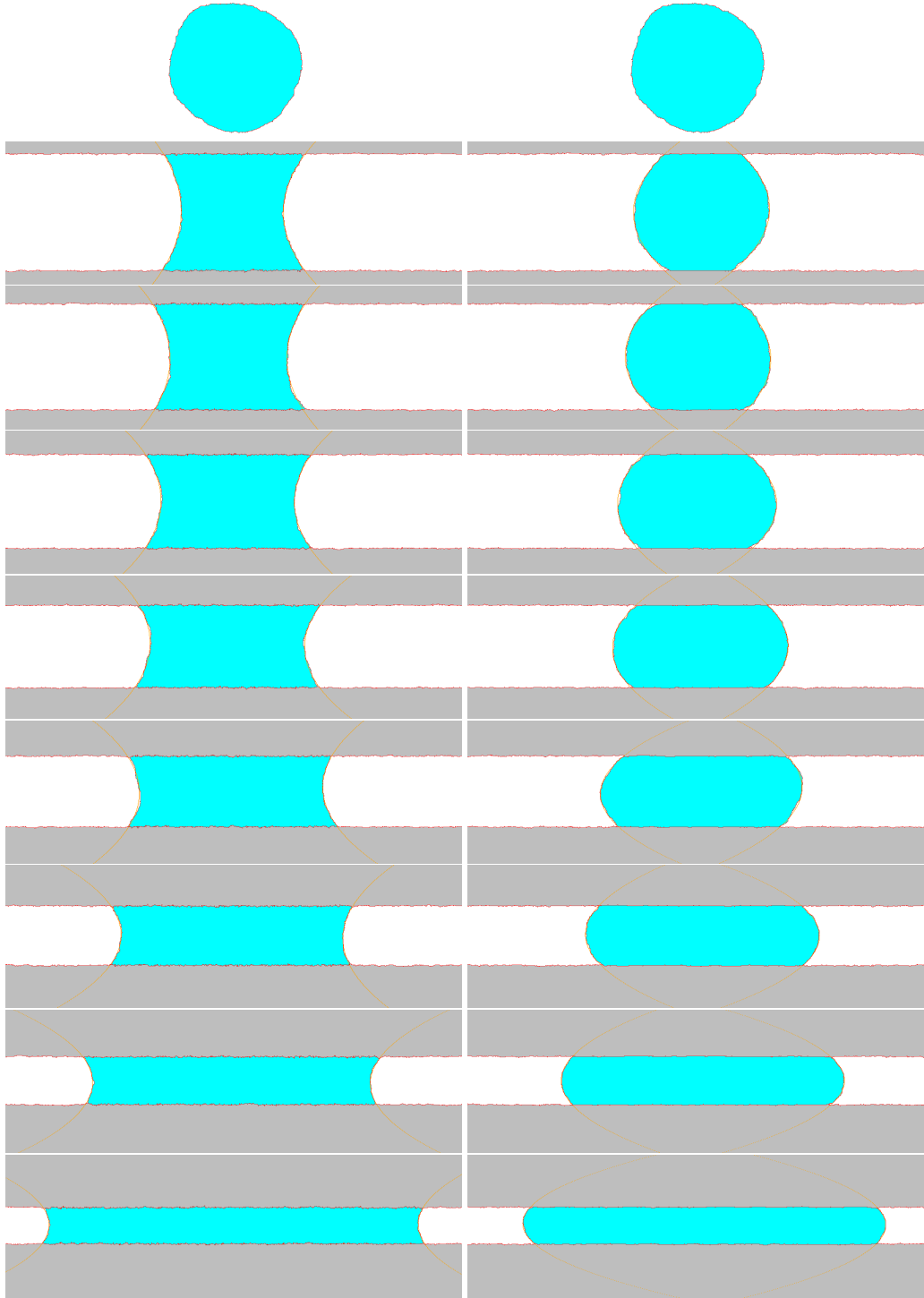


Figure 5.7: Drop compression. Left: adhesive plates, $\gamma_{DP} = 1.13 \times 10^5$, $\gamma_{DM} = 3.39 \times 10^5$, $\gamma_{PM} = 3.39 \times 10^5$, $\lambda_A = 10$, $A_0 = 41000$, $\xi = 7 \times 10^4$, $k = 2 \times 10^4$. Right, non-adhesive plates, $\gamma_{DP} = 6.78 \times 10^5$. Snapshots are taken just before each compression, at 300, 10400, 20400, 30400, 40400, 50400, 60400 and 70400 MCS, and during the last, long compression, at 90400 MCS. Total simulation time is 100000 MCS, on a lattice of 250×800 pixels.

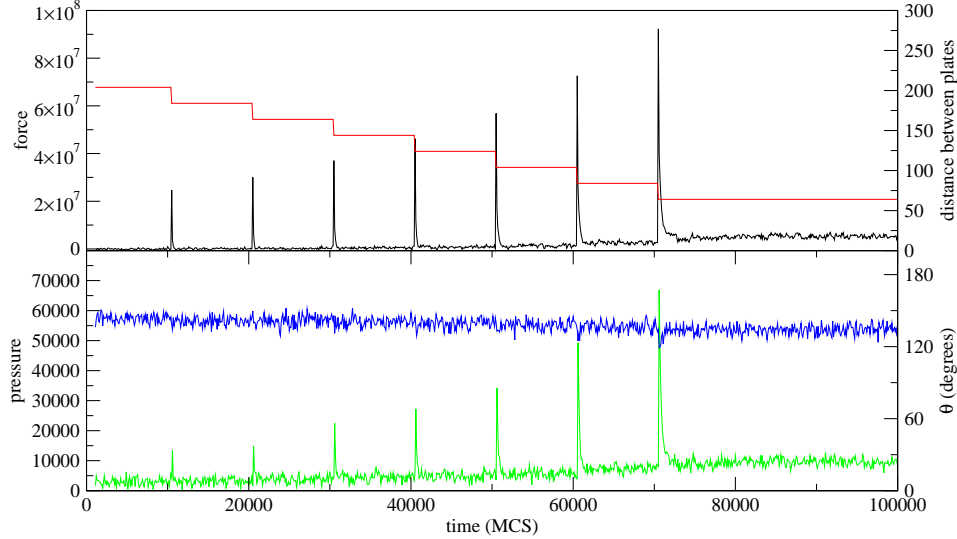


Figure 5.8: The distance between the plates (red) and measurements of the force (black), pressure (green) and the contact angle (blue), during the simulation shown in Figure 5.7 (right). Measurements are made every 100 MCS.

Figure 5.9 illustrates the estimation of the surface tension σ , which is equal to γ_{DM} in the case of a drop. The linear fits yield three comparable values: $\sigma = 2.8 \times 10^5$; this is lower than the input value of γ_{DM} (3.39×10^5). This is due to a systematic bias in the curvature estimation: taking the second derivative of a fitted second order polynomial overestimates the curvature, and thus underestimates the surface tension.

The estimations of the surface tension should be independent of the interfacial tension between the drop and the plate. In the simulations summarised in Figure 5.10, γ_{DP} varies from 1.13×10^5 to 6.78×10^5 , which corresponds to contact angles varying theoretically (Eq. [5.8]) from 48° to 180° . The main difference between the estimations obtained at different values of γ_{DP} are the standard deviations. They attain values comparable to the estimation when θ approaches 90° , where curvature vanishes, at $\gamma_{DP} = 3.39 \times 10^5$ (not presented in Figure 5.10).

Considering that most experiments are done with none-adhesive plates (thus $\theta > 90^\circ$), we choose a value of γ_{DP} that yields a contact angle inter-

5. AGGREGATE COMPRESSION

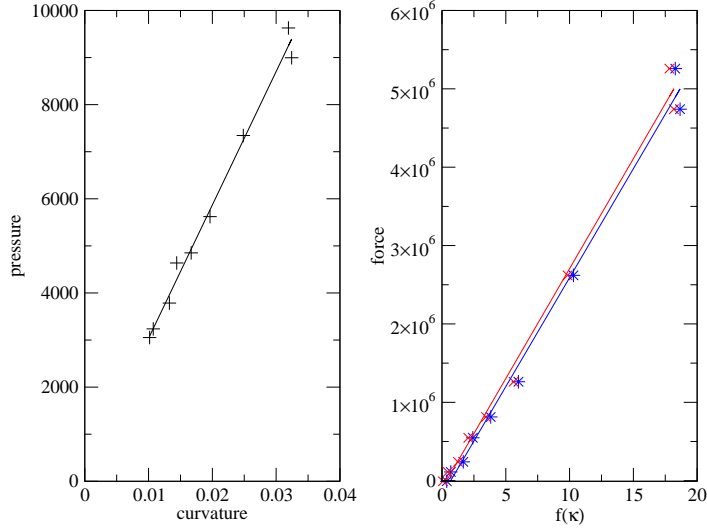


Figure 5.9: Estimation of the surface tension, corresponding to the simulation shown in Figure 5.7 (right). Direct application of Laplace's law (Eq. [5.9], black; linear fit $\Pi = 2.1 \times 10^2 + 2.8 \times 10^5 \kappa$); the force balance at $h = H/2$ (Eq. [5.10], blue; $f(\kappa) = 2R_1\kappa - 2$; linear fit $F = -1.9 \times 10^5 + 2.8 \times 10^5 f(\kappa)$) and the force balance at $h = 0$ (Eq. [5.11], red; $f(\kappa) = 2R_3\kappa - 2 \sin \theta$; linear fit $F = -1.0 \times 10^5 + 2.8 \times 10^5 f(\kappa)$). Data points are averages of the measurements of the second half of each compression interval, except for the last compression, where two averages over equal time intervals are calculated.

mediate between 90° and 180° . This optimises both the accuracy and the robustness of the curvature estimation.

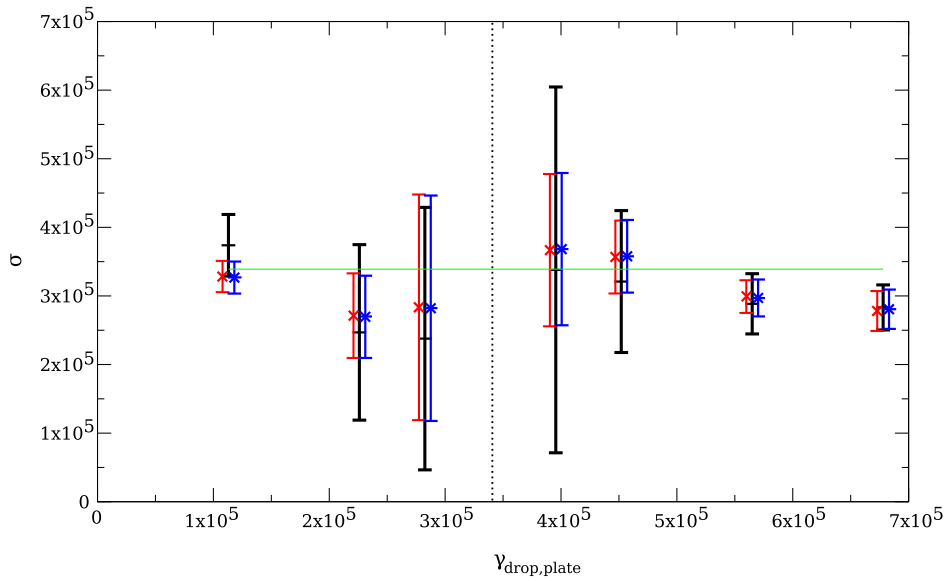


Figure 5.10: Surface tension estimation for different affinities of the drop to the plates. The expected value of the tension σ , 3.39×10^5 , is indicated by the green line. The dotted line indicates the value of γ_{DP} for which $\theta = 90^\circ$. Values obtained from the direct application of Laplace's law are in black, values from the force balance at $h = H/2$ in blue, and from the balance at $h = 0$ in red. The estimations are shown \pm the standard deviation; the symbols representing the three methods are slightly displaced horizontally for lisibility. Parameters as in Figure 5.7, except for γ_{DP} , which is presented on the horizontal axis. At the left, $\gamma_{DP} = 1.13 \times 10^5$, which is the simulation presented left in Figure 5.7; at the right, $\gamma_{DP} = 6.78 \times 10^5$, corresponding to the simulation at the right in Figure 5.7. The corresponding calculated contact angles θ_{th} are (from left to right): 48° , 71° , 80° , 100° , 109° , 132° and 180° .

5.3 Aggregate compression

5.3.1 Liquid behaviour

Figure 5.11 shows the compression of an aggregate, simulated with the constant tension model Eq. [3.1]. As in the drop compression, immediately after each compression, the force and pressure peak, and decrease to an equilibrium value afterwards; the dynamics of attaining the equilibrium will be studied in Section 5.3.5. The expected aggregate surface tension, as determined by the input parameters, is 5.085×10^5 . As Figure 5.12 shows, the three estimation methods are well fitted by straight lines and yield values close to this theoretical value: 5.2×10^5 for the direct application of Laplace's law, and 4.9×10^5 for both methods using the force balance.

The fitted intercept in the application of Laplace's law (e.g. (Figure 5.12, left graph) is linearly dependent on γ_{CC} , and vanishes almost when $\gamma_{CC} = 0$ *. It is the effect of the interfacial tension on the individual cells in an uncompressed aggregate. This is, however, not important for the surface tension estimation of this aggregate.

5.3.2 Cell-cell interfacial tension and fluctuations

Figure 5.13 shows an example of a simulated aggregate with a 6-fold increase of γ_{CC} compared to the aggregate in Figure 5.11. The aggregate-medium interfaces are irregular, and do not look like circular arcs. The value of σ we expect from the parameters is 2.26×10^5 , but the estimations based on the measurements during each compression differ considerably (Figure 5.14): 4.0×10^5 for the direct application of Laplace's law, and 6.6×10^5 and 6.7×10^5 for the application of the force balance at $h = H/2$ and $h = 0$, respectively.

This aggregate does not behave like a fluid where the surface tension determines the shape of the drop as well as the force that it exerts. We now try to describe the shape and the mechanical behaviour of these non-fluid aggregates, in order to find out if they are related, and if we can understand the cellular origin of the behaviour.

The deviation of the mechanical behaviour of the aggregate with respect to a liquid drop, $\sigma_{th} - \sigma_{est}$, is determined in simulations: σ_{th} is calculated from the interfacial tensions (Eq. [5.7]), and σ_{est} is given by the application of Laplace's law or one of the two force balance methods. The estimation

*a linear regression of 18 fitted intercepts and values of γ_{CC} yields: r-squared= 0.996, intercept= -1712, with p-value= 0.0308; slope= 0.08225, with p-value $< 2 \times 10^{-16}$

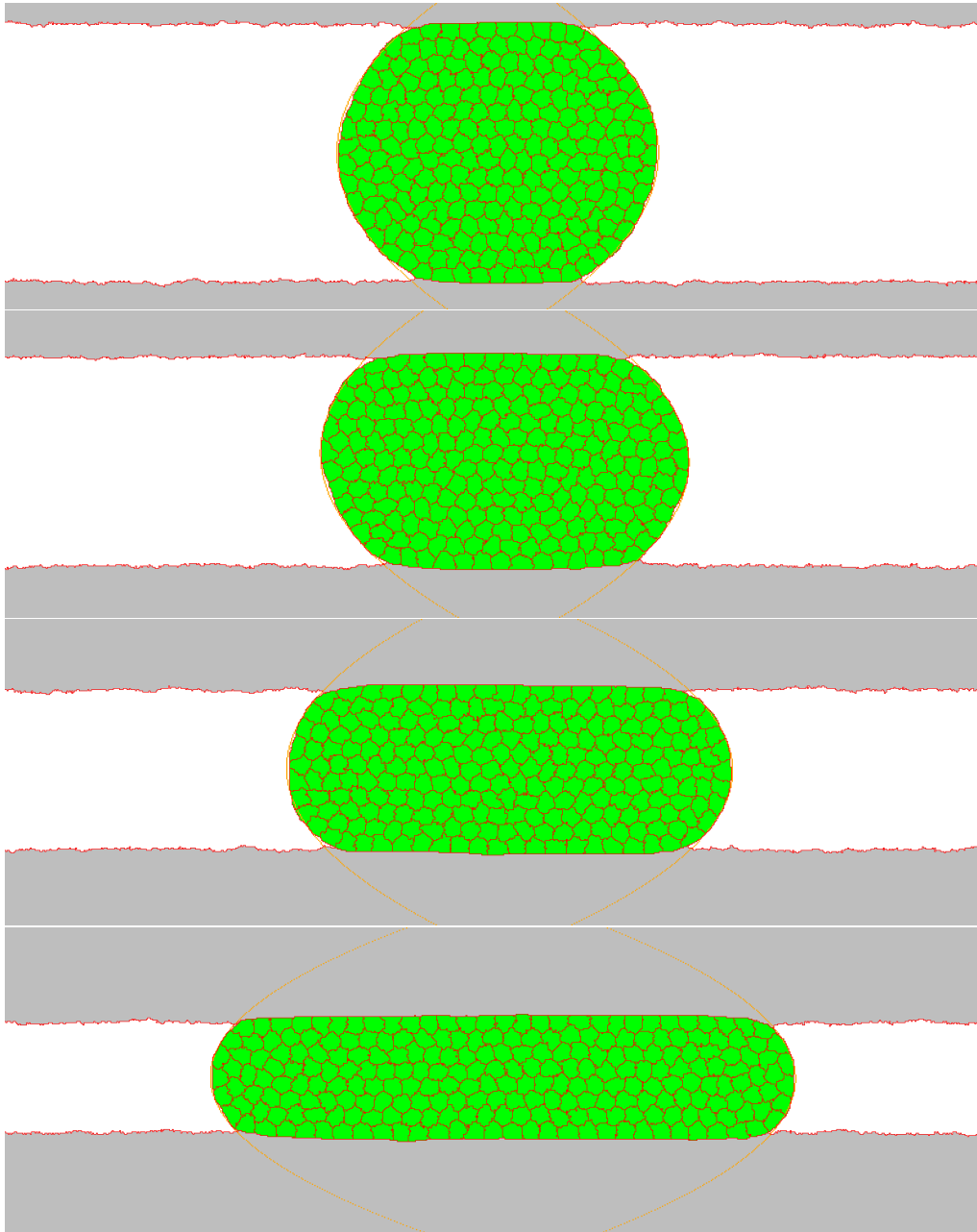


Figure 5.11: Aggregate compression. Parameters are $\gamma_{CC} = 1.13 \times 10^5$, $\gamma_{CM} = 5.65 \times 10^5$, $\gamma_{CP} = 6.78 \times 10^5$, $\gamma_{MP} = 1.13 \times 10^5$, $\lambda_A = 1.0 \times 10^3$, $A_0 = 200$, $\xi = 4 \times 10^4$, $k = 2 \times 10^3$. The total simulation time is 10^6 MCS; the lattice size is 250×800 pixels, with 240 cells. Snapshots are shown at 101500, 301500, 501500 and 951500 MCS; the first three are taken just before a compression.

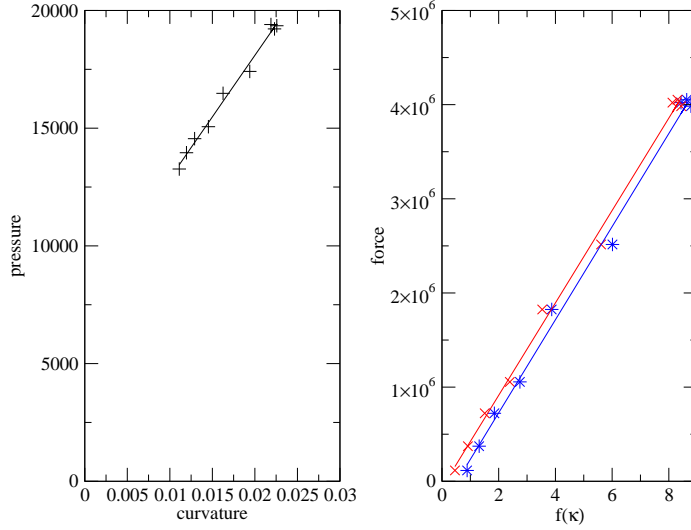


Figure 5.12: Estimation of the surface tension, corresponding to the simulation shown in Figure 5.11. Direct application of Laplace's law (black; linear fit $\Pi = 7.6 \times 10^3 + 5.2 \times 10^5 \kappa$); the force balance at $h = H/2$ (blue; linear fit $F = -2.6 \times 10^5 + 4.9 \times 10^5 f(\kappa)$) and the force balance at $h = 0$ (red; linear fit $F = -7.0 \times 10^4 + 4.9 \times 10^5 f(\kappa)$).

methods themselves yield indices for their validity: the standard deviation of the fitted slope, useful for all estimation methods, and the value of the fitted intercept, only for the force balance methods (as mentioned in Section 5.3.1, the fitted intercept for the Laplace method is determined by the pressure in non-compressed cells).

We performed a series of simulations where γ_{CC} varies from 1.13×10^5 (as in Figure 5.11) to 11.07×10^5 . Some examples are shown in Figure 5.15. The irregularity of the shape increases with the cell-cell interfacial tension. More quantitatively (Figure 5.16), the difference between the estimated and calculated surface tension increases, as do the descriptors of non-fluid mechanical behaviour (intercept of the fit used to determine the tension, and the standard deviation of the estimated tension, upper right graph). Both the left-right and top-bottom asymmetries increase, while the goodness of fit of the profile decreases (Figure 5.16, lower graphs). The cell shape anisotropy increases almost linearly with γ_{CC} (Figure 5.16, bottom right). The anisotropy reflects the amount of elastic stress stored in

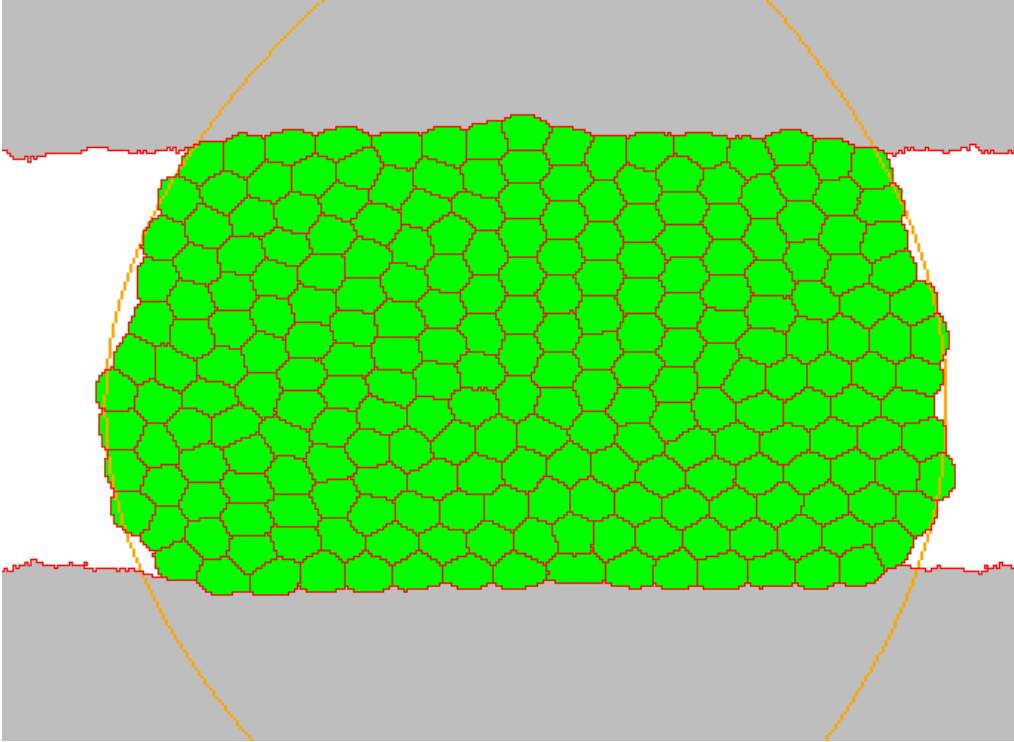


Figure 5.13: A compressed aggregate with a higher interfacial tension between cells, $\gamma_{CC} = 6.78 \times 10^5$. Other parameters as in Figure 5.11. The orange lines are the polynomials that are fitted through both aggregate-medium interfaces.

cell deformations; this explains the difference between the estimated and calculated tension.

Diminishing the fluctuation allowance ξ (Eq. [2.3]) has the same effect as increasing γ_{CC} (results not shown).

5.3.3 Cell-medium interfacial tension

We now change the interfacial tension between the cells and the medium, γ_{CM} , while leaving γ_{CC} constant. To obtain the results shown in Figure 5.17, γ_{CC} is fixed at 5.65×10^5 , an intermediate value for which the aggregate behaviour and shape are moderately but significantly different from the behaviour and shape of a liquid drop (cf Figure 5.16). Variation of γ_{CM} does not influence the correctness of the surface tension estimations: the difference between the estimations and the calculated value stays moderate but significant over the whole range of values tested (Figure 5.17, upper

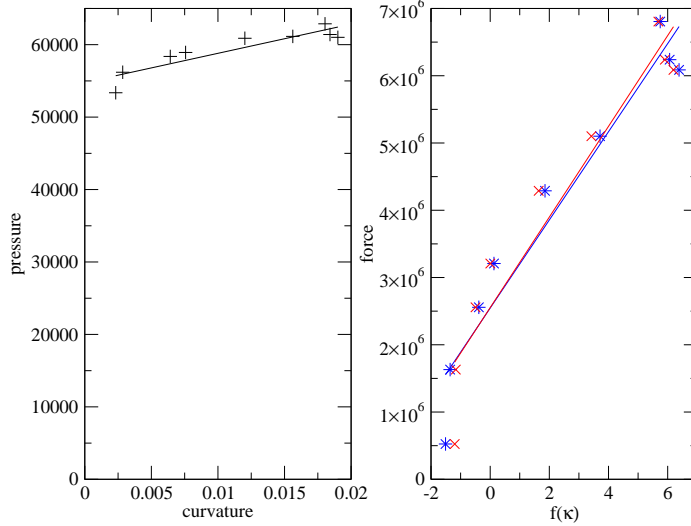


Figure 5.14: Estimation of the surface tension of the aggregate shown in Figure 5.13. Direct application of Laplace's law (black; linear fit $\Pi = 5.5 \times 10^4 + 4.0 \times 10^5 \kappa$); the force balance at $h = H/2$ (blue; linear fit $F = 2.5 \times 10^6 + 6.6 \times 10^5 f(\kappa)$) and the force balance at $h = 0$ (red; linear fit $F = 2.5 \times 10^6 + 6.7 \times 10^5 f(\kappa)$).

left). The intercept and standard deviation increase with γ_{CM} , but increase less than for γ_{CC} (compare Figure 5.17 and 5.16, upper right graphs).

More importantly, the shape of the aggregate resembles more the shape of a drop when γ_{CM} increases: both the aggregate and the profile asymmetry decrease, and the goodness of fit increases (Figure 5.17, lower graphs). The cell shape anisotropy, and thus the stored elastic stress, is hardly influenced (Figure 5.17, lower right). This offers an explanation for the approximately constant difference between σ_{est} and σ_{th} (Figure 5.17, upper left).

5.3.4 Variable tension model

We test whether we obtain different results with the variable tension model (Eq. [3.2]). Figure 5.18 shows the results of increasing the perimeter modulus λ_P in comparison with the results obtained with the constant tension model (Figure 5.16). As λ_P is not interface specific, the calculated aggregate surface tension (based on the interfacial tensions calculated with

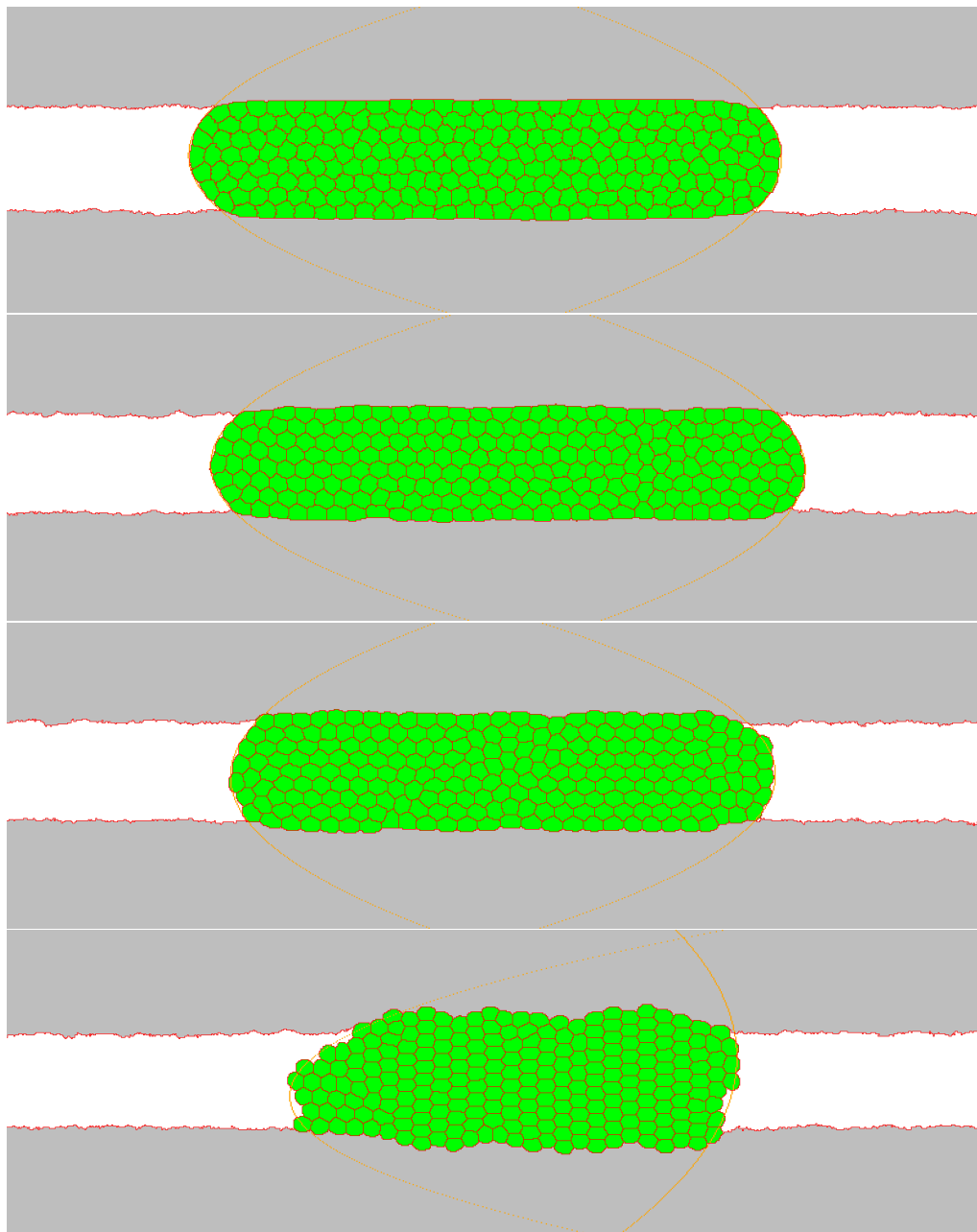


Figure 5.15: Compressed aggregates with different values of γ_{CC} : 2.26×10^5 , 4.52×10^5 , 6.78×10^5 and 11.07×10^5 respectively. Other parameters as in Figure 5.11. Snapshots are taken at the end of the simulations, after 10^6 MCS.

5. AGGREGATE COMPRESSION

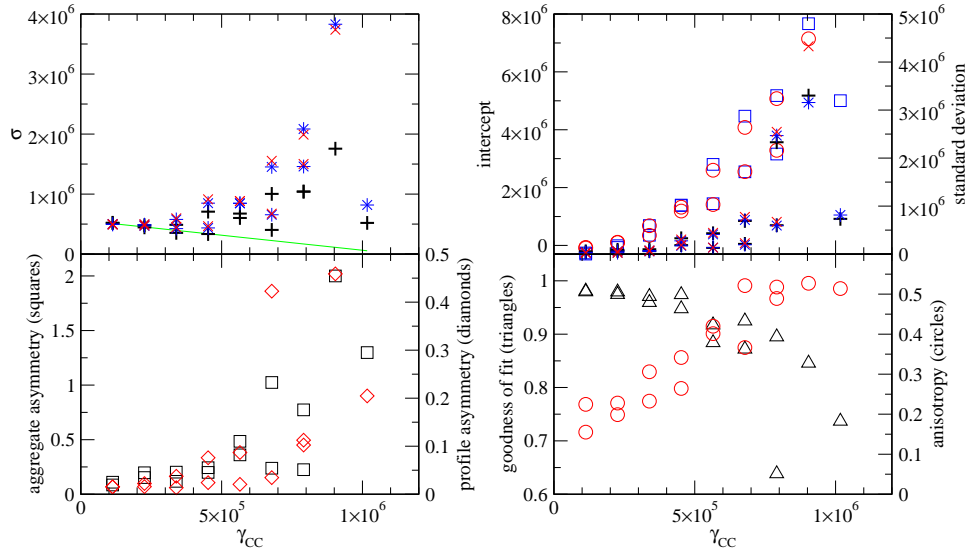


Figure 5.16: Effect of cell-cell interfacial tension (γ_{CC}). Upper left: the surface tension σ calculated from the parameters (green line) compared to the values obtained with the different estimation methods (Laplace: +; force balance at $H/2$: *; force balance at $h = 0$: x). Upper right: the intercept and standard deviations of the slope of the fitted lines used to estimate the surface tension. Intercepts: force balance at $H/2$, blue squares; force balance at $h = 0$, red circles. Standard deviations: same symbols as upper left graph. Lower left: aggregate asymmetry ($\Delta\kappa$, black squares) and profile asymmetry (e/H , red diamonds). Lower right: goodness of fit (r^2 , black triangles) and anisotropy (a , Eq. [5.12], red circles). 18 simulations were performed with the parameters mentioned in Figure 5.11, while varying γ_{CC} , with two simulations per value of γ_{CC} . One of the two simulations with $\gamma_{CC} = 9.04 \times 10^5$ and one with $\gamma_{CC} = 11.07 \times 10^5$ did not allow sensible measurements and were discarded; the other simulation with $\gamma_{CC} = 11.07 \times 10^5$ had numerical problems in the estimation of the contact angle, so the method using the force balance at $h = 0$ could not be used. Values used for the lower graphs are the averages of the measurements during the last compression.

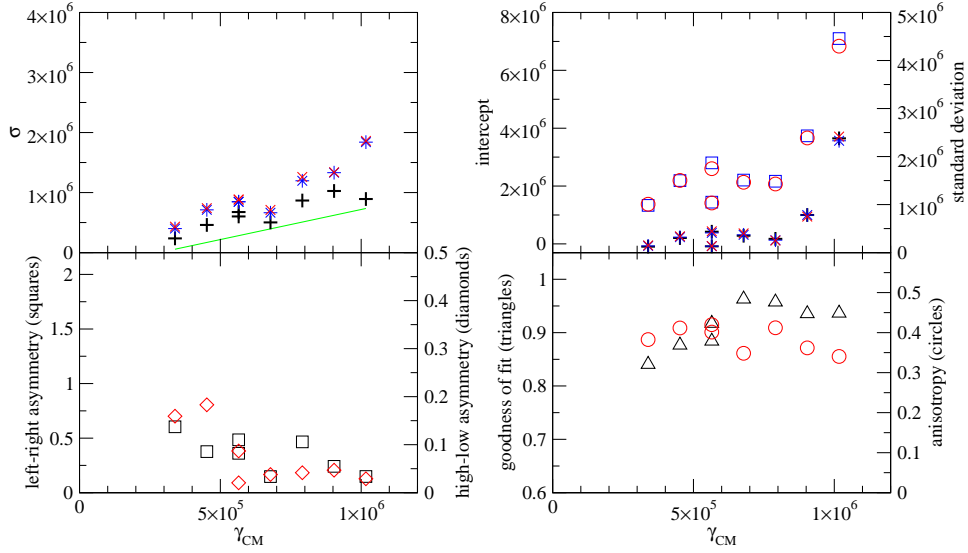


Figure 5.17: The effect of the cell-medium interfacial tension, γ_{CM} , on the mechanical behaviour and the shape of the aggregate. Axes, scales, symbols and colour coding are the same as in Figure 5.16, but note that the horizontal axes now present γ_{CM} . Parameters are as in Figure 5.11, except that $\gamma_{CC} = 5.65 \times 10^5$, and γ_{CP} varies with γ_{CM} , so that $\gamma_{CP} = \gamma_{CM} + 1.13 \times 10^5$.

Eq. [3.3]) stays constant, whereas the estimated surface tension increases with increasing λ_P . All interfacial tensions increase with λ_P , thus making rearrangements more difficult, and increasing the cellular anisotropy.

However, the deviations from liquid behaviour at high values of γ_{CC} are lower in the variable tension model simulations than in those with the constant tension model, which is explained by the difference of σ_{est} between the constant and variable tension models. This difference influences the shape (Figure 5.18 bottom) but not the anisotropy (bottom right), as already found when studying the effect of γ_{CM} . The increase of λ_P in the variable tension model is thus equivalent to an increase of both γ_{CC} and γ_{CM} in the constant tension model.

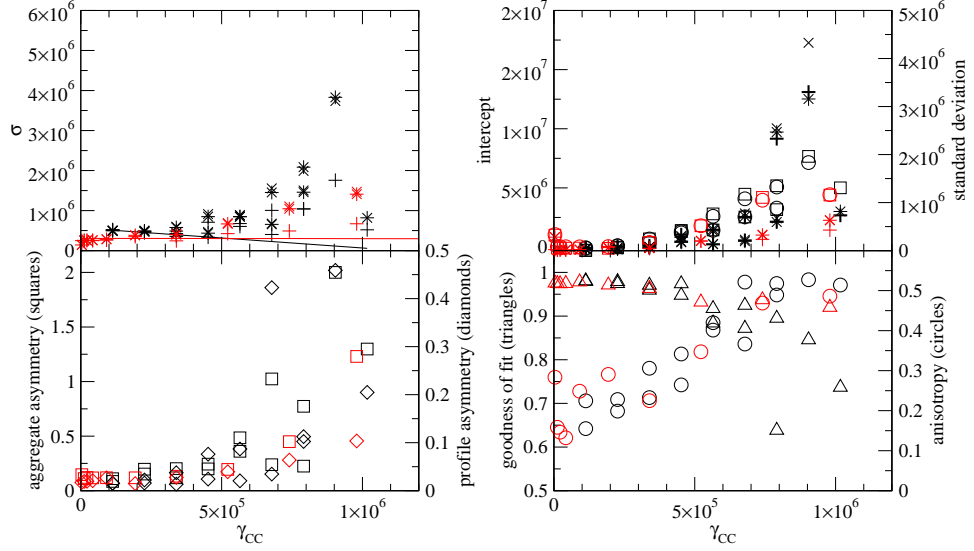


Figure 5.18: Comparison of the results of the variable tension model with the results of the constant tension model, presented in Figure 5.16. Symbols are as in Figure 5.16, but the colour code now represents the models: black for the constant tension model, red for the variable tension model. Variable tension model parameters are $\xi = 4 \times 10^4$, $\lambda_A = 10^3$, $A_0 = 200$, $P_0 = 0.7 \times (11.3 \times 2\sqrt{\pi A_0 C})$, $J_{CC} = 6.1 \times 10^5$, $J_{CP} = J_{MP} = -1.13 \times 10^5$, $J_{CM} = 0$, and λ_P varies from 10 to 316.

5.3.5 Relaxation towards equilibrium

Non-liquid behaviour is the effect of non-relaxed stress, stored in elastic deformations. If we wait long enough, would this stress disappear? We test this hypothesis, and find that it is not the case. In the upper graph of Figure 5.19, two curves of the relaxation of the compressive force are shown: one representing a liquid-like aggregate (black line; surface tension estimations shown in Figure 5.12), the other an aggregate that does not behave as a liquid (red line; for surface tension estimations, see Figure 5.14). For both aggregates, a stable force is reached at the end.

The cell shape anisotropy a in both simulations also reaches a stable value (Figure 5.19, middle graph). The lower graph shows the cumulative cellular rearrangements, which are presented as the eigenvalues of the matrix made of the sum of all rearrangements, $\sum \bar{T}$. After each compression,

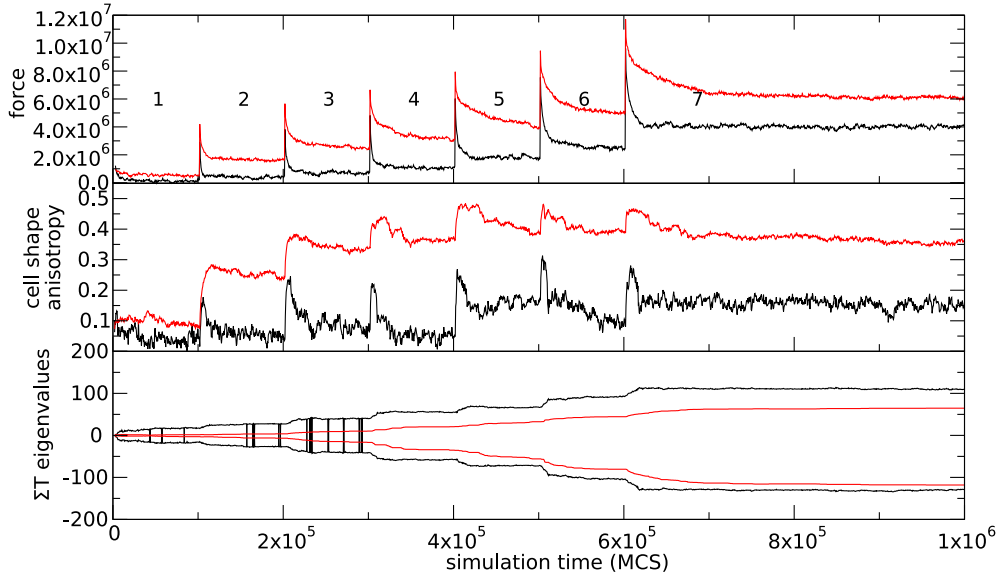


Figure 5.19: Dynamics of the force measured on the plates (upper graph) and the shape (middle graph) and spatial behaviour (lower graph) of cells during simulations of aggregate compression. Black: aggregate corresponding to Figure 5.11; red: aggregate corresponding to Figure 5.13. The compression intervals are numbered in the upper graph.

in both simulations shown, the absolute values of the eigenvalues increase, and reach a plateau. A stable value of the eigenvalues either indicates no rearrangements, or random rearrangements; an increase represents dissipation of elastic stress. Thus, after each compression, stress is released because cells intercalate, and the cell shape anisotropy decreases. However, the equilibrium value of the cell shape anisotropy increases with the degree of compression, indicating that the rearrangements are not sufficient to release all stored stress. The plateau force at the end of the simulation is thus a stable one.

P. Marmottant (pers. comm.) proposes to model the stress relaxation in an aggregate analytically. If cells were inert, they would behave like a foam, and stresses below the yield stress would not be released. However, in the absence of external stress, the fluctuations of cells provide a way to overcome the energy barrier ($\Delta\mathcal{E}_{T1}$) associated to rearrangements (Figure 5.20B; see further Section 1.2.3.2 and Figure 1.11; Graner, 1993; Beysens et al., 2000). In an aggregate, not all energy barriers are the same; in practice, $\Delta\mathcal{E}_{T1}$ represents a distribution of energy barriers.

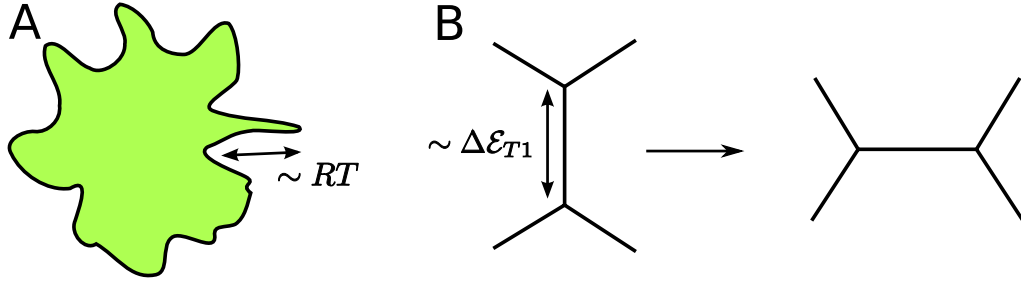


Figure 5.20: Cellular origin of the parameters in Eq. [5.13]. **A**: Membrane fluctuations are described by the temperature analog RT . **B**: The energy barrier for a rearrangement to occur, $\Delta\mathcal{E}_{T1}$, is related to the interfaces, and thus to their tension and length.

These barriers are compared to the energy of cell fluctuations, which we call RT in analogy with molecular thermodynamics (Figure 5.20A). If $RT \gg \Delta\mathcal{E}_{T1}$, the cells' fluctuations can easily overcome all energy barriers, and the aggregate's behaviour is liquid-like; if $RT \ll \Delta\mathcal{E}_{T1}$, it is solid-like. Increasing T , which is analogous to a temperature, increases the facility to rearrange.

Applying a stress to the aggregate changes the probability to rearrange: it increases the probability of stress-releasing rearrangements, and decreases the probability of stress-enhancing rearrangements. In an adaptation of Eyring's model (Eyring, 1935), both contributions to the rate of rearrangements (the applied external stress and the fluctuations) are incorporated in a constitutive model of the mechanical behaviour of the aggregate (Marrontant et al., in prep).

A sudden compression of an aggregate is a sudden application of a stress. The elastic stress in the aggregate increases to a peak value τ_0 , then decays as

$$\tau = 2\tau^* \tanh^{-1} \left[\tanh \left(\frac{\tau_0}{2\tau^*} \right) \exp \left(-\frac{t}{t_c} \right) \right]. \quad (5.13)$$

t is the time, and t_c the time over which stress disappears, which depends on the ratio of the average energy barrier and the fluctuation energy:

$$t_c \sim \exp \left(\frac{\Delta\mathcal{E}_{T1}}{RT} \right). \quad (5.14)$$

τ^* is a characteristic stress, that describes the ease with which fluctuations can overcome energy barriers in the absence of external stress:

$$\tau^* = \frac{RT}{V}, \quad (5.15)$$

where V is of the order of the volume of a cell. If we wait infinitely long, all stresses disappear.

If the applied stress is higher than the characteristic stress ($\tau_0 > \tau^*$), τ decreases faster than exponential. This relaxation has an infinity of characteristic times: this time increases during the relaxation (instead of using a model with two times, cf Forgacs et al., 1998).

We can adapt Eq. [5.13] to describe the force exerted on the plates while compressing an aggregate. The simulated aggregates are 2D, so the force on a plate is

$$\begin{aligned} F &= 2R_3(\tau + \tau_p) \\ &= 2R_3\left(2\tau^* \tanh^{-1}\left[\tanh\left(\frac{\tau_s}{2\tau^*}\right)\exp\left(-\frac{t-t_0}{t_c}\right)\right] + \tau_p\right). \end{aligned} \quad (5.16)$$

Immediately after compression, at $t = t_0$, $F = 2R_3\tau_s$, where τ_s is the sum of τ_0 (the stored elastic stress at $t = t_0$) and τ_p ($\tau_s = \tau_0 + \tau_p$). During relaxation, the force decreases to $2R_3\tau_p$, where τ_p is the stress at the plateau value of the force; it incorporates the effect of the surface tension, as well as any non-relaxed stress.

We fit the force relaxation curves shown in Figure 5.19 with this model. R_3 is measured during the simulation, τ_s is calculated from the force measured directly after the compression, at time $t = t_0$: $\tau_s = F_0/(2R_3)$.

If we suppose that all interior stresses disappear, τ_p can be calculated from the distance between the plates and the calculated surface tension. In the simulation with high γ_{CC} (Figure 5.19, red curve), this calculated value of τ_p gives a force ($F_p = 2R_3\tau_p$) which is several times lower than the plateau value of the force in each compression interval. When we try to force the fit to reach this force F_p , the regression does not converge: it is not possible to fit the force relaxation in this simulated value when supposing that all internal stress has disappeared. This agrees with the observation that the average cell shape does not become isotropic (Figure 5.19, middle graph). We explain this by supposing that $RT < \Delta\mathcal{E}_{T1}$: a large part of the energies can not be easily crossed by the fluctuation, leading to a stabilisation of the force before all stress has disappeared.

τ_p is thus left as a parameter of the fit, together with τ^* and t_c . One fit is shown in Figure 5.21, and the results are summarised in Figure 5.22. In both simulations, the fitted value of τ_p increases with the degree of compression: in the liquid-like aggregate, the curvature increases, so the pressure in the aggregate increases as well, while in the non-liquid aggregate the stored elastic stress increases with the degree of compression (Figure 5.19 middle and lower graphs). τ^* stays approximately constant at the same value for

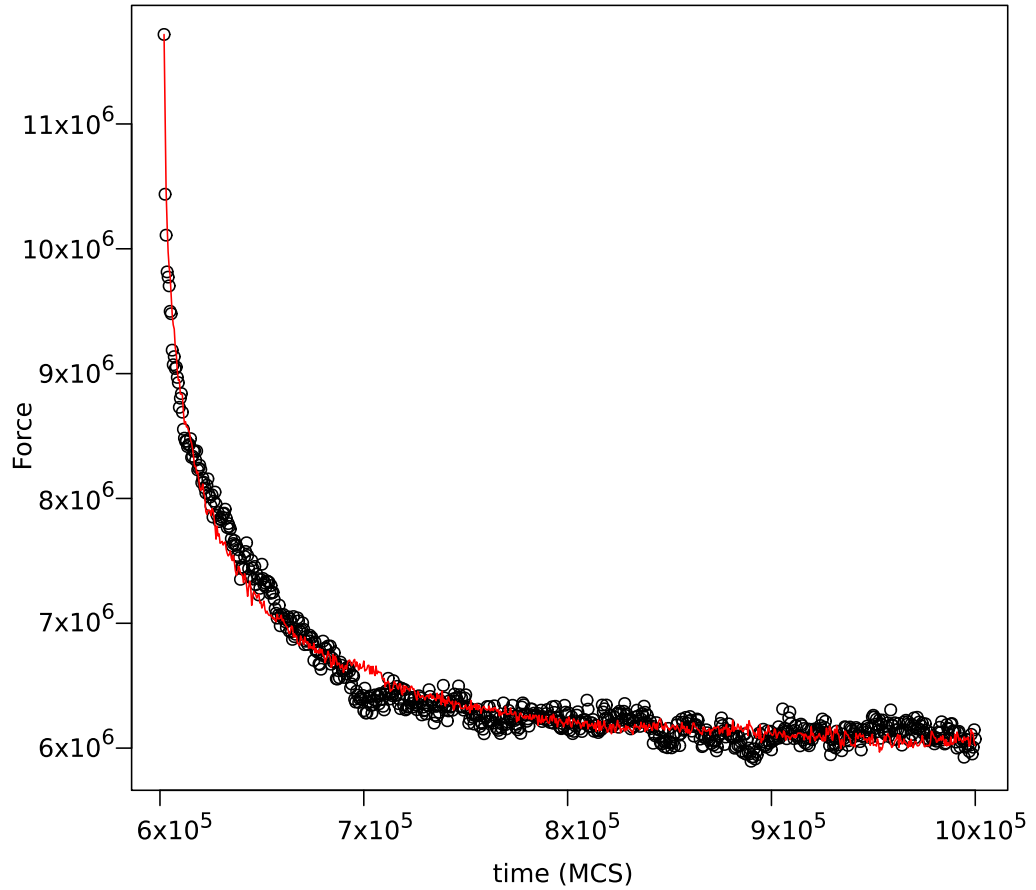


Figure 5.21: Fit of Eq. [5.16] to the force relaxation of the last compression of an aggregate with $\gamma_{CC} = 6.78 \times 10^5$ (Figure 5.19, red). The black circles indicate the simulated force, the red line the fit. The fitted parameters are $\tau^* = 3399$, $\tau_p = 14802$ and $t_c = 64210$, with standard errors being 32, 18 and 1065, respectively. The fitted line fluctuates because of the use of the simulated values of R_3 .

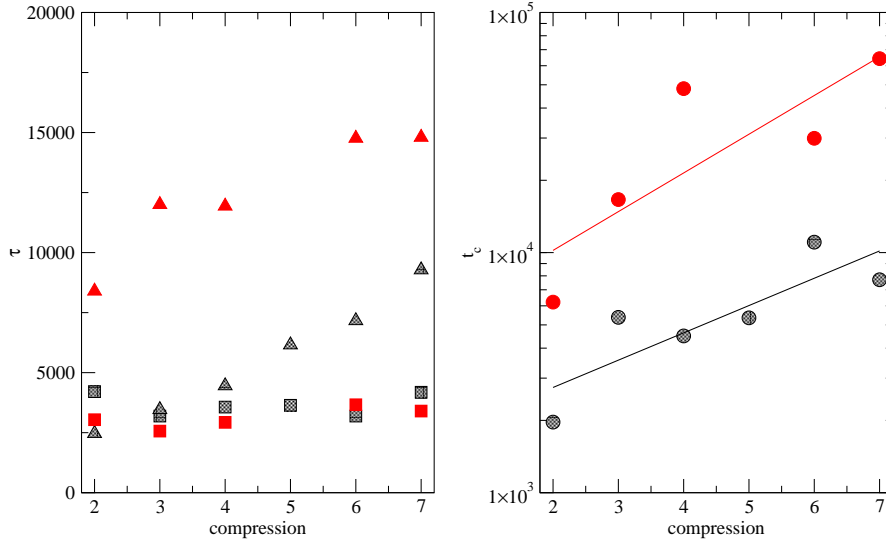


Figure 5.22: Parameters obtained by fits of Eq. [5.16] to the force relaxation curves in Figure 5.19. Colour coding as in Figure 5.19. Squares present the fitted τ^* , triangles τ_p , and circles t_c ; note the logarithmic scale of the vertical axis of the left graph. Fitted lines are drawn to guide the eye. n on the horizontal axes corresponds to the n^{th} compression interval in Figure 5.19; of a total of 7 intervals, the first was discarded. For the aggregate represented in red, the fit of the 5^{th} compression interval did not converge. All fitted parameters have standard errors $< 10\%$ of the estimated value.

both simulations. τ^* depends on the energy of the fluctuations (Eq. [5.15]), which are determined by the parameter ξ in the simulations. This parameter does not change during and between simulations, which corresponds to the fact that the fitted τ^* does not change either.

The difference in the dynamical behaviour of these simulated aggregates is found in the fitted variable t_c . Its value depends on the ratio of the fluctuation energy RT and the average energy barrier $\Delta\mathcal{E}_{T1}$ (Eq. [5.14]). As τ^* does not change, and we concluded before that RT thus did not change, the change in t_c should be due to a change in $\Delta\mathcal{E}_{T1}$. Indeed, γ_{CC} is a tension, which is an energy change associated to a length change; for the simulation with the higher γ_{CC} , we expect $\Delta\mathcal{E}_{T1}$ (Figure 5.20B) and thus t_c to be larger.

t_c increases during both simulations as well. As the compressions provoke rearrangements (Figure 5.19 lower graph), the rearrangements that have a relatively low energy barrier have a higher probability to take place. This increases the average value of $\Delta\mathcal{E}_{T1}$, that determines t_c (Eq. [5.14]).

5.4 Discussion

5.4.1 Liquid and non-liquid behaviour

We simulate the behaviour of an aggregate of cells, and compare this behaviour with the behaviour that is predicted by the popular hypothesis that aggregates behave as liquids do. We indeed find simulation parameters for which the aggregate is sufficiently liquid; in this case, all stress in the aggregate is due to the surface tension, and the tension can thus be quantified easily. Aggregate liquidity means that all bulk stress in the aggregate is dissipated by plastic cell rearrangements.

However, when increasing the cell-cell interfacial tension γ_{CC} , the aggregate reaches a regime in which rearrangements are more difficult. In this regime, the force that the aggregate exerts on the plates is not due to the surface tension alone, but also to non-released elastic stress, stored as cell deformations. Neglecting this elastic stress when estimating the surface tension from force measurements would result in an overestimation of this tension. This overestimation is accompanied by an increase in the standard deviation of the tension estimation, as well as an increase in the asymmetry (high-low, left-right) of the aggregate shape and the roughness of the profile. The cell shape anisotropy, a measure for the stored elastic stress, correlates well with γ_{CC} . We do not detect a difference between the constant and the variable tension model; increasing the cortical cytoskeleton contractility (λ_P) increases γ_{CC} , and the effect is quantitatively indistinguishable from increasing γ_{CC} in the constant tension model.

Increasing the cellular fluctuations, described by the model parameter ξ , has the opposite effect: at high values of ξ , the elastic stress is released more easily, and the aggregate behaviour is more liquid-like. The cell-medium interfacial tension γ_{CM} does only influence the surface of the aggregate: it thus influences the shape, but not the cell shape anisotropy in the bulk of the aggregate. Aggregates can thus appear smooth and constantly curved, while their mechanical behaviour is solid-like; on the other hand, aggregates with a low γ_{CM} can appear rough, yet behave as a liquid if γ_{CC} is low as well.

The dynamics of the aggregate after compression show that both the cell shape anisotropy and the force diminish when rearrangements take place, and an equilibrium of these is reached at the end of the simulations. We fit the force relaxation curves with an analytical model (Marmottant et al., in prep). The extracted parameters are in agreement with the equilibrium behaviour, and this provides a possibility of comparison with experimental data, that we discuss below.

In a liquid, all elastic stresses disappear with time, and its equilibrium behaviour is governed uniquely by the surface tension. A solid is characterised by its elasticity and a threshold to this elasticity; above this threshold, its behaviour is plastic (or it breaks). Aggregates are intermediate between liquids and solids: surface tension acts at the surface, while the bulk properties can vary from liquid to solid-like. For rearrangements, an energy barrier ($\Delta\mathcal{E}_{T1}$) needs to be overcome. When the cell fluctuations are sufficient to overcome this barrier, the aggregate behaves as a liquid; when they are not, the energy barriers act as a threshold, that prevents a certain amount of elastic stress to be dissipated.

The surface tension drives the shape relaxation; the fluctuations drive the elastic stress relaxation, which makes shape relaxation possible. The cell-cell interfacial tension increases $\Delta\mathcal{E}_{T1}$ and impedes stress relaxation; this leads to irregular shapes. Due to the surface tension, the global energy minimum, even for a non-liquid aggregate, would closely resemble the shape of drop; due to the existence of a threshold, the shape that the aggregate takes is more or less random (it depends on the history). It is thus the average deviation from a smooth curved interface that characterises this threshold; the shape deviations should thus be studied statistically.

5.4.2 Biological origin of the parameters

Cell properties, which are the interfacial tensions (γ_{CC} , γ_{CM}) and the fluctuations (described by the parameter ξ) have an influence on the mechanical behaviour of the aggregate. The interfacial tensions are determined by the cortical cytoskeleton (both γ_{CC} and γ_{CM}) and the adhesion (only γ_{CC}), as in Chapter 3 and 4. Indeed, increasing λ_P , that determines the contractility of the cortical cytoskeleton in the variable tension model (Chapter 3), resembles an increase of both γ_{CM} and γ_{CC} in the constant tension model. The effect of adhesion in the model is a decrease of γ_{CC} : this hypothesis seems to be confirmed by the results presented in Chapter 3 and 4.

If the effect of adhesion was merely a decrease in γ_{CC} , it would facilitate rearrangements. Experimentally, the effect of adhesion on the dynamical

behaviour of cells is ill-studied. On the one hand, downregulation of adhesion increases invasiveness of tumour cells (Gumbiner, 2005), and the random motions of *Hydra* cells are smaller in more cohesive aggregates (Rieu et al., 2000), suggesting that adhesion hampers cell movements. On the other hand, in the *Drosophila* oocyte, border cells without E-cadherin do not migrate (Niewiadowska et al., 1999; Geisbrecht and Montell, 2002), and increasing integrin-mediated cell-cell adhesion allows aggregate rounding to occur (Robinson et al., 2003), suggesting a positive effect of adhesion on cell motility.

Several studies have compared thermodynamic fluctuations, described by the parameter ξ in the CPM, to active cell membrane ruffling, that are decreased upon treating the cells with cytochalasin B (Glazier and Graner, 1993; Graner, 1993; Mombach et al., 1995; Beysens et al., 2000) or by cooling them (Mombach and Glazier, 1996). These studies already demonstrated that fluctuations are necessary to overcome the energy barriers associated to the rearrangements that allow cells to diffuse.

The present study suggests a few tests that can be performed experimentally. First, the behaviour of one aggregate which undergoes successive compressions can be studied, and parameters can be extracted using Eq. [5.16]. Second, aggregates can be compared qualitatively by treating them with drugs, or genetically modifying cell properties.

5.4.3 Simulations

The model parameters are scalable, and yield relative values. Some parameters could be studied in more details. E.g., the area modulus λ_A optimises the pressure measurements (see Section 5.2.1), but equally affects the fluctuations. The target area A_0 determines the cell-to-pixel size ratio, which affects the facility of rearrangements (Raufaste et al., 2007); we have chosen a value that allows the exploration of liquid as well as non-liquid behaviour. The difficulty of crossing the energy barrier $\Delta\mathcal{E}_{T1}$ is related to its height and the amplitude and frequency of the fluctuations; γ_{CC} and A_0 determine its height, and ξ and λ_A determine the fluctuations. The determination of the quantitative effect of these parameters will be improved when they can be calibrated to experimental values.

The CPM simulations can describe the dynamics of cell aggregates correctly if these dynamics are quasi-static, *i.e.* if they are a succession of equilibria. At each successive compression, the aggregate is compressed by 10 to 20% (20 pixels), which is equal to 1.5 to 2 cell heights (the diameter of an unstressed cell is ~ 16 pixels), by displacing the energy minimum of the plates. It takes time for the plates to reach this energy minimum, because

the speed of any object in the CPM is limited to 1 pixel per MCS. Furthermore, they are deformed by the cells, which slows down their movement even more. The cells are thus displaced less than 1 pixel per MCS, and are able to stay in, or regain quickly, a local energy minimum (see Section 2.3.2). The force relaxation in the simulations is reasonably well described by the analytical model (Eq. [5.13]).

5.4.4 Perspectives

We model the compression of cell aggregates, and link both the behaviour at equilibrium as the dynamics of relaxation to cell-level parameters. In simulations, we combine ideas that stem from different physical analogies (liquids and foams). In contrast to other quantitative studies (Forgacs et al., 1998), the same cellular properties govern the dynamics and the final state (shape and force). We propose thus to extend the study of aggregates beyond those aggregates that behave like liquids.

When understanding how cell-level properties influence several aspects of the behaviour of the aggregate, it will be possible to perform the inverse analysis: inferring the cellular properties from measurements and pictures of an aggregate. We are currently analysing aggregate compression experiments (A. Mgharbel, H. Delanoë and J.-P. Rieu). We plan to widen this approach to other experiments, like aggregate rounding and fusion, which can also be simulated (J.C.M. Mombach) and studied theoretically (P. Marmottant).

In the following, we briefly indicate how simulation results, theory and experiments can be combined, using the work presented here and related publications. From the analysis of the behaviour at equilibrium in the first part of this chapter, we find that γ_{CC} and ξ determine the amount of non-relaxed stress at the plateau value of the force, and that γ_{CM} does not influence this stress. The difference between γ_{CM} and $\gamma_{CC}/2$ is the surface tension σ , which acts uniquely at the surface of the aggregate. The ratio γ_{CC}/γ_{CM} can thus be estimated at the cell scale at the aggregate surface, as these interfacial tensions determine the contact angles ϕ of the cells and the medium: $\cos(\phi/2) = \gamma_{CC}/(2\gamma_{CM})$. In the bulk of the aggregate, γ_{CM} does not act, and the exploitation of experimental force-relaxation curves (cf Figure 5.19) might allow to estimate γ_{CC}/ξ , or $\Delta\mathcal{E}_{T1}/RT$, separately from the surface tension.

We analyse currently if the fast dynamics immediately following a compression can be used quantitatively, and fitted by Eq. [5.13]. If so, then they allow to extract other mechanical parameters from the fits, like the elastic modulus and the characteristic strain. The characteristic strain is

a dimensionless quantity (it is a fraction of the deformation), which allows direct comparison between theory, simulations, and experiments. Theory predicts that this strain is mainly determined by RT/γ_{CC} . We already saw that the dependence of τ^* on RT (Eq. [5.15]) seems to be confirmed by the simulations, as well as the relation of t_c to γ_{CC} through $\Delta\mathcal{E}_{T1}$ (Eq. [5.14]).

Other experiments are possible, and we can simulate them and model them mathematically: aggregate rounding (cf Mombach et al., 2005), fusion of two aggregates, or the relaxation of the aggregate's shape upon the sudden removal of the compression plates. Note that aggregate rounding and fusion are slow processes (e.g. Schötz et al., 2008; Jakab et al., 2008), driven by the aggregate surface tension, whereas the relaxation of a compressed aggregate is faster and probably includes elastic, plastic and viscous behaviour. In longer experiments, surface tension does thus play more significant role, possibly allowing another way to estimate it. Beysens et al. (2000) present two different ways to estimate the fluctuation energy (out RT), from observations of membrane fluctuations and the diffusion of cells in aggregates.

We started to study the dynamics of shape relaxation following retraction of the compressive plates, both in CPM simulations, with the mathematical model, and in experiments (Audren, 2008). Preliminary results indicate that surface tension is indeed not enough to completely round up the aggregate on short time scales.

5.5 Résumé français

Pour pouvoir comparer quantitativement l'adhésion cellulaire de différents types, et prédire le résultat du tri cellulaire *in vitro* et *in vivo*, on mesure les forces exercées par un agrégat homotypique comprimé. Dans la littérature, un agrégat est alors considéré comme une goutte liquide, où seule la tension de surface exerce une force sur les plaques comprimantes. La mesure de cette force et quelques paramètres géométriques serait suffisante pour calculer la tension de surface.

Cependant, tous les agrégats ne sont pas liquides. Dans un agrégat, cellules peuvent se déformer et se réarranger, comme les bulles dans une mousse. Un agrégat peut donc, comme une mousse, être visco-élastoplastique.

Dans les simulations, nous disposons de l'avantage de connaître les paramètres cellulaires, et de pouvoir calculer la valeur théorique de la tension de l'agrégat. Ces méthodes sont vérifiées et optimisées dans les sim-

ulations des gouttes liquides et des agrégats qui se comportent comme des liquides.

En augmentant la tension interfaciale entre cellules, ou en diminuant les fluctuations, l'agrégat se comporte de plus en plus comme un solide. Les déviations de la forme de l'agrégat par rapport au comportement liquide sont quantifiées au bords (asymétrie et irrégularité), et l'anisotropie de la forme des cellules à l'intérieur de l'agrégat. L'anisotropie des cellules est une mesure pour les contraintes élastiques non-relâchées.

L'étude de la relaxation après compression montre que la force et l'anisotropie cellulaire diminuent vite au début, et atteignent un plateau. Nous fittons cette relaxation de la force avec un modèle mathématique non-spatiale, qui traite l'agrégat comme un matériau visco-élasto-plastique. La contrainte élastique stockée dans un agrégat est relâchée par des réarrangements ; la probabilité des réarrangements dépend des fluctuations quand la contrainte est faible, et augmente fortement au-dessus d'une contrainte seuil. La barrière d'énergie qui doit être franchie pour un réarrangement dépend de la tension interfaciale entre cellules.

Dans un agrégat qui ne se comporte pas comme un liquide, la tension de surface agit uniquement à la surface et donc sur la forme de l'agrégat, tandis que les fluctuations et la tension interfaciale cellule-cellule agissent à l'intérieur, et déterminent l'écart de la forme et de la force à celles d'une goutte liquide. Ceci peut être utile dans une étude plus quantitative, qui aura pour but d'estimer les propriétés cellulaires à partir des mesures collectives.

Concluding discussion

6.1 Synthesis

6.1.1 Summary of the results

In **Chapter 3**, we modelled the shape of cells in the developing *Drosophila* retina. Previously, Hayashi and Carthew (2004) suggested that surface minimisation was the driving force determining the shape of the cone cells. This suggestion was based on two observations: clusters of different numbers (two to six) of cone cells resembled clusters of an equal number of soap bubbles; and upon deletion or overexpression of cadherin molecules, the cells changed shape, and ceased looking like bubble clusters.

We simulated the cone cells together with their surrounding cells using surface minimisation (constant tension model), and found that this is not sufficient to account for the packing and the shape of these cells.

We thus proposed a second model, the variable tension model. It takes the balance between adhesion and the cortical cytoskeleton into account: adhesion increases the contact surface between cells, which stretches the cell surface; this increases the tension in the cell cortex, which mechanical properties are mainly determined by the cortical acto-myosin cytoskeleton.

The establishment of cell shape and packing thus involves two feedback loops. First, the interfacial tension determines cell shape; in turn, the cell shape influences the interfacial tension by stretching the cortex. Second, because the cells are closely packed, the shape of one cell influences its neighbours' shape, and vice versa.

The variable tension model correctly describes the wildtype as well as mutants over- or underexpressing N- and/or E-cadherin, or having variable cell numbers.

Chapter 4 focused on the *in vitro* behaviour of dissociated zebrafish germ layer cells. Upon reaggregation of two mixed cell types, these types

sort out. According to the Differential Adhesion Hypothesis (DAH), a theory successful in explaining cell sorting, weakly adhering cells should end up surrounding strongly adhering ones. This would be analogous to the demixing of immiscible liquids, where the liquid with the highest surface tension is surrounded by the one with a lower surface tension.

The adhesion strength of the cells was assessed by Atomic Force Microscopy (AFM): the cells that sorted out to the periphery of the aggregate have in fact a stronger adhesion than the ones in the center, which is in contradiction with the DAH. In search for an alternative explanation, AFM experiments were used to reveal that the cells that ended up in the center had the largest cortical tension.

We explain how the cortical tension influences cell sorting. The surface tension of an aggregate is determined by differences in the interfacial tensions at cell-cell and cell-medium interfaces. The contractile cortical cytoskeleton can thus influence the aggregate surface tension, if it acts differently at the interfaces with the medium and at those with other cells. Indeed, this was confirmed by confocal microscopy images from aggregates: the cells ending up in the center had more actin associated to the cell-medium interfaces than to the cell-cell interfaces.

Differential contractility of the cytoskeleton proves to be more important than adhesion for cell sorting of the zebrafish germ layer cells. This is correctly described by CPM simulations, that link cell-level properties with collectively observable cell organisation.

Finally, in **Chapter 5**, we study how individual cell properties determine the behaviour of aggregates of various cell types. When aggregates behave as liquids, it is possible to measure their surface tension by compressing them between two plates. However, cells do not always behave like molecules in a liquid: tissues are able to acquire a stable shape, they are not always round. We focused on both the shape and the mechanical behaviour of compressed aggregates. By increasing the interfacial tension of the cells, or diminishing their fluctuations, the shape of the aggregate becomes more and more irregular, and the force that is needed to compress it is larger. The aggregate behaves thus not purely as a liquid, but visco-elasto-plastic; elastic through cell deformations, plastic through cell rearrangements, and viscous through dissipation within cells.

This more complete description allows us to link cell parameters to aggregate behaviour: cell-cell interfacial tension not only co-determines the interfacial tension, but also the deviations from liquid behaviour. Cellular fluctuations have the opposite effect, they ‘liquefy’ the aggregate. The aggregate’s surface tension is a driving force for the establishment of the

shape; in aggregates that do not behave as liquids, its action is limited to the surface.

A mathematical model allows us to use the dynamical behaviour of the simulated aggregates, and link that with the same cellular properties. This model successfully describes the transition from liquid to solid behaviour, with all intermediates. This offers possibilities to extend this study to experiments with aggregates, and might allow the extraction of useful parameters from those that do not behave as liquids.

6.1.2 Merits and limits of physical analogies

We have examined three analogies between physical systems and biological tissues and aggregates: soap bubble clusters and cell packing in the developing *Drosophila* retina; demixing of liquids and sorting of zebrafish germ layer cells; and liquid drops and aggregates of embryonic cells.

These simple physical analogies proved to be incomplete. They are however instructive. Like in foams, the space-tiling arrangement of cells in a tissue influences the spatial interactions of cells, their shapes and rearrangements. Like in liquids, cells rearrange due to their fluctuations, which are active in the case of cells.

Cells have a multitude of physical properties, and one physical analogy is not enough to understand the mechanics of tissues. Because of the similar structural properties of foams and tissues, the foam-like structure which is the basis of our modelling provides a convenient starting point, to which other cellular properties can be added.

This provides a framework to understand how individual cell properties act on a collective level, a necessary step in the understanding how gene expression influences morphogenesis.

6.2 Modelling approach

The interaction of many, or even a few cells is not straightforward to understand. It thus required modelling to find out in Chapter 3 that cells, if they would have the properties of bubbles, would not be able to form the shapes observed in the *Drosophila* retina; modelling was equally required to find out how the properties of a contractile cortical cytoskeleton would act on the stability of these shapes. In Chapter 4, modelling was used to test the predictions of the effect of interface-specific contraction on the determination of the aggregate surface tension and cell sorting. Finally, in Chapter 5, we took advantage from the simulations, because they allow to

control the cellular parameters one by one, and to measure quantities that are not easily accessible in experiments (e.g. the pressure in cells, or the cell shape within an aggregate).

In Chapter 3 and 4, the models use knowledge obtained by experiments; the simulation results are directly comparable to the experimental results. In Chapter 5, no direct comparison is made, but we plan to do this in the near future. In the understanding of how biological cells act collectively, simulations are one of the tools; they are the tool we focus on in this thesis.

Energy minimisation

Cells in biological tissues constantly use energy; they are not in equilibrium. The biological regulation of the cell's mechanical properties (having a contractile cortical cytoskeleton, constantly remodelling the membrane and its constituents, and changing the mechanical properties depending on the cell type of your neighbours) costs energy.

All results have been obtained using the same model, the Cellular Potts Model (CPM), designed to find equilibrium, minimum energy states of cellular patterns. Care should thus be taken when simulating out-of equilibrium biological tissues with energy minimising algorithms. One of the results of this thesis is that it is possible and useful to do so in some cases. Energy minimisation is a way to describe an equilibrium of forces; if this description is successful for biological cells, then we might suggest that the cell's shape results from its mechanical properties. The cell can change its mechanical properties, thereby acting on its shape.

In the CPM as we used it here, biological activity is present in the form of a fluctuation allowance. This allows the model cells to explore their neighbourhood, and makes it possible for a tissue to evolve slowly. The equilibrium that the simulations find depends strongly on these fluctuations, as small energy barriers can be passed. To pass larger energy barriers, either a force from outside is needed, or the cells need to change their mechanical properties (cf Rauzi et al., 2008).

Cell based modelling

Modelling in this thesis focuses on the coupling between cell mechanics and tissue properties. The cell mechanics are modelled in a heuristic way: as simple as possible, as complicated as necessary. The adhesion, the cytoskeleton mechanics, and the internal structure of a cell present difficult modelling challenges in themselves. For a more accurate description of adhesion on a subcellular level, see e.g. Evans (1985b); Bell (1978); Bell et al.

(1984); Zhu (2000); the cytoskeleton is a mixture of different fibres, molecular motors and cross-linkers and an exact model is far from being found, see e.g. Stamenovic and Ingber (2002); Janmey and McCulloch (2007) for reviews.

These subcellular mechanical studies will probably reveal new mechanisms, interactions, and give hints to better descriptions, that might alter our view of cell mechanics, and influence the link between cell and tissue behaviour. Most models of subcellular cell mechanics are used to model single cells. Marée et al. (2006) model cells that are very different from the ones studied in this thesis, namely fish keratocytes that move by means of lamellipodia. In their model, that uses the CPM cell as a basis, the intracellular spatial dynamics of actin polymerisation lets the simulated 2D cells crawl. Maurin et al. (2008) model the spreading of a 3D adhesive cell by subdividing the simulated cell in several thousands of small elements, that are linked mechanically to one another. In the dynamics, the internal viscosity of the cells might be important. The approach of Sandersius and Newman (2008) is similar, and also yields single cell viscosity. In recent papers Viens and Brodland (2007); Yang et al. (2008) present cell-level models that can take this viscosity into account. These models have might in the future be used to predict behaviour of tissues and aggregates that non-viscous models miss.

Between the cell-based models and this detailed modelling, a number of intermediate approaches exist. Starruss et al. (2007) model aggregation of rod-shaped myxobacteria by diving one cell into several CPM cells, and assign a bending energy to the rod. In this way, other subcellular structures and their interactions could be represented in the CPM.

6.3 Contemporary literature

During this thesis, a number of relevant papers appeared.

Inspired by Hayashi and Carthew (2004), Sun (2007) tried to model the shape of the cells in the *Drosophila* retina using surface minimisation. Contrary to the approach in Chapter 3, he only models the cone cells, without the surrounding pigmented cells (for terminology, see Figure 3.1). He uses a dynamical model which has been developed for wet foams, explicitly modelling the liquid between the bubbles. With this model, the equilibrium shapes that are obtained minimise their overall perimeter. As had already been shown by Hayashi and Carthew (2004) (reproduced in Figure 3.2), these minimal surfaces are able to mimic the topology of *Roi*-mutant

ommatidia. Differential adhesion is not taken into account, thus making it impossible to model the cadherin mutant shapes.

Hilgenfeldt et al. (2008) use a finite element model, the Surface Evolver (mentioned in Section 2.1) to study the *Drosophila* retina. As in Chapter 3, they take the surrounding cells into account, and model the action of adhesion and the cortical cytoskeleton explicitly, in essentially the same way as Eq. [3.2]. Their approach focused on the shape of wildtype cells, and an optimisation algorithm was used to quantitatively fit the shape of the wildtype ommatidium. They too found that N-cadherin mediated adhesion should be stronger than E-cadherin mediated adhesion. They further applied their model to three N-cadherin deletion mutants, and obtain the same qualitative shape changes as in experiments. Their study confirms the results we obtained in Chapter 3.

Farhadifar et al. (2007) use an energy function similar to Eq. [3.2], to study cell packing in the *Drosophila* wing disk with another algorithm, a vertex model. In the wing disk, which is an epithelial monolayer, cells divide, and Classen et al. (2005) had previously shown that the topological disorder decreases during tissue morphogenesis: the fraction of cells with more or less than 6 sides decreases, increasing the fraction of 6-sided cells. By simulating cell divisions, they find that the network of vertices becomes more or less disordered, and this disorder is compared to experimental images. Furthermore, they simulate laser ablation experiments to calibrate the simulation parameters. Again, their results illustrate that the balance between adhesion and contractility governs cell patterning.

Lecuit and Lenne (2007) reviewed a large number of experimental studies and came to a conclusion similar to the one in Chapter 3: individual cells have a surface tension, which is created mainly by contraction of the acto-myosin cortical cytoskeleton, and diminished by adhesion. In tissues, the cells' surface tensions are responsible for the interfacial tension that shapes the tissues and their constituent cells.

Reviewing the papers mentioned above and our work presented in Chapter 3, Lecuit (2008) concludes that “the physical concepts underlying cell shape have gradually evolved and been refined, departing from the striking, yet too simplistic idea that cells and soap bubbles behave as if similar”.

A study of germlayer-cell behaviour (cf Chapter 4) was conducted by Nomiya and Winklbauer (2008) with *Xenopus* (a frog) gastrula cells. They found that adding extra cell types to a sorting assay can change the final position of the cell types: without epithelial cells, one tissue (anterior mesenchyme) engulfed the other (posterior mesenchyme); a coating with epithelial cells rather results in separation. The authors argue that the mesenchym-epithelium adhesion can alter the relation of the two types of

mesenchym, thus leading to different stable configurations. This is similar to our assumptions for for zebrafish germlayer cell sorting (Figure 4.10).

Very recently, Rauzi et al. (2008) studied convergent extension during *Drosophila* germ band elongation by combining *in vivo* imaging, laser ablation and simulations. By analysing the relaxation after laser ablation, they find that the tension in the interfaces is better described by a model taking cortex elasticity into account than by a constant tension model, supporting the conclusions of Chapter 3. Furthermore, the relaxation is different between interfaces with different orientations, due to the enrichment of myosin II in the interfaces that disappear during intercalation: interface-specific contractility of the cytoskeleton, which was important in Chapter 4, here acts inside the tissue. A finite element model correctly described the spatial behaviour of cells, compared to *in vivo* data: the anisotropy of the cell shape, number and orientation of the rearrangements, the evolution of topological disorder, and tissue elongation. In this model, cell fluctuations are important to facilitate rearrangements: fluctuations thus play the same role as in Chapter 5.

6.4 Outlook

Experiments

In this thesis, we have encountered several ways to study experimentally how cells behave in a tissue: directly in the tissue, visualising the cells by staining and modifying their properties genetically; or in aggregates, by simplifying the conditions and studying one or two cell types at a time, correlating *in vitro* behaviour with *in vivo* properties. These kinds of experiments are still far from being completely understood, and yet other methods are available, enlarging the possibilities of gaining knowledge.

Live imaging of *in vivo* tissues can yield a wealth of information, and is already a useful tool in a wide range of tissues. In *Drosophila*, e.g. the retina (Larson et al., 2008), germ band elongation (Bertet et al., 2004; Blankenship et al., 2006; Cavey et al., 2008; Rauzi et al., 2008), and imaginal disc evagination (Taylor and Adler, 2008) have been studied this way. In the zebrafish, 2D live imaging has already been used (Koppen et al., 2006; Pezeron et al., 2008), and 3D imaging is on its way (Melani et al., 2007).

These data might stimulate and/or require simulations. In the style of Chapter 3 and 4, models can be useful to distinguish between hypothesis, and to predict and/or understand the effect of mutations. Tools developed to quantify patterns in images, initially of foams, are applicable for any

cellular pattern (Aubouy et al., 2003; Graner et al., 2008), and will be useful to quantitatively compare simulation results to experiments. This approach is currently being applied to epithelia (Rauzi et al., 2008; Kabla et al., in prep.; collaboration Y. Bellaïche).

Laser cutting of live tissues is a powerful tool to probe the mechanical properties of tissues *in vivo* (Farhadifar et al., 2007; Cavey et al., 2008; Rauzi et al., 2008). Again, these experiments can be simulated (Farhadifar et al., 2007; Rauzi et al., 2008) and compared qualitatively and quantitatively to the behaviour of foams (Cox et al., 2008).

Modelling perspectives

We have shown how the shape and patterning of cells in tissues and aggregates can be modelled with the CPM. B. Vianay and H. Guillou (*Institut Néel*, Grenoble) now take a similar approach to understand the shape of single cells on micro-patterned substrates (Vianay, in prep.). Here, the energy minimisation algorithm of the CPM becomes a tool to investigate the energy barriers separating different equilibrium shapes, and to assess the ways cells use to pass them when changing their shape. This collaboration will be extended to use the variable tension model to explain the spatial organisation of two cells on adhesive micro-patterns (M. Théry, CEA Grenoble; cf Théry and Bornens, 2006; Théry et al., 2007).

One of the goals of the studies on single cells or aggregates is the understanding of morphogenesis *in vivo*. In this thesis, we have shown that patterns can be established by physical processes. In tissues, physical processes feedback on chemical processes (mechanosensing, e.g. Desprat et al., 2008). Modelling will be a useful tool to separate the role of physical and chemical cell properties in morphogenesis, but also to study their interaction.

Quilliet et al. (2008) studied the topological disorder in foams, which we compared to the order and disorder of the facets in the *Drosophila* wildtype and mutant retinas (cf Figure 3.1 and Figure 3.2a). We explore whether the knowledge from foams could be used to explain the emergence of order in morphogenesis, which mostly means an increase in the number of six-sided cells. Does this require genetic regulation of the patterns, or is it an expected consequence of other cell characteristics? Simulations can be used to identify the minimal biological information necessary for this patterning.

In Chapter 5, cell anisotropy was the result of the application of stress. However, in several tissues, cells are polarised and have anisotropic shapes, while there is no external force acting on the tissue; this is often related to intercalation (Figure 1.6). Cellular polarity involves an atypical adhesion

molecule, flamingo (Usui et al., 1999). We performed simulations that show that an anisotropic distribution of adhesion influences cell shape and can drive intercalation; this will be studied in more detail and compared to experiments (collaboration Y. Bellaïche).

In the morphogenesis of the *Drosophila* retina, cadherins are necessary to orient the ommatidia by rotation (Brown and Freeman, 2003; Brown et al., 2006; Mirkovic and Mlodzik, 2006); cell deaths (Brachmann and Cagan, 2003) and rearrangements (Larson et al., 2008) occur, possibly influenced by adhesion (Bao and Cagan, 2005). We have tried before to model the developmental dynamics in the retina, but two years ago, the experimental data were not sufficient. We currently reconsider this possibility, thanks to the availability of live imaging and new information of the role of adhesion (J.C. Hsu, pers. comm.).

6.5 Résumé français

En résumé, dans cette thèse nous avons étudié trois analogies entre systèmes biologiques et systèmes physiques : l'analogie entre l'arrangement des bulles de savon et cellules dans la rétine de la drosophile, entre la démixion de liquides et tri cellulaire des cellules des feuillets embryonnaires du poisson zèbre, et entre la compression d'une goutte liquide et un agrégat de cellules. Nous avons montré que ces analogies physiques manquent dans les trois cas des ingrédients nécessaires pour comprendre le système biologique. Pourtant, ces analogies sont intéressantes : à partir d'elles, nous pouvons proposer une description physique propre aux tissus et agrégats biologiques.

La simulation des systèmes biologiques a permis de découvrir les ingrédients biologiques responsables pour les comportements observés, et de tester les hypothèses issues des expériences. Un ensemble de cellules peut donc, dans ces cas, être décrit comme un système qui minimise son énergie. Cette approche peut notamment être étendue vers l'effet des propriétés subcellulaires au comportement collectif, avec le CPM ou d'autres modèles.

Pendant le cours de cette thèse, quelques publications pertinentes pour les sujets étudiés ici sont parues. Notamment, le modèle de tension variable, introduit dans Chapitre 3, a été utilisé pour étudier les cellules cônes dans la rétine de la drosophile avec un autre algorithme de minimisation d'énergie, et l'hexagonalisation des cellules dans le *wing disk* de la drosophile. Les conclusions sur l'importance de la contraction du cytosquelette sont confirmées par des études expérimentales.

Quelques perspectives ouvertes par cette thèse font déjà objet des travaux en cours. Des cellules isolées ou à deux sur des substrats micropatternés

6. CONCLUDING DISCUSSION

sont simulées pour étudier les propriétés cellulaires en plus de détail. Les simulations sont utiles pour distinguer la régulation biologique et l'évolution passive dans l'hexagonalisation dans des tissus embryonnaires. Ou encore, dans les simulations, une distribution anisotrope des molécules d'adhésion peut changer la forme des cellules et orienter les réarrangements, et des outils statistiques sont employés pour comparer les résultats des simulations aux films des tissus. Finalement, des nouveaux résultats expérimentaux font de la modélisation de la dynamique de la morphogenèse dans la rétine de la drosophile une piste intéressante.

Stèfstu esténoci.

(Raymond Queneau - Les fleurs bleues, 1965)

Bibliography

- Alberts, B., Johnson, A., Lewis, J., Raff, M., Roberts, K., and Walter, P. (2002). *Molecular biology of the cell*. Garland Science, New York, 4 edition.
- Almgren, F. J. and Taylor, J. E. (1976). Geometry of soap films and soap bubbles. *Sci.Am.*, 235(1):82–93.
- Asipauskas, M., Aubouy, M., Glazier, J. A., Graner, F., and Jiang, Y. (2003). A texture tensor to quantify deformations: the example of two-dimensional flowing foams. *Granul. Matter*, 5(2):71–74.
- Aubouy, M., Jiang, Y., Glazier, J. A., and Graner, F. (2003). A texture tensor to quantify deformations. *Granul. Matter*, 5(2):67–70.
- Audren, B. (2008). Étude de la plasticité et de la viscoélasticité d’agrégats cellulaires. Rapport de stage, ENS & Université Lyon I, Laboratoire de Physique de la Matière Condensée et des Nanostructures.
- Baaijens, F. P., Trickey, W. R., Laursen, T. A., and Guilak, F. (2005). Large deformation finite element analysis of micropipette aspiration to determine the mechanical properties of the chondrocyte. *Ann. Biomed. Eng.*, 33(4):494–501.
- Balland, M., Richert, A., and Gallet, F. (2005). The dissipative contribution of myosin II in the cytoskeleton dynamics of myoblasts. *Eur. Biophys. J.*, 34(3):255–261.
- Bao, S. and Cagan, R. (2005). Preferential adhesion mediated by Hibris and Roughest regulates morphogenesis and patterning in the *Drosophila* eye. *Dev. Cell*, 8(6):925–935.
- Bar-Ziv, R., Tlusty, T., Moses, E., Safran, S. A., and Bershadsky, A. (1999). Pearling in cells: a clue to understanding cell shape. *Proc. Natl. Acad. Sci. U.S.A.*, 96(18):10140–10145.
- Bauer, A. L., Jackson, T. L., and Jiang, Y. (2007). A cell-based model exhibiting branching and anastomosis during tumor-induced angiogenesis. *Biophys. J.*, 92(9):3105–3121.

BIBLIOGRAPHY

- Bell, G. I. (1978). Models for the specific adhesion of cells to cells. *Science*, 200(4342):618–627.
- Bell, G. I., Dembo, M., and Bongrand, P. (1984). Cell adhesion. Competition between nonspecific repulsion and specific bonding. *Biophys. J.*, 45(6):1051–1064.
- Beltman, J. B., Marée, A. F., and De Boer, R. J. (2007). Spatial modelling of brief and long interactions between T cells and dendritic cells. *Immunol Cell Biol.*, 85(4):306–314.
- Bertet, C., Sulak, L., and Lecuit, T. (2004). Myosin-dependent junction remodelling controls planar cell intercalation and axis elongation. *Nature*, 429(6992):667–671.
- Beysens, D. A., Forgacs, G., and Glazier, J. A. (2000). Cell sorting is analogous to phase ordering in fluids. *Proc. Natl. Acad. Sci. U.S.A.*, 97(17):9467–9471.
- Blankenship, J. T., Backovic, S. T., Sanny, J. S., Weitz, O., and Zallen, J. A. (2006). Multicellular rosette formation links planar cell polarity to tissue morphogenesis. *Dev. Cell*, 11(4):459–470.
- Brachmann, C. B. and Cagan, R. L. (2003). Patterning the fly eye: the role of apoptosis. *Trends Genet.*, 19(2):91–96.
- Brakke, K. (1992). The Surface Evolver. *Experimental Mathematics*, 1(2):141–165.
- Brangwynne, C. P., MacKintosh, F. C., Kumar, S., Geisse, N. A., Talbot, J., Mahadevan, L., Parker, K. K., Ingber, D. E., and Weitz, D. A. (2006). Microtubules can bear enhanced compressive loads in living cells because of lateral reinforcement. *J. Cell Biol.*, 173(5):733–741.
- Brevier, J. (2006). *Croissance de contacts cellulaires*. PhD thesis, Université Joseph Fourier, Grenoble I.
- Brodland, G. W. and Chen, H. H. (2000). The mechanics of heterotypic cell aggregates: insights from computer simulations. *J. Biomech. Eng.*, 122(4):402–407.
- Brown, K. E., Baonza, A., and Freeman, M. (2006). Epithelial cell adhesion in the developing *Drosophila* retina is regulated by Atonal and the EGF receptor pathway. *Dev Biol.*, 0(O):O.
- Brown, K. E. and Freeman, M. (2003). Egfr signalling defines a protective function for ommatidial orientation in the *Drosophila* eye. *Development*, 130(22):5401–5412.
- Cagan, R. L. and Ready, D. F. (1989). The emergence of order in the *Drosophila* pupal retina. *Dev. Biol.*, 136(2):346–362.
- Carthew, R. W. (2005). Adhesion proteins and the control of cell shape. *Curr. Opin. Genet. Dev.*, 15(4):358–363.

-
- Cavey, M., Rauzi, M., Lenne, P. F., and Lecuit, T. (2008). A two-tiered mechanism for stabilization and immobilization of E-cadherin. *Nature*, 453(7196):751–756.
- Chichilnisky, E. J. (1986). A mathematical model of pattern formation. *J. theor. Biol.*, 123(1):81–101.
- Classen, A. K., Anderson, K. I., Marois, E., and Eaton, S. (2005). Hexagonal packing of *Drosophila* wing epithelial cells by the planar cell polarity pathway. *Dev. Cell*, 9(6):805–817.
- Cox, S., Graner, F., and Vaz, M. F. (2008). Screening in dry two-dimensional foams. *Soft Matter*, 4:1871–1878.
- Cuvelier, D., Théry, M., Chu, Y. S., Dufour, S., Thiéry, J. P., Bornens, M., Nassoy, P., and Mahadevan, L. (2007). The universal dynamics of cell spreading. *Curr. Biol.*, 17(8):694–699.
- Dai, J. and Sheetz, M. P. (1999). Membrane tether formation from blebbing cells. *Biophys. J.*, 77(6):3363–3370.
- Dai, J., Sheetz, M. P., Wan, X., and Morris, C. E. (1998). Membrane tension in swelling and shrinking molluscan neurons. *J. Neurosci.*, 18(17):6681–6692.
- De Almeida, R. M. C. and Iglesias, J. R. (1989). Equilibrium states of 2d cellular structures. *Phys. Lett. A*, 138(6-7):253–257.
- Desprat, N., Supatto, W., Pouille, P. A., Beaurepaire, E., and Farge, E. (2008). Tissue deformation modulates twist expression to determine anterior midgut differentiation in *Drosophila* embryos. *Dev. Cell*, 15(3):470–477.
- Doherty, G. J. and McMahon, H. T. (2008). Mediation, modulation, and consequences of membrane-cytoskeleton interactions. *Annu. Rev. Biophys.*, 37:65–95.
- Dollet, B., Aubouy, M., and Graner, F. (2005). Anti-inertial lift in foams: a signature of the elasticity of complex fluids. *Phys. Rev. Lett.*, 95(16):168303.
- Drees, F., Pokutta, S., Yamada, S., Nelson, W. J., and Weis, W. I. (2005). Alpha-catenin is a molecular switch that binds E-cadherin-beta-catenin and regulates actin-filament assembly. *Cell*, 123(5):903–915.
- Duguay, D., Foty, R. A., and Steinberg, M. S. (2003). Cadherin-mediated cell adhesion and tissue segregation: qualitative and quantitative determinants. *Dev. Biol.*, 253(2):309–323.
- Evans, E. A. (1985a). Detailed mechanics of membrane-membrane adhesion and separation. I. Continuum of molecular cross-bridges. *Biophys. J.*, 48(1):175–183.
- Evans, E. A. (1985b). Detailed mechanics of membrane-membrane adhesion and separation. II. Discrete kinetically trapped molecular cross-bridges.

BIBLIOGRAPHY

- Biophys. J.*, 48(1):185–192.
- Evans, E. A. and Calderwood, D. A. (2007). Forces and bond dynamics in cell adhesion. *Science*, 316(5828):1148–1153.
- Evans, E. A. and Waugh, R. (1977). Osmotic correction to elastic area compressibility measurements on red cell membrane. *Biophys. J.*, 20(3):307–313.
- Eyring, H. (1935). The activated complex in chemical reactions. *J. Chem. Phys.*, 3(2):107–115.
- Farhadifar, R., Röper, J. C., Aigouy, B., Eaton, S., and Jülicher, F. (2007). The Influence of Cell Mechanics, Cell-Cell Interactions, and Proliferation on Epithelial Packing. *Curr. Biol.*, 17(24):2095–2104.
- Forgacs, G., Foty, R. A., Shafirir, Y., and Steinberg, M. S. (1998). Viscoelastic properties of living embryonic tissues: a quantitative study. *Biophys. J.*, 74(5):2227–2234.
- Foty, R. A., Forgacs, G., Pflieger, C. M., and Steinberg, M. S. (1994). Liquid properties of embryonic tissues: Measurement of interfacial tensions. *Phys. Rev. Lett.*, 72(14):2298–2301.
- Foty, R. A., Pflieger, C. M., Forgacs, G., and Steinberg, M. S. (1996). Surface tensions of embryonic tissues predict their mutual envelopment behavior. *Development*, 122(5):1611–1620.
- Foty, R. A. and Steinberg, M. S. (2005). The differential adhesion hypothesis: a direct evaluation. *Dev. Biol.*, 278(1):255–263.
- Frisch, T. and Thoumine, O. (2002). Predicting the kinetics of cell spreading. *J. Biomech.*, 35(8):1137–1141.
- Gates, J. and Peifer, M. (2005). Can 1000 reviews be wrong? Actin, alpha-Catenin, and adherens junctions. *Cell*, 123(5):769–772.
- Geisbrecht, E. R. and Montell, D. J. (2002). Myosin VI is required for E-cadherin-mediated border cell migration. *Nat. Cell Biol.*, 4(8):616–620.
- Glazier, J. A., Anderson, M. P., and Grest, G. S. (1990). Coarsening in the 2-dimensional soap froth and the large-Q Potts-model - a detailed comparison. *Philos. Mag. B-Phys. Condens. Matter Stat. Mech. Electron. Opt. Magn. Prop.*, 62(6):615–645.
- Glazier, J. A. and Graner, F. (1993). Simulation of the differential adhesion driven rearrangement of biological cells. *Phys. Rev. E*, 47(3):2128–2154.
- Graner, F. (1993). Can surface-adhesion drive cell-rearrangement. 1. biological cell-sorting. *J. theor. Biol.*, 164(4):455–476.
- Graner, F., Dollet, B., Raufaste, C., and Marmottant, P. (2008). Discrete rearranging disordered patterns, part I: Robust statistical tools in two or three dimensions. *Eur. Phys. J. E*, 25(4):349–369.
- Graner, F. and Glazier, J. A. (1992). Simulation of biological cell sorting using a two-dimensional extended Potts model. *Phys. Rev. Lett.*,

-
- 69(13):2013–2016.
- Graner, F., Jiang, Y., Janiaud, E., and Flament, C. (2001). Equilibrium states and ground state of two-dimensional fluid foams. *Phys. Rev. E*, 63(1 Pt 1):011402.
- Graner, F. and Sawada, Y. (1993). Can surface-adhesion drive cell rearrangement. 2. a geometrical model. *J. theor. Biol.*, 164(4):477–506.
- Guilak, F., Erickson, G. R., and Ting-Beall, H. P. (2002). The effects of osmotic stress on the viscoelastic and physical properties of articular chondrocytes. *Biophys. J.*, 82(2):720–727.
- Gumbiner, B. M. (2005). Regulation of cadherin-mediated adhesion in morphogenesis. *Nat. Rev. Mol. Cell Biol.*, 6(8):622–634.
- Halbleib, J. M. and Nelson, W. J. (2006). Cadherins in development: cell adhesion, sorting, and tissue morphogenesis. *Genes Dev.*, 20(23):3199–3214.
- Harris, A. K. (1976). Is Cell sorting caused by differences in the work of intercellular adhesion? A critique of the Steinberg hypothesis. *J. theor. Biol.*, 61(2):267–285.
- Hayashi, T. and Carthew, R. W. (2004). Surface mechanics mediate pattern formation in the developing retina. *Nature*, 431(7009):647–652.
- Hayashi, T., Kojima, T., and Saigo, K. (1998). Specification of primary pigment cell and outer photoreceptor fates by BarH1 homeobox gene in the developing *Drosophila* eye. *Dev. Biol.*, 200(2):131–145.
- Heasman, J. (2002). Morpholino oligos: making sense of antisense? *Dev. Biol.*, 243(2):209–214.
- Helenius, J., Heisenberg, C. P., Gaub, H. E., and Muller, D. J. (2008). Single-cell force spectroscopy. *J. Cell Sci.*, 121(Pt 11):1785–1791.
- Hilgenfeldt, S., Erisken, S., and Carthew, R. W. (2008). Physical modeling of cell geometric order in an epithelial tissue. *Proc. Natl. Acad. Sci. U.S.A.*, 105(3):907–911.
- Höhler, R. and Cohen-Addad, S. (2005). Rheology of liquid foam. *J. Phys.-Condes. Matter*, 17(41):R1041–R1069.
- Holm, E. A., Glazier, J. A., Srolovitz, D. J., and Grest, G. S. (1991). Effects of lattice anisotropy and temperature on domain growth in the 2-dimensional potts-model. *Phys. Rev. A*, 43(6):2662–2668.
- Israelachvili, J. (1991). *Intermolecular & Surface Forces*. Academic Press, London, second edition edition.
- Jakab, K., Damon, B., Marga, F., Doaga, O., Mironov, V., Kosztin, I., Markwald, R., and Forgacs, G. (2008). Relating cell and tissue mechanics: Implications and applications. *Dev. Dyn.*, 237(9):2438–2449.
- Janmey, P. A. (1991). Mechanical properties of cytoskeletal polymers. *Curr. Opin. Cell Biol.*, 3(1):4–11.

BIBLIOGRAPHY

- Janmey, P. A., Euteneuer, U., Traub, P., and Schliwa, M. (1991). Viscoelastic properties of vimentin compared with other filamentous biopolymer networks. *J. Cell Biol.*, 113(1):155–160.
- Janmey, P. A. and McCulloch, C. A. (2007). Cell mechanics: integrating cell responses to mechanical stimuli. *Annu. Rev. Biomed. Eng.*, 9:1–34.
- Jiang, Y., Swart, P. J., Saxena, A., Asipauskas, M., and Glazier, J. A. (1999). Hysteresis and avalanches in two-dimensional foam rheology simulations. *Phys. Rev. E*, 59(5):5819–5832.
- Käfer, J., Hogeweg, P., and Marée, A. F. (2006). Moving forward moving backward: directional sorting of chemotactic cells due to size and adhesion differences. *PLoS. Comput. Biol.*, 2(6):e56.
- Keller, R. (2002). Shaping the vertebrate body plan by polarized embryonic cell movements. *Science*, 298(5600):1950–1954.
- Koppen, M., Fernandez, B. G., Carvalho, L., Jacinto, A., and Heisenberg, C. P. (2006). Coordinated cell-shape changes control epithelial movement in zebrafish and *Drosophila*. *Development*, 133(14):2671–2681.
- Kovacs, E. M. and Yap, A. S. (2008). Cell-cell contact: cooperating clusters of actin and cadherin. *Curr. Biol.*, 18(15):R667–R669.
- Larson, D. E., Liberman, Z., and Cagan, R. L. (2008). Cellular behavior in the developing *Drosophila* pupal retina. *Mech. Dev.*, 125(3-4):223–232.
- Leckband, D. and Prakasam, A. (2006). Mechanism and dynamics of cadherin adhesion. *Annu. Rev. Biomed. Eng.*, 8:259–287.
- Lecuit, T. (2005). Adhesion remodeling underlying tissue morphogenesis. *Trends Cell Biol.*, 15(1):34–42.
- Lecuit, T. (2008). “Developmental mechanics”: cellular patterns controlled by adhesion, cortical tension and cell division. *HFSP J.*, 1(1):44.
- Lecuit, T. and Lenne, P. F. (2007). Cell surface mechanics and the control of cell shape, tissue patterns and morphogenesis. *Nat. Rev. Mol. Cell Biol.*, 8(8):633–644.
- Lenormand, G., Henon, S., Richert, A., Simeon, J., and Gallet, F. (2001). Direct measurement of the area expansion and shear moduli of the human red blood cell membrane skeleton. *Biophys. J.*, 81(1):43–56.
- Marée, A. F., Jilkine, A., Dawes, A., Grieneisen, V. A., and Edelstein-Keshet, L. (2006). Polarization and movement of keratocytes: a multi-scale modelling approach. *Bull. Math. Biol.*, 68(5):1169–1211.
- Marée, A. F. M., Grieneisen, V. A., and Hogeweg, P. (2007). The Cellular Potts Model and biophysical properties of cells, tissues and morphogenesis. In Anderson, A. R. A., Chaplain, M. A. J., and Rejniak, K. A., editors, *Single Cell Based Models in Biology and Medicine*, pages 107–136. Birkhäuser-Verlag, Basel.

-
- Marée, A. F. M. and Hogeweg, P. (2001). How amoeboids self-organize into a fruiting body: multicellular coordination in *Dictyostelium discoideum*. *Proc. Natl. Acad. Sci. U.S.A.*, 98(7):3879–3883.
- Marée, A. F. M. and Hogeweg, P. (2002). Modelling *Dictyostelium discoideum* morphogenesis: the culmination. *Bull. Math. Biol.*, 64(2):327–353.
- Marée, A. F. M., Panfilov, A. V., and Hogeweg, P. (1999a). Migration and thermotaxis of *Dictyostelium discoideum* slugs, a model study. *J. theor. Biol.*, 199(3):297–309.
- Marée, A. F. M., Panfilov, A. V., and Hogeweg, P. (1999b). Phototaxis during the slug stage of *Dictyostelium discoideum*: a model study. *Proc. R. Soc. Lond. Ser. B-Biol. Sci.*, 266(1426):1351–1360.
- Marmottant, P. and Graner, F. (2007). An elastic, plastic, viscous model for slow shear of a liquid foam. *Eur. Phys. J. E*, 23(4):337–347.
- Marmottant, P., Raufaste, C., and Graner, F. (2008). Discrete rearranging disordered patterns, part II: 2D plasticity, elasticity and flow of a foam. *Eur. Phys. J. E*, 25(4):371–384.
- Maurin, B., Canadas, P., Baudriller, H., Montcourrier, P., and Bettache, N. (2008). Mechanical model of cytoskeleton structuration during cell adhesion and spreading. *J. Biomech.*, 41(9):2036–2041.
- Mège, R. M., Gavard, J., and Lambert, M. (2006). Regulation of cell-cell junctions by the cytoskeleton. *Curr. Opin. Cell Biol.*, 18(5):541–548.
- Melani, C., Campana, M., Lombardot, B., Rizzi, B., Veronesi, F., Zanella, C., Bourguine, P., Mikula, K., Peyrieras, N., and Sarti, A. (2007). Cells tracking in a live zebrafish embryo. *Conf. Proc. IEEE. Eng. Med. Biol. Soc.*, 2007:1631–1634.
- Merkel, R., Nassoy, P., Leung, A., Ritchie, K., and Evans, E. (1999). Energy landscapes of receptor-ligand bonds explored with dynamic force spectroscopy. *Nature*, 397(6714):50–53.
- Mirkovic, I. and Mlodzik, M. (2006). Cooperative activities of *Drosophila* DE-Cadherin and DN-Cadherin regulate the cell motility process of ommatidial rotation. *Development*, 133(17):3283–3293.
- Mombach, J. C. and Glazier, J. A. (1996). Single cell motion in aggregates of embryonic cells. *Phys. Rev. Lett.*, 76(16):3032–3035.
- Mombach, J. C., Glazier, J. A., Raphael, R. C., and Zajac, M. (1995). Quantitative comparison between differential adhesion models and cell sorting in the presence and absence of fluctuations. *Phys. Rev. Lett.*, 75(11):2244–2247.
- Mombach, J. C. M., Robert, D., Graner, F., Gillet, G., Thomas, G. L., Idiart, M., and Rieu, J. P. (2005). Rounding of aggregates of biological cells: Experiments and simulations. *Physica A*, 352(2-4):525–534.

BIBLIOGRAPHY

- Montero, J. A. and Heisenberg, C. P. (2004). Gastrulation dynamics: cells move into focus. *Trends Cell Biol.*, 14(11):620–627.
- Morris, C. E. and Homann, U. (2001). Cell surface area regulation and membrane tension. *J. Membr. Biol.*, 179(2):79–102.
- Niewiadomska, P., Godt, D., and Tepass, U. (1999). DE-Cadherin is required for intercellular motility during *Drosophila* oogenesis. *J. Cell Biol.*, 144(3):533–547.
- Ninomiya, H. and Winklbauer, R. (2008). Epithelial coating controls mesenchymal shape change through tissue-positioning effects and reduction of surface-minimizing tension. *Nat. Cell Biol.*, 10(1):61–69.
- Norotte, C., Marga, F., Neagu, A., Kosztin, I., and Forgacs, G. (2008). Experimental evaluation of apparent tissue surface tension based on the exact solution of the Laplace equation. *Europhys. Lett.*, 81(4):R163–R165.
- Ouchi, N. B., Glazier, J. A., Rieu, J. P., Upadhyaya, A., and Sawada, Y. (2003). Improving the realism of the cellular Potts model in simulations of biological cells. *Physica A*, 329(3-4):451–458.
- Paluch, E., Piel, M., Prost, J., Bornens, M., and Sykes, C. (2005). Cortical actomyosin breakage triggers shape oscillations in cells and cell fragments. *Biophys. J.*, 89(1):724–733.
- Peeters, E. A., Oomens, C. W., Bouten, C. V., Bader, D. L., and Baaijens, F. P. (2005). Viscoelastic properties of single attached cells under compression. *J. Biomech. Eng.*, 127(2):237–243.
- Perez, T. D., Nelson, W. J., Boxer, S. G., and Kam, L. (2005). E-cadherin tethered to micropatterned supported lipid bilayers as a model for cell adhesion. *Langmuir*, 21(25):11963–11968.
- Pezeron, G., Mourrain, P., Courty, S., Ghislain, J., Becker, T. S., Rosa, F. M., and David, N. B. (2008). Live analysis of endodermal layer formation identifies random walk as a novel gastrulation movement. *Curr. Biol.*, 18(4):276–281.
- Phillips, H. M. and Steinberg, M. S. (1978). Embryonic tissues as elasticoviscous liquids. I. Rapid and slow shape changes in centrifuged cell aggregates. *J. Cell Sci.*, 30:1–20.
- Phillips, H. M., Steinberg, M. S., and Lipton, B. H. (1977). Embryonic tissues as elasticoviscous liquids. II. Direct evidence for cell slippage in centrifuged aggregates. *Dev. Biol.*, 59(2):124–134.
- Pilot, F. and Lecuit, T. (2005). Compartmentalized morphogenesis in epithelia: from cell to tissue shape. *Dev. Dyn.*, 232(3):685–694.
- Pilot, F., Philippe, J. M., Lemmers, C., and Lecuit, T. (2006). Spatial control of actin organization at adherens junctions by a synaptotagmin-like protein Btsz. *Nature*, 442(7102):580–584.

-
- Plateau, J. (1873). *Statique expérimentale et théorique des liquides soumis aux seules forces moléculaires*, volume 1. Gauthier-Villars, Paris.
- Popper, K. R. (1960). On the sources of knowledge and ignorance. *Proceedings of the British Academy*, 46. Reprinted in 1998 as “Des sources de la connaissance et de l’ignorance” by Rivages, translation M.-I. and M.B. de Launay.
- Puech, P. H., Taubenberger, A., Ulrich, F., Krieg, M., Muller, D. J., and Heisenberg, C. P. (2005). Measuring cell adhesion forces of primary gastrulating cells from zebrafish using atomic force microscopy. *J. Cell Sci.*, 118(Pt 18):4199–4206.
- Quilliet, C., Ataei Talebi, S., Rabaud, D., Käfer, J., Cox, S. J., and Graner, F. (2008). Topological and geometrical disorders correlate robustly in two-dimensional foams. *Phil. Mag. Lett.*, 88:651–660.
- Quintin, S., Gally, C., and Labouesse, M. (2008). Epithelial morphogenesis in embryos: asymmetries, motors and brakes. *Trends Genet.*, 24(5):221–230.
- Rasband, W. (2005). ImageJ 1.34s. <http://rsb.info.nih.gov/ij/>.
- Raucher, D. and Sheetz, M. P. (1999). Characteristics of a membrane reservoir buffering membrane tension. *Biophys. J.*, 77(4):1992–2002.
- Raufaste, C. (2007). *Rhéologie et imagerie des écoulements 2D de mousse*. PhD thesis, Université Joseph Fourier, Grenoble I.
- Raufaste, C., Dollet, B., Cox, S., Jiang, Y., and Graner, F. (2007). Yield drag in a two-dimensional foam flow around a circular obstacle: Effect of liquid fraction. *Eur. Phys. J. E*, 23(2):217–228.
- Rauzi, M., Verant, P., Lecuit, T., and Lenne, P.-F. (2008). Nature and anisotropy of cortical forces orienting *Drosophila* tissue morphogenesis. *Nat. Cell Biol.*, in press.
- Rieu, J. P., Upadhyaya, A., Glazier, J. A., Ouchi, N. B., and Sawada, Y. (2000). Diffusion and deformations of single hydra cells in cellular aggregates. *Biophys. J.*, 79(4):1903–1914.
- Robinson, E. E., Zazzali, K. M., Corbett, S. A., and Foty, R. A. (2003). Alpha5beta1 integrin mediates strong tissue cohesion. *J. Cell Sci.*, 116(Pt 2):377–386.
- Rosa, M. E. and Fortes, M. A. (2006). Uniaxial deformation tests of aqueous foams: rate effects and topological changes. *Philos. Mag.*, 86(32):4997–5007.
- Rosenbluth, M. J., Lam, W. A., and Fletcher, D. A. (2006). Force microscopy of nonadherent cells: a comparison of leukemia cell deformability. *Biophys. J.*, 90(8):2994–3003.
- Sandersius, S. A. and Newman, T. J. (2008). Modeling cell rheology with the Subcellular Element Model. *Phys. Biol.*, 5(1):15002.

BIBLIOGRAPHY

- Sato-Maeda, M., Uchida, M., Graner, F., and Tashiro, H. (1994). Quantitative evaluation of tissue-specific cell adhesion at the level of a single cell pair. *Dev. Biol.*, 162(1):77–84.
- Savill, N. J. and Hogeweg, P. (1997). Modelling morphogenesis: From single cells to crawling slugs. *J. theor. Biol.*, 184(3):229–235.
- Schock, F. and Perrimon, N. (2002). Molecular mechanisms of epithelial morphogenesis. *Annu. Rev. Cell Dev. Biol.*, 18:463–493.
- Schötz, E. M., Burdine, R. D., Jülicher, F., Steinberg, M. S., Heisenberg, C. P., and Foty, R. A. (2008). Quantitative differences in tissue surface tension influence zebrafish germ layer positioning. *HFSP J.*, 2(1):42–56.
- Sheetz, M. P. and Dai, J. (1996). Modulation of membrane dynamics and cell motility by membrane tension. *Trends Cell Biol.*, 6(3):85–89.
- Sheetz, M. P., Sable, J. E., and Dobereiner, H. G. (2006). Continuous membrane-cytoskeleton adhesion requires continuous accommodation to lipid and cytoskeleton dynamics. *Annu. Rev. Biophys. Biomol. Struct.*, 35:417–434.
- Shi, Q., Chien, Y. H., and Leckband, D. (2008). Biophysical properties of cadherin bonds do not predict cell sorting. *J. Biol. Chem.*, in press.
- Solnica-Krezel, L. (2005). Conserved patterns of cell movements during vertebrate gastrulation. *Curr. Biol.*, 15(6):R213–R228.
- Stamenovic, D. and Ingber, D. E. (2002). Models of cytoskeletal mechanics of adherent cells. *Biomech. Model. Mechanobiol.*, 1(1):95–108.
- Starruss, J., Bley, T., Sogaard-Andersen, L., and Deutsch, A. (2007). A new mechanism for collective migration in *Myxococcus xanthus*. *J. Stat. Phys.*, 128(1-2):269–286.
- Stein, M. B. and Gordon, R. (1982). Epithelia as bubble rafts: a new method for analysis of cell shape and intercellular adhesion in embryonic and other epithelia. *J. theor. Biol.*, 97(4):625–639.
- Steinberg, M. S. (1963). Reconstruction of tissues by dissociated cells. Some morphogenetic tissue movements and the sorting out of embryonic cells may have a common explanation. *Science*, 141:401–408.
- Sun, Q. (2007). The mechanism of pattern formation in the developing *Drosophila* retina. *Sci. China. C. Life Sci.*, 50(1):120–124.
- Taylor, J. and Adler, P. N. (2008). Cell rearrangement and cell division during the tissue level morphogenesis of evaginating *Drosophila* imaginal discs. *Dev. Biol.*, 313(2):739–751.
- Théry, M. and Bornens, M. (2006). Cell shape and cell division. *Curr. Opin. Cell Biol.*, 18(6):648–657.
- Théry, M., Jimenez-Dalmaroni, A., Racine, V., Bornens, M., and Julicher, F. (2007). Experimental and theoretical study of mitotic spindle orientation. *Nature*, 447(7143):493–496.

-
- Thomas, G. L., De Almeida, R. M. C., and Graner, F. (2006). Coarsening of three-dimensional grains in crystals, or bubbles in dry foams, tends towards a universal, statistically scale-invariant regime. *Phys. Rev. E*, 74(2).
- Thompson, D. (1942). *On Growth and Form: A New Edition*. Cambridge University Press. Reprinted by Dover Publications, New York, 1992.
- Thoumine, O., Cardoso, O., and Meister, J. J. (1999). Changes in the mechanical properties of fibroblasts during spreading: a micromanipulation study. *Eur. Biophys. J.*, 28(3):222–234.
- Thoumine, O. and Ott, A. (1997). Time scale dependent viscoelastic and contractile regimes in fibroblasts probed by microplate manipulation. *J. Cell Sci.*, 110:2109–2116.
- Trickey, W. R., Baaijens, F. P., Laursen, T. A., Alexopoulos, L. G., and Guilak, F. (2006). Determination of the Poisson’s ratio of the cell: recovery properties of chondrocytes after release from complete micropipette aspiration. *J. Biomech.*, 39(1):78–87.
- Usui, T., Shima, Y., Shimada, Y., Hirano, S., Burgess, R. W., Schwarz, T. L., Takeichi, M., and Uemura, T. (1999). Flamingo, a seven-pass transmembrane cadherin, regulates planar cell polarity under the control of Frizzled. *Cell*, 98(5):585–595.
- Vaz, M. F. (2008). Liquid foams: an introduction. *Phil. Mag. Lett.*, 88:627–636.
- Viens, D. and Brodland, G. W. (2007). A three-dimensional finite element model for the mechanics of cell-cell interactions. *J. Biomech. Eng.*, 129(5):651–657.
- Weaire, D. and Hutzler, S. (1999). *The Physics of Foams*. Oxford University Press.
- Wolff, T. and Ready, D. (1993). Pattern formation in the *Drosophila* retina. In Bate, M. and Martinez Arias, A., editors, *The Development of Drosophila melanogaster*, pages 1277–1325. Cold Spring Harbor Laboratory Press.
- Yamada, S., Pokutta, S., Drees, F., Weis, W. I., and Nelson, W. J. (2005). Deconstructing the cadherin-catenin-actin complex. *Cell*, 123(5):889–901.
- Yang, L., Effler, J. C., Kutscher, B. L., Sullivan, S. E., Robinson, D. N., and Iglesias, P. A. (2008). Modeling cellular deformations using the level set formalism. *BMC. Syst. Biol.*, 2:68.
- Zhu, B., Chappuis-Flament, S., Wong, E., Jensen, I. E., Gumbiner, B. M., and Leckband, D. (2003). Functional analysis of the structural basis of homophilic cadherin adhesion. *Biophys. J.*, 84(6):4033–4042.
- Zhu, C. (2000). Kinetics and mechanics of cell adhesion. *J. Biomech.*, 33(1):23–33.

Abstract

To understand how cellular mechanical properties act on the level of a tissue, where they are implied in morphogenesis, it has been proposed that cells act as soap bubbles or molecules in a liquid. We test these analogies between tissues and physical systems with a computational model, in collaboration with experimentalists.

In the retina of *Drosophila*, the packing of cells has been compared to soap bubble packing. We find that the resemblance is not due to the physical resemblance of cells and bubbles, but to a similar organisation on the collective level: cells in a tissue tile the space, like bubbles in a foam, thereby influencing each other's shapes.

The spontaneous sorting of cells of different types has been compared to the demixing of liquids. While in liquids this behaviour is due to the attraction between molecules, we find that in aggregates of zebrafish germlayer cells differential contraction of the cytoskeleton plays a role as well.

Compression of an aggregate of cells has been analysed as if the aggregate behaved as a liquid drop, where only the surface tension determines its properties. However, individual cells in the aggregate deform and rearrange, and solid-like stresses inside the aggregate co-determine its shape and forces.

The widely used physical analogies prove thus to be incomplete, but interesting. We propose a distinctive description, in which an aggregate or tissue is a collection of closely packed living cells that change shape and rearrange. This approach allows to study how cell adhesion, cortical tension and the cellular fluctuations govern the behaviour on the collective level, and on morphogenesis.

Résumé

Pour comprendre comment les propriétés mécaniques des cellules jouent au niveau d'un tissu et déterminent la morphogénèse, il a été proposé que les cellules se comportent comme les bulles de savon, ou comme des molécules dans un liquide. Nous testons numériquement ces analogies entre tissus et systèmes physiques, en collaboration avec des expérimentateurs.

Dans la rétine de la *Drosophile*, les cellules ont été comparées aux bulles de savon. On trouve que la ressemblance entre les cellules et bulles de savon n'est pas due à leur propriétés physiques, mais à leur structure collective : les cellules dans un tissu pavent l'espace, comme les bulles dans une mousse, donc elles influencent leur formes entre elles.

Le tri spontané des cellules de types différents est souvent comparé à la démixion de liquides. Pour les liquides, ce comportement est produit par des différences d'attraction entre les molécules, alors qu'on trouve que pour les cellules embryonnaires du poisson zèbre la contraction différentielle du cortex des cellules est le facteur le plus important.

La compression d'un agrégat de cellules a été analysé comme si c'était une goutte liquide, où les propriétés sont déterminées uniquement par la tension de surface. Mais, les cellules dans un agrégat peuvent se déformer et se réarranger, et des contraintes plutôt solides co-déterminent la forme et les forces de l'agrégat.

Ces analogies physiques sont donc incomplètes, mais intéressantes. A partir d'elles, nous proposons ici une description propre aux cellules : un agrégat ou tissu est une collection de cellules vivantes qui peuvent changer leur forme et se réarranger. Cette approche nous permet d'étudier l'effet de l'adhésion cellulaire, la tension corticale, et les fluctuations des cellules sur le comportement collectif et la morphogénèse.